

University of Massachusetts School of Marine Sciences

SECONDARY FLOW ASSOCIATED WITH TRANSIENT TIDAL EDDY  
MOTION IN THE WESTERN GULF OF MAINE

A Thesis in

Marine Science and Technology

by

Gustavo Mastrorocco Marques

Copyright 2010 by Gustavo Mastrorocco Marques

Submitted in Partial Fulfillment of the

Requirements for the Degree of

Master of Science

September 2010

I grant the University of Massachusetts Dartmouth the non-exclusive right to use  
the work for the purpose of making single copies of the work available to the public  
on a not-for-profit basis if the University's circulating copy is lost or destroyed.

---

Gustavo Mastrorocco Marques

Date \_\_\_\_\_

We approve the thesis of Gustavo Mastrorocco Marques

Date of Signature

---

Wendell S. Brown  
Professor, Department of Estuarine and Ocean Sciences  
Thesis Advisor

---

Amit Tandon  
Associate Professor, Department of Estuarine and Ocean Sciences  
Thesis Committee

---

Geoffrey Cowles  
Assistant Professor, Department of Fisheries Oceanography  
Thesis Committee

---

Louis Goodman  
Professor/Chair, Department of Estuarine and Ocean Sciences  
Thesis Committee

---

Avijit Gangopadhyay  
Associate Dean and Graduate Program Director

---

John W. Farrington  
Interim Dean, School for Marine Science and Technology

---

Robert R. Gamache  
Dean, University of Massachusetts School of Marine Sciences

---

Alex J. Fowler  
Associate Provost for Graduate Studies

---

# Abstract

## SECONDARY FLOW ASSOCIATED WITH TRANSIENT TIDAL EDDY MOTION IN THE WESTERN GULF OF MAINE

by Gustavo Mastrorocco Marques

The kinematics and dynamics of the tidal circulation in the western Gulf of Maine (GoM) region are investigated with focus on the secondary circulation. This study is motivated by previous research suggesting the formation and evolution of transient tidal eddy motions in a high-density scallop region off Chatham, Massachusetts. Three-dimensional flow velocity and surface elevation fields were obtained using the QUODDY finite-element coastal ocean circulation model in the barotropic mode and forced by the five most important tidal constituents in the region ( $M_2$ ,  $N_2$ ,  $S_2$ ,  $K_1$  and  $O_1$ ). Observations are used to justify the model setup, as well as for validation purposes. Two-dimensional momentum balances in a streamwise/normal coordinate system suggest the existence of two different dynamic regions, which are related to the complex bathymetry in this area. The shallower-water kinematic characteristics are close to those of a progressive wave, where the principal streamwise dynamical balance is between pressure gradient force (PGF) and local acceleration (LA), with strong influence from bottom friction (BF). In deeper waters, the kinematic characteristics are close to those of a standing wave, where the principal streamwise dynamical balance is between PGF and LA alone (no friction contribution). In the shallow-water regions, a streamwise adverse PGF during maximum semidiurnal flood (ebb) flow results in the formation of

anticlockwise (clockwise) phase eddy motion that translates along the bathymetric boundary between the two dynamical regions. The dynamics are nonlinear such that the ebb flow-related eddy motion is weaker than the flood flow eddy motion. The dynamics of these transient phase eddy motions differ from transient tidal eddies that are reported to form around small promontories. The momentum balances also reveal a secondary circulation that is orthogonal to the primary tidal flow. The secondary flow dynamics are mainly controlled by a balance between PGF and Coriolis. The secondary flow kinematics feature time/space-varying convergences and divergences that are affected by the transient tidal eddy motions. The mechanisms controlling the long-term average tidal secondary circulation, which is relevant for biological transport, are discussed.

# Acknowledgements

I am heartily thankful to my advisor, Wendell Brown, for his encouragement, guidance and support during the development of this thesis. I also appreciate the time and interest expended by the rest of my committee members: Geoffrey Cowles, Amit Tandon and Louis Goodman.

In addition, I thank Zhitao YU (URI), Keston Smith (WHOI), James Hench (Duke University), Rocky Geyer (WHOI) and Rich Signell (USGS) for helping me along the evolution of this thesis.

All students, staff and professors at SMAST made it an excellent place to work. In particular, I would like to thank Frank “Chico” Smith for his friendship and help in the past three years.

Finally, I thank my family for providing enough love, support and friendship throughout my life; this thesis would not be possible without them.

This work was supported by MIT Sea Grant, project number 2007-R/RC-104 and by NOAA Grant NA07NOS4730221 to Rutgers University through a subcontract to UMassD.

# Table of Contents

<b>List of Tables</b>	<b>ix</b>
<b>List of Figures</b>	<b>xi</b>
<b>1 Introduction</b>	<b>1</b>
1.1 Eddy Formation around Coastal Promontories	1
1.2 Theoretical Considerations	3
1.3 Tidal Eddy Motion in the Western Gulf of Maine	10
1.4 Thesis Objectives	13
1.5 Thesis Overview	16
<b>2 Measurements</b>	<b>17</b>
2.1 Current and Pressure Time Series	18
2.2 Hydrographic Measurements	21
2.3 Chapter Summary	26
<b>3 Numerical Model Simulations</b>	<b>28</b>
3.1 Model Description	28
3.2 Boundary Conditions	29
3.2.1 Tidal elevations	29

3.2.2	Normal flow	29
3.3	Model Operation	31
3.4	Model Sensitivity and Validation	32
3.5	Basic Model Eddy Motion	34
3.5.1	Snapshots of circulation and relative vorticity	36
3.5.2	Time series at fixed locations	39
<b>4</b>	<b>Dynamics of the Basic Eddy Motion</b>	<b>44</b>
4.1	Depth-Averaged Momentum Balance Calculations	44
4.2	Temporal Variabilities at Fixed Locations	46
4.3	Spatial Variability	47
4.3.1	Maximum flood (A)	47
4.3.2	Second half flood (B)	49
4.3.3	Slack before ebb (C)	51
4.3.4	First half ebb (D)	53
4.4	Summary of Results	55
<b>5</b>	<b>Three-Dimensional Circulation</b>	<b>58</b>
5.1	Velocity Structure	58
5.1.1	Maximum flood (A)	58
5.1.2	Slack before ebb (C)	59
5.1.3	Maximum ebb (E)	62
5.1.4	First half flood (G)	64
5.2	Three-Dimensional Residual Circulation	67
5.3	Summary of Results	68

<b>6 Discussion</b>	<b>73</b>
6.1 Eddy Motion Formation and Evolution	73
6.2 Momentum Balance and Flow Separation	74
6.3 Three-Dimensional Circulation	75
6.3.1 Mechanisms controlling the secondary flow	75
6.3.2 Upwelling and downwelling	76
6.3.3 Maximum strength of the secondary flow	79
6.3.4 Tidal long-term circulation	80
<b>7 Summary and Concluding Remarks</b>	<b>83</b>
 <b>Appendices</b>	
<b>A Model/Observation Comparisons</b>	<b>86</b>
<b>B The Gradient of a Scalar in an Unstructured Grid</b>	<b>92</b>
<b>Bibliography</b>	<b>95</b>

# List of Tables

1.1	Flow regimes and the corresponding dominant force balances (Alaee et al. 2004)	9
2.1	Moored current and sea-surface elevation (TTE and NAUSET) station locations, including the Moody et al. (1984) sites (NSA, NSB, NSD and NAUSET)	18
2.2	The harmonic constants for the 5 principal and 2 nonlinear tidal constituents of the ADCP 6.35-meter AB eastward and northward current components	22
2.3	Same as Table 2.2, but for 8.35-meter AB	22
2.4	The harmonic constants for the 5 principal and 2 nonlinear tidal constituents of the TTE bottom pressure (BP) record	23
2.5	The harmonic constants for the five principal constituents based on a harmonic analysis of hindcast eastward and northward current component series at three nearby historic stations (Moody et al. 1984)	24
2.6	The moored ADCP (at 6.35 and 8.35 meters AB) and bottom pressure (BP) time series bulk statistics	25
2.7	Station information for the 27 January 2009 shipboard CTD survey	25

2.8	The SBE-25 specifications	26
3.1	Description of the numerical simulations that were conducted in order to examine the model's sensitivity to bottom drag coefficient ( $C_d$ )	32
3.2	Comparison between the three simulations based on averages and standard deviations for the amplitude % error and phase difference (model-observations)	33
3.3	The $M_2$ tidal current ellipses from both model results and observations	36
3.4	Times in hours selected for analysis from Figure 3.4 and their designated letters	36
3.5	Location of the nodes used to reference the tides (R) and of the inner (I) and outer (O) nodes used in the time series analysis	38

# List of Figures

1.1	Downwelling induced by Coriolis force acting on the coastal current (Garrett and Loucks 1976)	5
1.2	Streamwise-normal coordinate system	6
1.3	The flow regime diagram based upon the two non-dimensional numbers, $R_{om}$ and $R_{ef}$ (Alaee et al. 2004)	10
1.4	The location map of the study region	12
1.5	Surface ebb (southward) current one hour before the change of tide (COT) from ebb to flood at 1000 GMT, 9 April 2005	13
1.6	The model $M_2$ change of tidal flow (COT) from flood (northward) to ebb (southward)	14
1.7	Model-derived cross-stream velocity section (cm/s) and vertical flow	15
2.1	Research Vessel <i>R&amp;R</i> fantail	18
2.2	ADCP velocity time series at station TTE	20
2.3	Time series of full 5-minute TTE bottom pressure series (db)	21
2.4	The TTE $M_2$ tidal current ellipses at 6.35 and 8.35 meters AB	23
2.5	The 27 January 2009 vertical sections of (top) temperature, (middle) salinity and (bottom) density anomaly (sigma-t)	27

3.1	The GHSD mesh for the QUODDY model domain	30
3.2	The $M_2$ tidal current ellipses for average measured currents (black) at stations TTE, NSA, NSB and NSD	34
3.3	Comparison between surface currents derived from CODAR to the model results	35
3.4	Northward depth-averaged velocity time series at the reference (R) model node	37
3.5	Locations of the reference node (R), in black, and the nodes at which time series of elevation, velocity, vorticity and the terms in Eqs. (4.3) and (4.4) are presented	38
3.6	Depth-averaged vector currents with color-coded relative vorticity from maximum flood (Time A) to first half ebb (Time D)	40
3.7	Depth-averaged vector currents with color-coded relative vorticity from maximum ebb (Time E) to first half flood (Time H)	41
3.8	Model-derived time series at points I and O	43
4.1	Time series of momentum flux at nodes I and O	48
4.2	Circulation and momentum balance at maximum flood (time A)	50
4.3	As in figure 4.2, but for second half flood (time B)	52
4.4	As in figure 4.2, but for slack before ebb (time C)	54
4.5	As in figure 4.2, but for first half ebb (time D)	56
5.1	Model result at maximum flood (time A)	60
5.2	Depth-averaged velocity (m/s) and its divergence (color coded, 1/s) for times A, C, E and G	61

5.3	As in figure 5.1, but for slack before ebb (time C), when an anticlockwise eddy motion is present	63
5.4	As in figure 5.1, but for maximum ebb (time E)	65
5.5	As in figure 5.1, but for slack before flood (time G), when a clockwise eddy motion is present	66
5.6	Residual depth-averaged circulation. Transects 1 (red) and 2 (blue) are located	67
5.7	The 31-day time-averaged (residual) model results in streamwise/normal coordinates	69
5.8	Schematic of the tidal circulation along transect 1 from time A to time G	70
5.9	Schematic of the residual tidal circulation along transects 1 and 2	72
6.1	Schematic of the transect 1 maximum flood tidal flow (time A)	78
6.2	Schematic of the transect 1 slack before ebb flow (time C)	79
6.3	Distribution of long-term depth-averaged model flow vectors (cm/s) and its divergence ( $s^{-1}$ , color-coded)	82
A.1	Difference between modeled and observed $M_2$ tidal sea level amplitudes	87
A.2	Difference between modeled and observed $M_2$ tidal sea level phases	87
A.3	Difference between modeled and observed $S_2$ tidal sea level amplitudes	88
A.4	Difference between modeled and observed $S_2$ tidal sea level phases	88
A.5	Difference between modeled and observed $N_2$ tidal sea level amplitudes	89
A.6	Difference between modeled and observed $N_2$ tidal sea level phases	89
A.7	Difference between modeled and observed $K_1$ tidal sea level amplitudes	90
A.8	Difference between modeled and observed $K_1$ tidal sea level phases	90

A.9	Difference between modeled and observed $O_1$ tidal sea level amplitudes	91
A.10	Difference between modeled and observed $O_1$ tidal sea level phases	91
B.1	Idealized unstructured mesh with 13 nodes and 16 elements	93
B.2	a) Linear distribution of a scalar $S$ over the idealized mesh according to Eq. (B.4), b) gradient of $S$ in the $y$ direction, and c) gradient of $S$ in the $x$ direction	94

# Chapter 1

## Introduction

### 1.1 Eddy Formation around Coastal Promontories

It has long been known that coastal promontories (including headlands and islands) have pronounced influence on the spatial structure of tidal currents. Eddies have been identified in association with coastal promontories in a variety of coastal environments (Pingree and Maddock 1977; Pingree and Maddock 1979a; Wolanski et al. 1984; Black and Gay 1987; Geyer and Signell 1990; Lee et al. 1999; Berthot and Pattiaratchi 2006). The formation and structure of tidal eddies have been investigated using theoretical, field, numerical (mainly depth-averaged) and remote-sensing techniques.

Pingree and Maddock (1979a) used a numerical model to study the residual circulation in the vicinity of Portland Bill, a headland in the English Channel. They proposed that vorticity at the headland was primarily generated by bottom frictional torque rather than the no-slip boundary condition. This results from large frictional force onshore and small frictional force further offshore. In addition, they indicated that there was some asymmetry in the flood and ebb tidal patterns due to

the effects of the Earth's rotation.

Wolanski et al. (1984) observed the generation of tidal eddies around Rattray Island (northeast Australia) using an array of 24 current meters, float and hydrographic measurements, and aerial photos. For their study, friction was comparable to advection, and a stable wake eddy was observed. These authors then speculated that if friction dominated over advection, eddies would not form.

In dealing with natural eddies in reversing tidal flow, Black and Gay (1987) suggested that the unsteadiness of the flow and the bottom friction depth-dependence would lead to the formation of "phase eddies." Using numerical model results they showed that large phase differences develop between the offshore current and the nearshore current in the lee of a promontory or in an area of relatively high friction. The nearshore waters then accelerate earlier than the offshore flow and have a flow direction opposite to that of the decelerating offshore flow. These "phase eddies" are distinctly different than water-transporting eddies formed due to flow separation at high modified Reynolds number (see definition of modified Reynolds number in section 1.2), like those considered by Signell and Geyer (1991) as described next.

Geyer and Signell (1990) used a shipboard Acoustic Doppler Current Profiler (ADCP) and moored current meter to obtain detailed measurements of the spatial structure of the tidal flow around a headland in Vineyard Sound, Massachusetts. They clearly observed flow separation near the tip of the headland and the formation of transient eddies downstream of the headland during flood and ebb flow. Signell and Geyer (1991) explained these observations using a simplified analytical model and numerical simulations. They suggested that in order to have

flow separation at the tip of a headland, the dominant balance in the momentum equation must be between advection and pressure gradient force.

The flow associated with the evolution of both the phase eddies and the Signell and Geyer (1991) eddies has substantial influence on many processes. Some research has suggested that bottom morphology may be controlled by tidal eddies in some areas (Zimmerman 1976; Pingree 1978; Geyer and Signell 1990; Neill et al. 2007).

Zimmerman (1976) also suggested that dispersion of waterborne material may be significantly influenced by this type of eddy structure. In addition, the associated secondary flow results in physical and biological fronts, affecting the aggregation of eggs, larvae and plankton and consequently distribution and density of benthic assemblages and of pelagic predators (Wolanski and Hamner 1988).

## 1.2 Theoretical Considerations

Geyer (1993) defines secondary flow the flow in the plane normal to the direction of the vertically averaged current. Field observations and numerical simulations have confirmed the presence of secondary flow patterns near coastal promontories (Geyer 1993; Wolanski et al. 1996; Alaee et al. 2004; Berthot and Pattiaratchi 2006). The secondary flows around these geological features can be driven by local imbalances (1) between the centrifugal<sup>1</sup> force (due to flow curvature) and the large-scale cross-stream pressure gradient force, or (2) between the Coriolis<sup>1</sup> and the large-scale cross-stream pressure gradient forces.

The first force balance is associated with the well-known secondary flow patterns that are induced when, for example, river flow rounds a bend. In the ocean, the

---

<sup>1</sup>We shall use the terms Coriolis force and centrifugal force since, in this study, we are considering flows in an non-inertial frame of reference.

alongshore current near the sea floor is reduced by bottom friction in the bottom boundary layer (BBL), with an equal reduction in the outward centrifugal force. Because the large-scale water-level-induced cross-stream pressure gradient force remains unchanged throughout, there is a net inward force (toward the center of rotation) in the BBL. The force imbalance drives the near-bottom flow toward the curving coast, where it upwells. Continuity requires an outward near-surface flow. Since the force balance configuration is independent of the alongcoast flow direction, the secondary flow orientation is always seaward at the surface and landward at depth.

The second force balance is the one in which the alongcoast current is in near geostrophic balance (i.e., a balance exists between pressure gradient force and Coriolis force; see Fig. 1.1). This situation applies where the radius of flow curvature of the streamline ( $R_s$ ) is so large that the Coriolis force dominates. However, in the BBL near the sea floor (see Fig. 1.1), the alongshore current is reduced by bottom friction, with a corresponding reduction in the Coriolis force. As in mechanism (1), the sea-level-induced pressure gradient force is unchanged throughout the BBL, producing a force imbalance that forces an offshore flow in the BBL. Continuity demands downwelling near the coast and inshore surface flow. Interestingly, the Coriolis-induced circulation is independent of flow speed. In summary, the configuration of the centrifugal-induced secondary flow is always seaward at the surface and landward at depth, while the sense of the Coriolis-induced flow depends on the main flow direction. These two mechanisms reinforce the strength of the flow for cyclonic curvature, while they compete with each other for anticyclonic curvature.

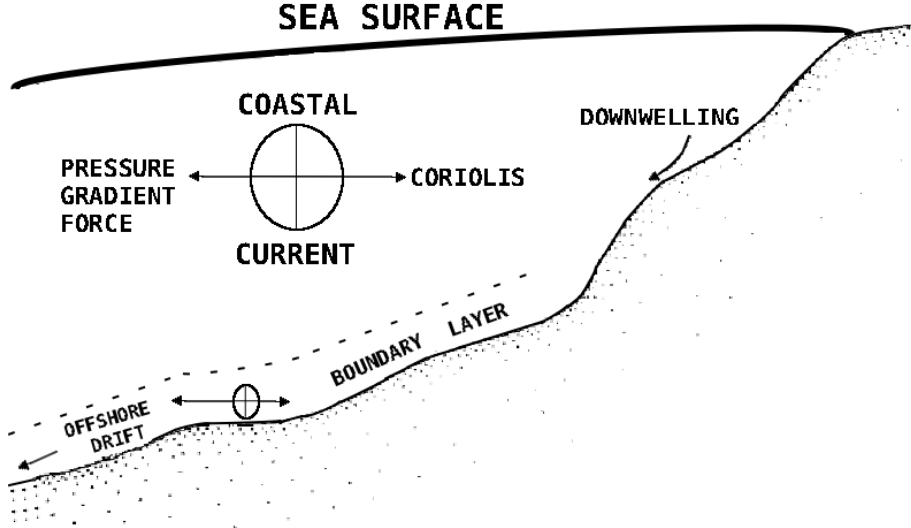


Figure 1.1: Downwelling induced by Coriolis force acting on the coastal current (Garrett and Loucks 1976).

Garrett and Loucks (1976) suggested that the centrifugal force associated with the strong tidal current was responsible for driving upwelling along the Yarmouth shore of Nova Scotia. They compared the strength of Coriolis and centrifugal forces and found that the latter was greater by a factor of two.

To study the secondary flow, many authors have adopted a streamwise/normal coordinate system because it allows for a more intuitive physical interpretation of strongly curving flow fields (Kalkwijk and Booij 1986; Geyer 1993; Hench and Leutttich 2003; Alaee et al. 2004). In this coordinate frame, the streamwise coordinate  $s$  is defined to be in the direction of the vertically averaged flow everywhere, while the normal (or cross-stream) coordinate  $n$  is positive to the left of the vertically averaged flow (Fig. 1.2). The  $z$ -axis is positive in the upward direction. By definition, the vertical average of the normal flow  $\bar{u}_n$  is zero everywhere, and the vertically-varying normal velocity  $u_n$  is the secondary circulation.

Kalkwijk and Booij (1986) developed a model for secondary flow by assuming that

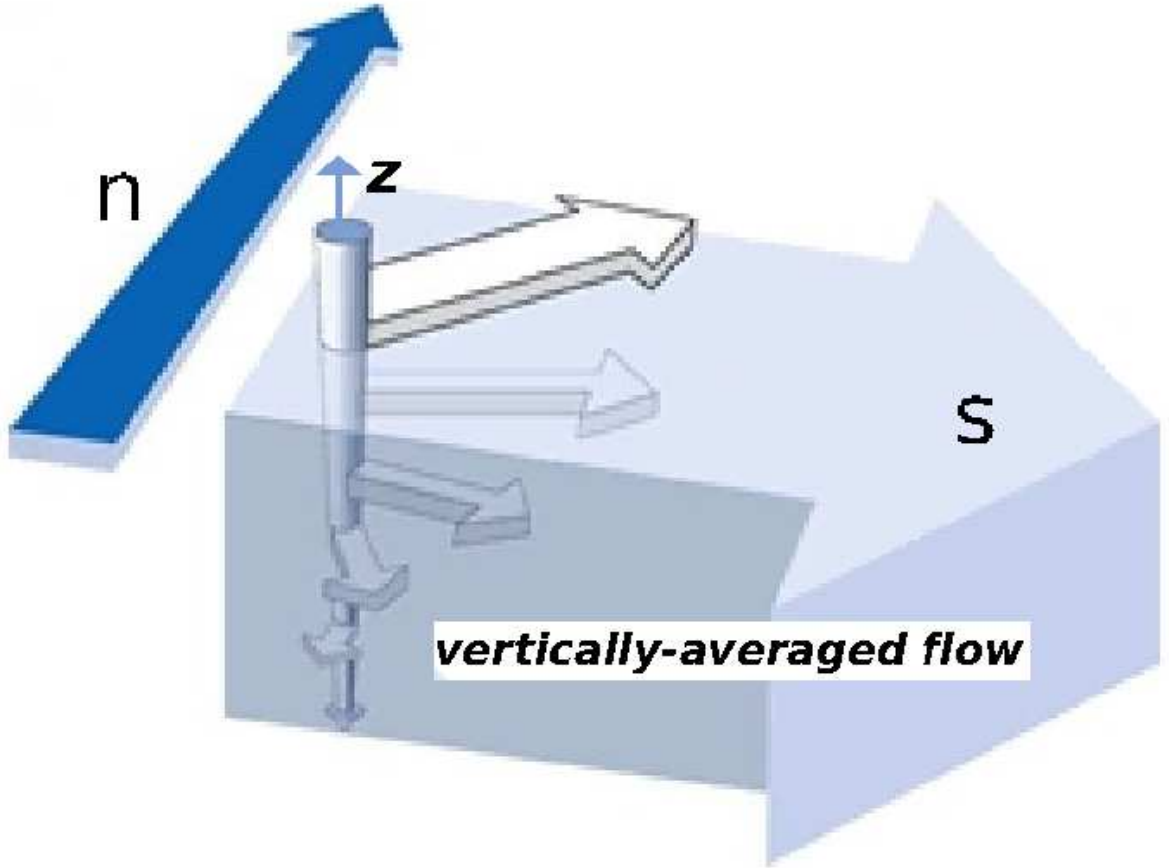


Figure 1.2: Streamwise-normal coordinate system.

$u_s \gg u_n$ , density is uniform, and vertical advection is negligible. The approximate normal direction momentum equation is:

$$\frac{\partial u_n}{\partial t} + u_s \frac{\partial u_n}{\partial s} - \frac{u_s^2}{R_s} + f u_s + g \frac{\partial \eta}{\partial n} - \frac{\partial}{\partial z} \left( A \frac{\partial u_n}{\partial z} \right) = 0, \quad (1.1)$$

where  $A$  is the eddy viscosity,  $f$  is the Coriolis force,  $\eta$  is the water level,  $g$  is the acceleration of gravity, and  $R_s$  is the radius of curvature of the streamline (defined to be positive for clockwise curvature). The depth average of Eq. (1.1) is:

$$\overline{u_s \frac{\partial u_n}{\partial s}} - \overline{\frac{u_s^2}{R_s}} + f \overline{u_s} + g \frac{\partial \eta}{\partial n} + \frac{\tau_n}{\rho h} = 0, \quad (1.2)$$

where  $h$  is the water depth and  $\tau_n$  is the bottom friction in the normal direction given by:

$$\frac{\tau_n}{\rho} = [A \frac{\partial u_n}{\partial z}]_{z=-h} \quad (1.3)$$

By subtracting (1.2) from (1.1) and neglecting the depth-averaged streamwise advection term in (1.2), which tends to be small (Kalkwijk and Booij 1986), we obtain the following expression for the secondary circulation:

$$\underbrace{\frac{\partial u_n}{\partial t} + u_s \frac{\partial u_n}{\partial s}}_{(a)} - \underbrace{\frac{\partial}{\partial z} \left( A \frac{\partial u_n}{\partial z} \right)}_{(b)} - \underbrace{\frac{\tau_n}{\rho h}}_{(d)} = - \underbrace{\frac{u_s^2 - \overline{u_s^2}}{R_s}}_{(e)} - \underbrace{f(u_s - \overline{u_s})}_{(f)} \quad (1.4)$$

(Note that normal water level gradient  $\frac{\partial \eta}{\partial n}$  does not appear).

The terms on the left-hand side (LHS) of Eq. (1.4) are: (a) the local acceleration of the normal velocity, (b) streamwise advection, (c) internal friction of the secondary circulation, and (d) bottom friction. The two driving forces on the right-hand side (RHS) of Eq. (1.4), which arise from departures of the streamwise velocity from its vertical mean, are: (e) the depth-dependent centrifugal force and (f) the depth-dependent Coriolis force. Kalkwijk and Booij (1986) solved Eq. (1.4) analytically for the cases of Coriolis-induced and curvature-induced circulation by assuming steady state, a logarithmic velocity profile in the vertical, and a parabolic form for the eddy viscosity.

The observations by Geyer (1993) indicate that the Kalkwijk and Booij (1986) model may not be applicable to oceanic conditions such as those at Gay Head and

similar sites. Geyer (1993) found that Kalkwijk and Booij (1986)  $u_n$  values for the Gay Head situation were up to four times lower than those observed for the tidal flow at that location. He suggested that both enhanced shears in the observed streamwise flow and reduced vertical mixing due to stratification were responsible for the discrepancy. However, according to Alaee et al. (2004), for curved oscillatory oceanic flows such as tidal flows around promontories, the time-dependent term and, more importantly, the varying characteristics of the flow in the streamwise direction, both neglected in Kalkwijk and Booij (1986), may have contributed to the discrepancy.

Based on Geyer's (1993) results, Alaee et al. (2004) proposed a model in which the nonlinear term (b) plays a key role, while internal friction (c) could be neglected when compared to bottom friction (d). By further assuming steady state (term (a) = 0), the Alaee et al. (2004) form of Eq. (1.4) becomes:

$$\underbrace{u_s \frac{\partial u_n}{\partial s}}_{(b)} - \underbrace{\frac{\tau_n}{\rho h}}_{(d)} = - \underbrace{\frac{u_s^2 - \bar{u}_s^2}{R_s}}_{(e)} - \underbrace{f(u_s - \bar{u}_s)}_{(f)}. \quad (1.5)$$

The Alaee et al. (2004) non-dimensionalization of Eq. (1.5) yielded two nondimensional numbers. One, an equivalent Reynolds number  $R_{ef} \sim \frac{H}{C_D b}$ , where  $b$  is the streamwise length scale, quantifies the relative importance of advection versus friction in Eq. (1.5). The other, a modified Rossby number  $R_{om} \sim 2 \frac{u_s}{f R_s}$ , quantifies the relative importance of the centrifugal force versus the Coriolis force in Eq. (1.5). Alaee et al. (2004) used these two numbers to define four secondary flow regimes, as shown in Table 1.1 (see also Fig. 1.3). They also defined the surface maximum strengths of the secondary flow  $u_n$  (Table 1.1). They used three-dimensional numerical simulations to calculate the constants  $K_A$ ,  $K_B$ ,  $K_C$  and  $K_D$  (see right

panel in Table 1.1). The best fit to the numerical model results indicated the following:

- $K_A = 0.026$
- $K_B = 0.019$
- $K_C = 0.109$
- $K_D = 0.27$

Table 1.1: Flow regimes and the corresponding dominant force balances (Alaee et al. 2004).

Regime	Primary balance between	$u_n$ max. strength
A	$R_{ef} < 1$ and $R_{om} < 1$ bottom friction and Coriolis forces	$u_n \sim K_A \frac{f h}{C_d}$
B	$R_{ef} > 1$ and $R_{om} < 1$ inertia and Coriolis forces	$u_n \sim K_B f b$
C	$R_{ef} < 1$ and $R_{om} > 1$ bottom friction and centrifugal forces	$u_n \sim K_C \frac{b u_s}{C_d R_s}$
D	$R_{ef} > 1$ and $R_{om} > 1$ inertia and centrifugal forces	$u_n \sim K_D \frac{b u_s}{R_s}$

Berthot and Pattiariatchi (2006) used the Alaee et al. (2004) model as part of a study that aimed to understand the three-dimensional variability of a headland-associated sandbank near Cape Levillain (Shark Bay, Western Australia). Their predicted result for the surface maximum normal velocity ( $u_n = 24$  cm/s) was in accordance with the normal flow velocities measured at Cape Levillain (surface flow up to 25 cm/s; bottom flow up to 12.5 cm/s).

Many studies (Pingree 1978; Pingree and Maddock 1979b; Wolanski et al. 1996; Park and Wang 2000; Berthot and Pattiariatchi 2006; White and Deleersnijder 2007; White and Wolanski 2008) have suggested that upwelling occurs in the presence of transient tidal eddies as a result of curvature-induced secondary circulation. In a

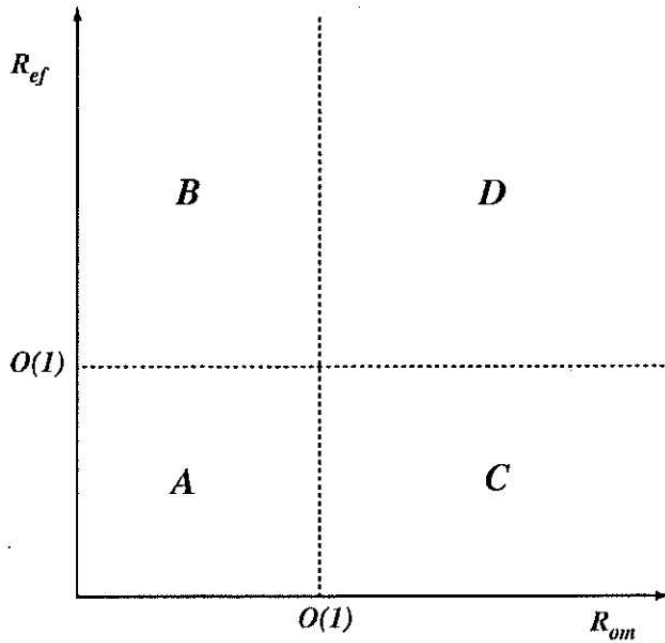


Figure 1.3: The flow regime diagram based upon the two non-dimensional numbers,  $R_{om}$  and  $R_{ef}$  (Alaee et al. 2004).

recent paper, White and Wolanski (2008) reported on the case study of Rattray Island (Great Barrier Reef, northeast Australia), subject to tidal flow in shallow water. Their idealized high-resolution finite-element numerical model suggested that eddy and tip upwellings may be of similar intensity at Rattray Island. Only Pingree (1978) and Doglioli et al. (2004) have reported the presence of Coriolis-induced (i.e.,  $R_{om} < 1$ ) secondary flow around such geological features.

### 1.3 Tidal Eddy Motion in the Western Gulf of Maine

There is observational and model evidence (Brown and Yu 2006) that the Great South Channel (GSC) region of the western Gulf of Maine (GoM; Fig. 1.4) is characterized by prominent eddy motion activity that is directly coupled with tidal

motion. Although there is no direct evidence relating the eddy motion activity with the high density of sea scallops, this region is known to be one of the critical areas of sea scallop recruitment (Stokesbury et al. 2004).

Surface current maps showing prominent eddy motion in the GSC region of the western GoM (e.g., Fig. 1.5a) were obtained for 9-10 April 2005 by Brown and Yu (2006) using high-frequency CODAR (Coastal Ocean Dynamics Acquisition Radar) derived from two stations. The suite of hourly CODAR surface current maps (not shown) reveals both anticlockwise (ACW) and clockwise (CW) eddy motions that are clearly related to the strong tidal flows in the region of the elbow of Cape Cod, MA.

These transient tidal eddy motion patterns (Fig. 1.5b) are very similar to the model eddy patterns seen in the Brown and Yu (2006) application of the high-resolution, homogeneous (i.e., barotropic), finite-element numerical ocean model QUODDY (Lynch et al. 1996). These model CW and ACW eddy motion patterns formed in the coastal boundary layer (CBL) near the elbow of Cape Cod in the presence of a streamwise adverse pressure gradient force. The eddy pattern then deflected (or separated) from the CBL and translated along-isobath in the offshore direction. For example, Figure 1.6a shows the “smooth” model along-coast ebb flow several hours before the end of the ebb tidal current phase. During the next couple of hours, a streamwise adverse PGF grows, the nearcoast flow slows and the CBL begins to separate (Fig. 1.6c). Figure 1.6d reveals a CW eddy that has formed in the flow separation envelope. This eddy motion then translates eastward (generally along the reference transect shown in the maps) to an area about 80 km offshore, where it loses its identity as the ebb tidal flow changes to flood (not shown). The Brown and

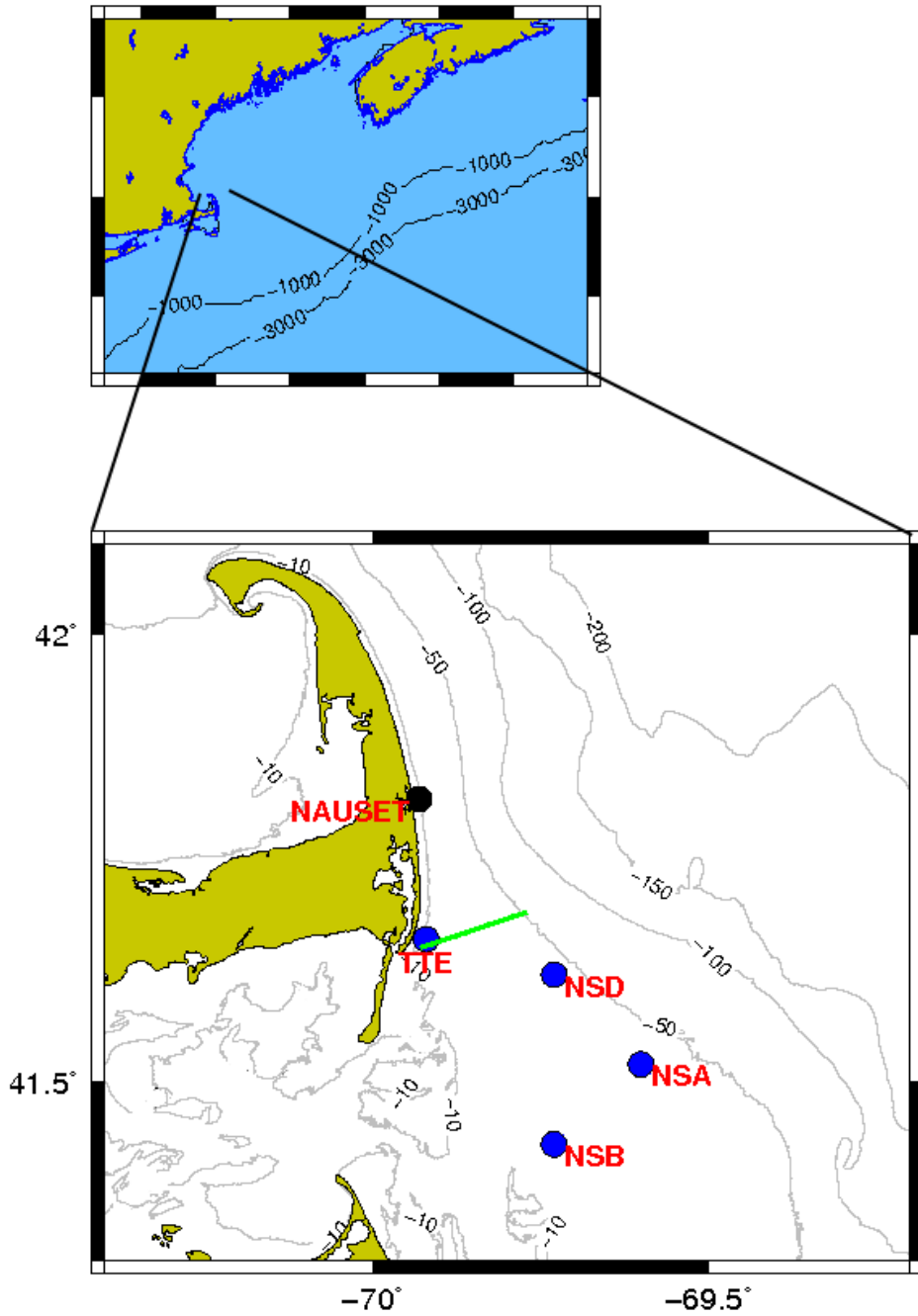


Figure 1.4: (bottom) The location map of the study region showing the TTE mooring location, the historical Moody et al. (1984) sites (current data: NSA, NSB and NSD; sea-surface elevation data: Nauset) and the CTD transect (green line). (top) The location of the study area in the western Gulf of Maine.

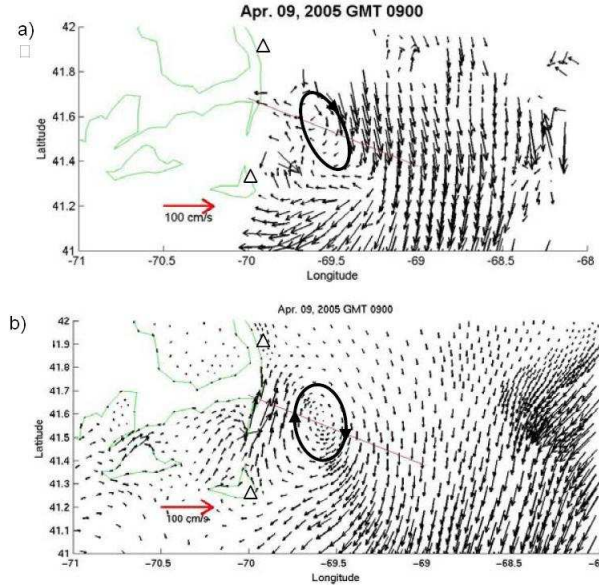


Figure 1.5: Surface ebb (southward) current one hour before the change of tide (COT) from ebb to flood at 1000 GMT, 9 April 2005: (a) CODAR-derived flow from measurements at Nauset and Nantucket (triangles); (b) model  $M_2$  tidal flow. CW eddies are highlighted. The reference transect and current scales are in red (Brown and Yu 2006).

Yu (2006) simulations also show that such eddy motions can include significant vertical velocities (Fig. 1.7).

## 1.4 Thesis Objectives

The purpose of this thesis research is to investigate the kinematics and dynamics of the tidal flow in the western Gulf of Maine (Fig. 1.4), with focus on the secondary circulation. A three-dimensional, nonlinear, finite-element, hydrodynamic computational code is used. Previous research suggests a set of questions concerning transient tidal eddy motion east of Cape Cod, MA:

1. What is the mechanism of formation and evolution of these eddy motions?
2. What is/are the mechanism(s) that control the secondary flows during the

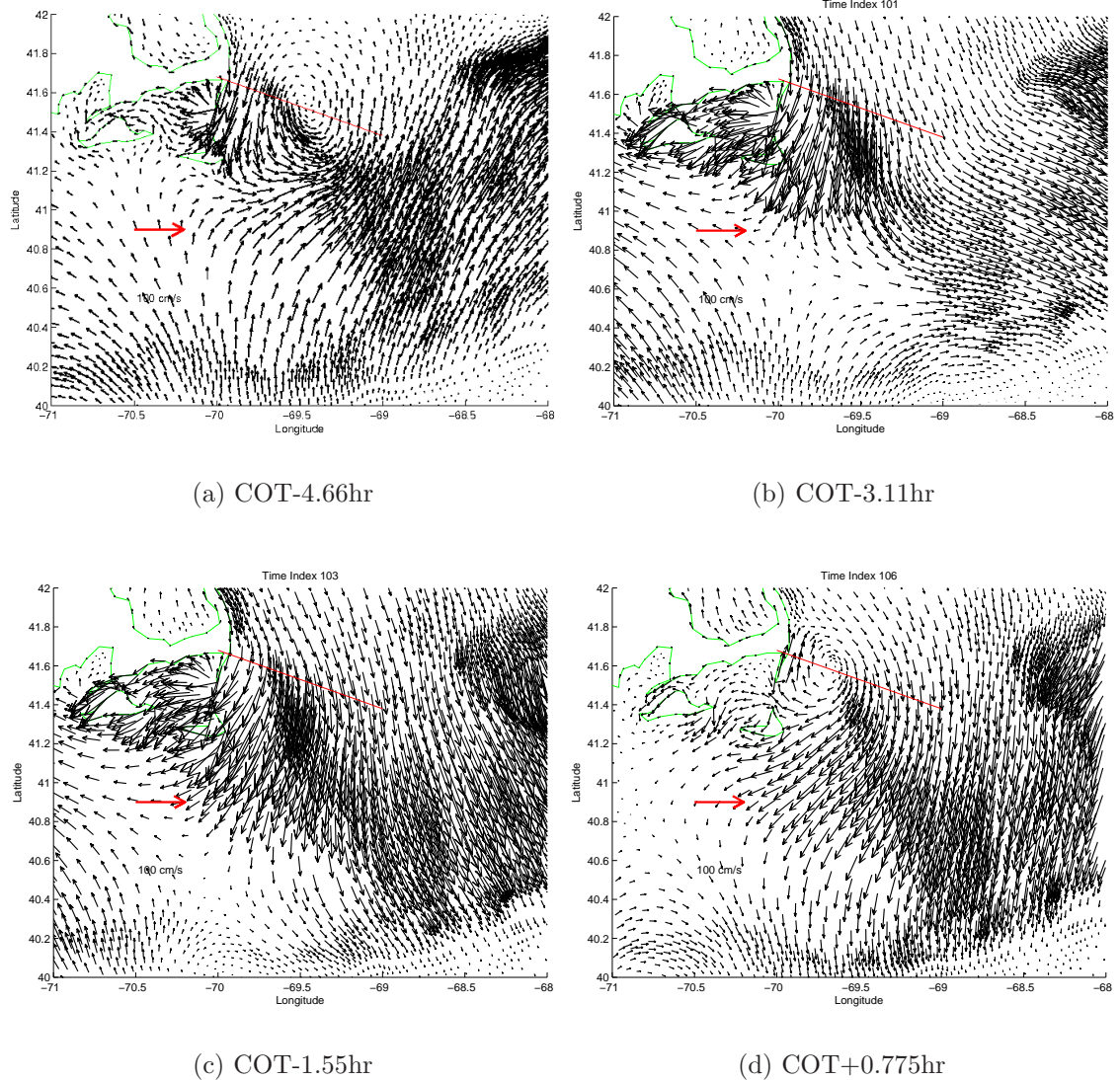


Figure 1.6: The model  $M_2$  change of tidal flow (COT) from flood (northward) to ebb (southward) following a sequence beginning with: (a) “smooth” along-coast flow at COT-4.66 hr (see Figure 1.5 legend); (b) along-coast flow that has been deflected eastward at COT-3.11 hr; (c) “full” ebb flow separation and the formation of a small clockwise (CW) eddy motion near the coast at COT-1.55 hr; (d) translation of the CW eddy motion eastward at COT+0.775 hr (Brown and Yu 2006).

tidal cycle?

3. How do these eddies modify the typical secondary flow of the dominant ebb or

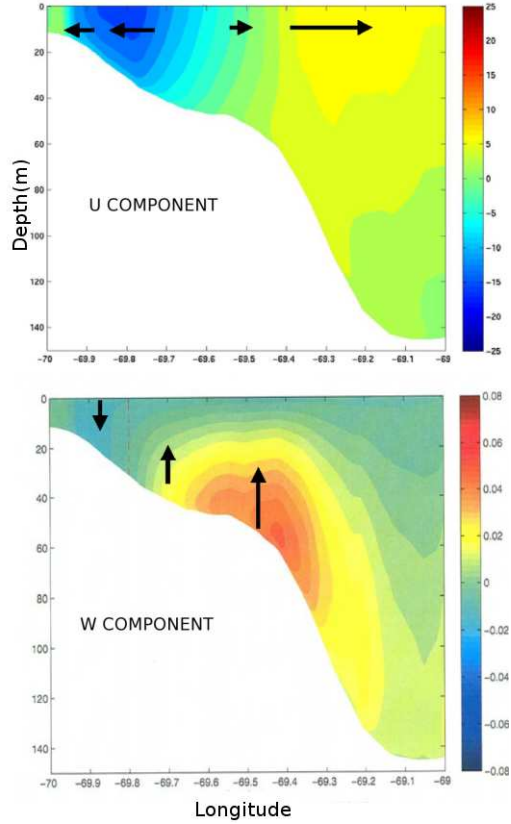


Figure 1.7: (top) Model-derived cross-stream velocity section (cm/s) with schematic vectors showing convergence and divergence regions. (bottom) Vertical flow showing how the convergences and divergences lead to respective downwellings/upwellings (Brown and Yu 2006).

flood?

4. How well can the maximum strength of the secondary flow be predicted using the theory proposed by Alaee et al. (2004)?
5. What mechanism(s) is/are controlling the long-term secondary circulation in this region?

## 1.5 Thesis Overview

In this thesis, observations and numerical model techniques are used to study the kinematics and dynamics of an area east of Cape Cod, MA, that is characterized by transient tidal eddy motion. Momentum balance analysis in a two-dimensional streamwise-normal coordinate system is conducted in order to elucidate the dynamics of this region. In addition, snapshots and time-series of the numerical model results are used to elucidate the mechanisms that control the secondary flow. In Chapter 2, measurements are used to define the basic tidal flow and the level of stratification, during wintertime, for the region where the eddy motions are formed. These data are relevant in justifying the numerical model operation and its boundary conditions.

In Chapter 3, the description of a three-dimensional, finite-element, nonlinear numerical model is presented. Also introduced are a detailed specification of the model boundary conditions and operation, and a comparison between model/observations. Using the numerical model results, snapshots and time-series of velocity and relative vorticity are used to described the basic tidal flow.

In Chapter 4, depth-averaged versions of the equations of motion are used to study the temporal and spatial dynamic variability of the basic tidal motion from a streamwise-normal perspective.

In Chapter 5, the three-dimensional model-derived velocity structure of the tidal flow is described. Finally, the roles of the primary and secondary flows in controlling vertical motions (upwelling/downwelling) is investigated.

The results are discussed in Chapter 6, and a summary of conclusions is presented in Chapter 7.

# Chapter 2

## Measurements

In this chapter, the measurements conducted during wintertime are presented. The main purpose for making these measurements is to describe the basic tidal flow structure and level of stratification in the region where the transient tidal eddy motion is formed.

Shipboard measurements were conducted using the 50-foot research vessel *R&R* (Fig. 2.1). The Transient Tidal Eddy (TTE) bottom-mounted, upward-looking ADCP/bottom pressure instrument was deployed in 12.5 m of water at station TTE (see Fig. 1.4 and Table 2.1), just east of Chatham, MA, on 3 November 2008 and recovered on 27 January 2009. A shipboard CTD survey was conducted on 27 January 2009, using an internally recording Sea Bird Electronics SBE-25 Conductivity/Temperature/Depth (CTD) instrument. Tidal constants for sea-surface elevation and currents at relevant stations, as presented by Moody et al. (1984), are also used in this study. Information regarding these stations is presented in Table 2.1 and Figure 1.4.



Figure 2.1: Research Vessel *R&R* fantail.

Table 2.1: Moored current and sea-surface elevation (TTE and NAUSET) station locations, including the Moody et al. (1984) sites (NSA, NSB, NSD and NAUSET). The depth above the bottom (AB) of the measurements and the record lengths are provided.

Station	Location		Depth AB	Length
	Lon.	Lat.	(m)	(Days)
TTE	-69.92	41.66	6.35, 8.35	58
NSA	-69.60	41.52	8, 28	60
NSB	-69.73	41.43	12	42
NSD	-69.73	41.62	17	42
NAUSET	-69.93	41.816	1	58

## 2.1 Current and Pressure Time Series

The TTE bottom-moored instrument consisted of a 2-meter-high aluminum frame on which was bolted an upward-looking RDI<sup>©</sup> 300k Hz Workhorse ADCP, an Aanderaa<sup>©</sup> bottom pressure instrument, and recovery gear (for details see Brown et al. 2009). The bottom-moored ADCP was configured as follows:

- bin size: 2.0 m;
- pings per ensemble: 200;
- seconds per ping: 0.33 sec;
- ensemble interval: 10 min;
- number of bins: 9;
- predicted accuracy (RDI): 6.1 cm/s.

This configuration, and the fact that the ADCP was mounted on a 2-meter-high aluminum frame, resulted in two bins with good data; bin 1 and bin 2, at 6.35 and 8.35 meters above the bottom (AB), respectively.

The 56-day time series records of the moored ADCP northward and eastward currents at 6.35 and 8.35 meters AB look identical (Fig. 2.2), which is consistent with the shallow depth of the water at station 1. The 2.5-month, 5-minute TTE bottom pressure (BP) time series record is shown in Figure 2.3, where the mean atmospheric pressure contribution has been removed for clarity.

A harmonic method of tidal analysis based on Dennis and Long (1971) was used in order to investigate the observed current/sea-surface elevation time series as the superposition of basic waves whose frequencies results from astronomical forcing.

The harmonic analysis results presented in Tables 2.2 to 2.4 show that these series are clearly dominated by the semidiurnal tides, the  $M_2$  tides in particular. The Moody et al. (1984) tidal constituents for sea-surface elevation and currents are presented in Tables 2.4 and 2.5, respectively. These data also show the dominance of the semidiurnal tides, with  $M_2$  being the most important constituent in terms of

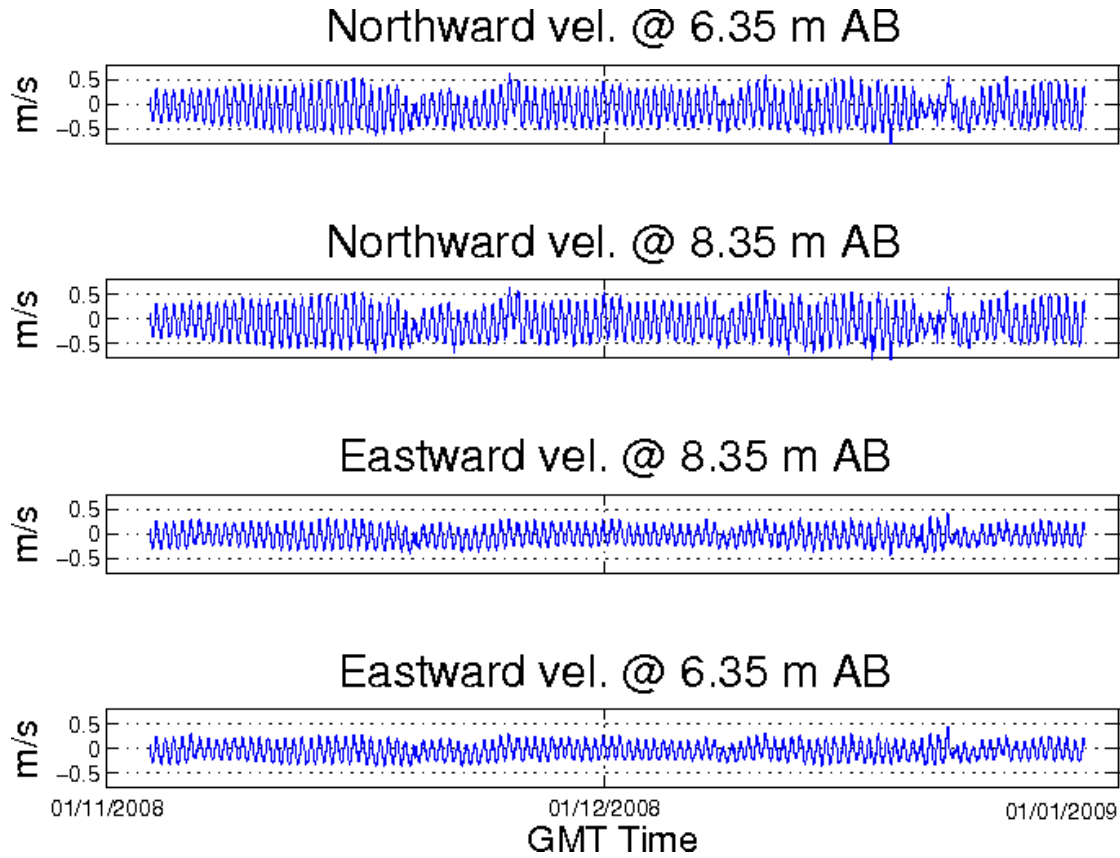


Figure 2.2: ADCP velocity time series at station TTE: (top 2 panels) northward currents at 6.35 and 8.35 meters AB; (bottom 2 panels) eastward currents at 6.35 and 8.35 meters AB.

both currents and sea-surface elevation. Not surprisingly, the M2 tidal current ellipse for nearshore (TTE site) tidal flow is nearly rectilinear in the direction of the bathymetry (Fig. 2.4).

Table 2.6 presents the moored ADCP and BP time series bulk statistics. The residual currents/sea-surface elevation records (or non-tidal contribution) were obtained by removing the contributions of the 20 most important tidal constituents in the time series. The mean residual currents presented in Table 2.6 are consistent with the approximately 10 cm/s southwestward vertically averaged residual currents measured by Chen et al. (1995) in a similar location during April 1988. The ratios

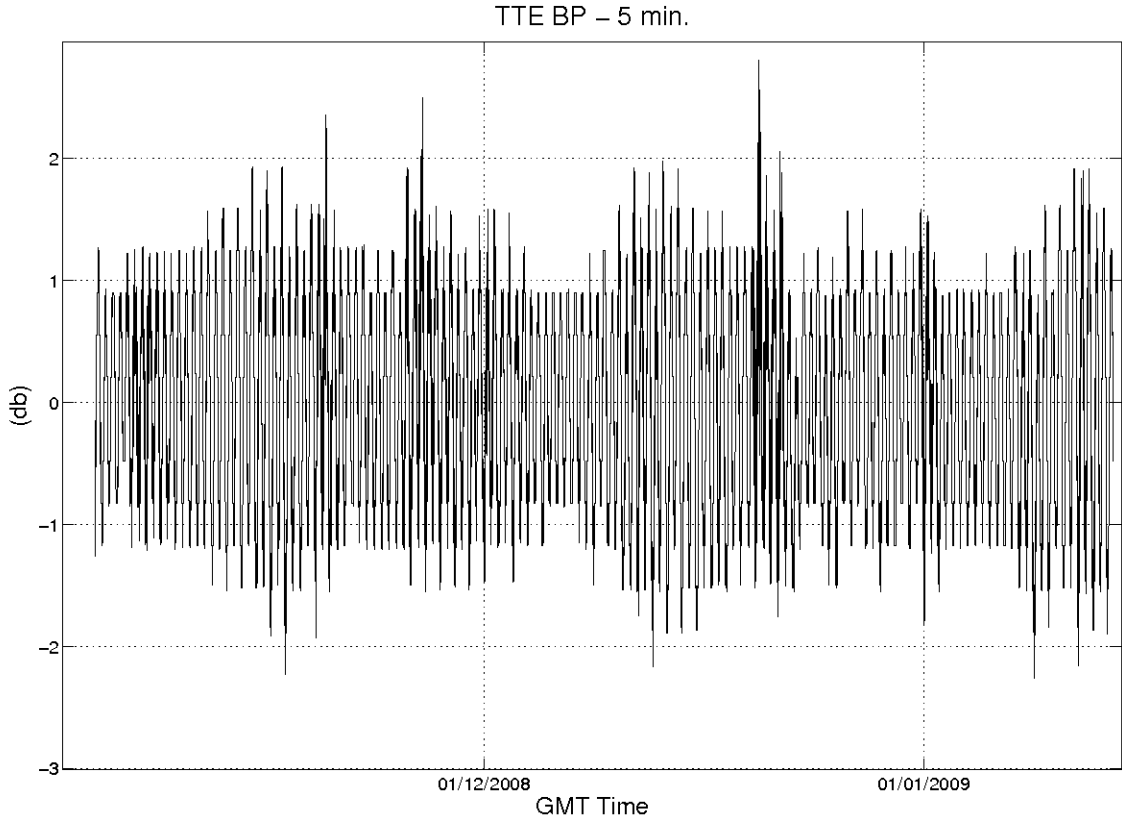


Figure 2.3: Time series of full 5-minute TTE bottom pressure series (db).

between the residual variance and the observed variance for the ADCP and BP time series, in the last column of Table 2.6, show small values. This indicates that the non-tidal current/sea-surface elevation noise in these measurements is small compared to the observed signal.

## 2.2 Hydrographic Measurements

The 27 January 2009 hydrographic measurements (Table 2.7) were conducted using a Seabird<sup>©</sup> SBE-25 Sea-logger with sensors for pressure (P), temperature (T), and conductivity (C) that were factory-calibrated on 9 October 2008. The specifications for a calibrated SBE-25 are presented on Table 2.8. The SBE-25 is an internally

Table 2.2: The harmonic constants for the 5 principal and 2 nonlinear tidal constituents of the ADCP 6.35-meter AB eastward and northward current components, based on an analysis of the 56-day records between 3 November and 29 December 2008. For each tidal constituent, the component amplitudes and Greenwich epoch phases uncertainties are given, along with the current ellipse in terms of major axis amplitude and orientation, ellipticity ( $\epsilon$ =major/minor; + means anticlockwise rotating current vector), and phase of the maximum current.

Tidal	Eastward (cm/s)		Northward (cm/s)		Ellipse (cm/s)			
	Cons.	Amp.	$G(^{\circ})$	Amp.	$G(^{\circ})$	Maj. Axis	Maj. Dir.	$\epsilon$
$M_2$	$21.5 \pm 0.5$	$271 \pm 1$	$38.8 \pm 1.0$	$275 \pm 1$	44.3	29.0	34.1	274
$N_2$	$3.8 \pm 0.5$	$238 \pm 6$	$6.9 \pm 1.0$	$246 \pm 7$	7.9	28.8	19.8	244
$S_2$	$2.4 \pm 0.5$	$307 \pm 11$	$7.4 \pm 1.0$	$306 \pm 7$	7.7	18.2	Inf	306
$O_1$	$0.5 \pm 0.4$	$329 \pm 54$	$0.1 \pm 0.1$	$287 \pm 105$	0.5	82.0	-5.0	328
$K_1$	$0.8 \pm 0.5$	$302 \pm 33$	$1.3 \pm 1.0$	$260 \pm 39$	1.5	26.0	-3.0	269
$M_4$	1.1	143	2.2	169	2.4	24.6	6.0	169
$M_6$	0.8	13	0.7	32	1.0	47.1	5.0	32

Table 2.3: Same as Table 2.2, but for 8.35-meter AB.

Tidal	Eastward (cm/s)		Northward (cm/s)		Ellipse (cm/s)			
	Cons.	Amp.	$G(^{\circ})$	Amp.	$G(^{\circ})$	Maj. Axis	Maj. Dir.	$\epsilon$
$M_2$	$23.0 \pm 0.5$	$272 \pm 1$	$40.7 \pm 1.1$	$275 \pm 1$	46.7	29.5	42.5	274
$N_2$	$3.9 \pm 0.5$	$238 \pm 7$	$7.2 \pm 1.1$	$246 \pm 9$	8.2	28.6	16.4	244
$S_2$	$2.4 \pm 0.5$	$307 \pm 12$	$7.7 \pm 1.1$	$306 \pm 8$	8.1	17.5	Inf	306
$O_1$	$0.3 \pm 0.4$	$343 \pm 76$	$0.1 \pm 0.1$	$46 \pm 106$	0.3	84.3	Inf	344
$K_1$	$0.8 \pm 0.5$	$296 \pm 35$	$1.6 \pm 1.1$	$257 \pm 40$	1.8	23.6	-3.4	264
$M_4$	0.9	136	2.0	173	2.2	21.0	4.4	168
$M_6$	0.9	15	0.6	22	1.1	56.8	11.0	17.2

recording instrument that was configured for these measurements as follows:

- sample rate: 8 scans/sec;
- minimum conductivity frequency for pump turn-on: 4000 Hz;

Table 2.4: The harmonic constants for the 5 principal and 2 nonlinear tidal constituents of the TTE bottom pressure (BP) record, based on an analysis of the 56-day records between 3 November and 27 December 2008. The harmonic amplitudes and Greenwich epoch phases, with uncertainties, are given for each of the TTE BP tidal constituents, as well as the 5 principal tidal constituents of historical bottom pressure measurements just offshore of NAUSET (Moody et al. 1984).

Tidal Const.	TTE BP Amp. (db)	G (°)	Nauset BP Amp. (db)	G (°)
M <sub>2</sub>	1.103±0.013	118±1	1.032	102
N <sub>2</sub>	0.238±0.013	96±3	0.222	70
S <sub>2</sub>	0.170±0.013	156±4	0.144	133
O <sub>1</sub>	0.114±0.013	209±5	0.115	182
K <sub>1</sub>	0.132±0.013	192±6	0.131	201
M <sub>4</sub>	0.027	16	-	-
M <sub>6</sub>	0.030	178	-	-

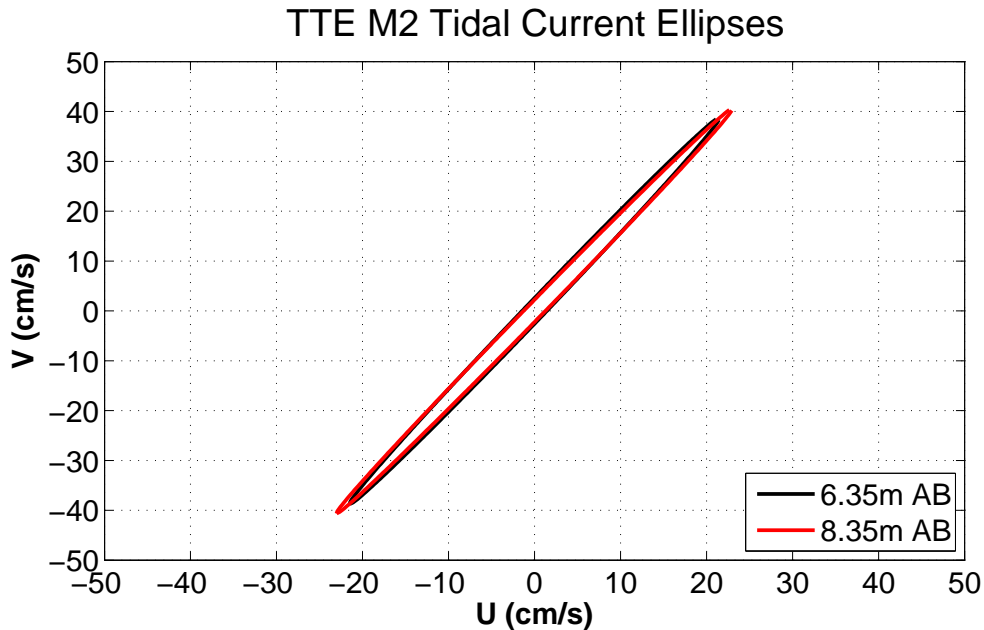


Figure 2.4: The TTE  $M_2$  tidal current ellipses at 6.35 and 8.35 meters AB.

- record up-cast: on;
- record down-cast: on.

Table 2.5: The harmonic constants for the five principal constituents based on a harmonic analysis of hindcast eastward and northward current component series at three nearby historic stations (Moody et al. 1984) are given in terms of current component amplitude (cm/s) and phase ( $^{\circ}$ G). See Table 2.1 for station details.

Tidal Const.	Eastward Amp. (cm/s)	Phase ( $^{\circ}$ G)	Northward Amp. (cm/s)	Phase ( $^{\circ}$ G)
<b>NSA 8 meters AB</b>				
$M_2$	6.4	16	59.3	319
$N_2$	1.5	346	11.9	288
$S_2$	0.3	172	9.4	44
$K_1$	1.4	63	4.5	357
$O_1$	1.2	35	1.8	339
<b>NSA 28 meters AB</b>				
$M_2$	7.7	40	58.8	344
$N_2$	2.3	23	16.3	304
$S_2$	2.7	169	16.3	102
$K_1$	0.7	60	4.4	357
$O_1$	1.9	63	6.4	3
<b>NSB 12 meters AB</b>				
$M_2$	37.0	20	62.9	345
$N_2$	6.8	355	1.1	319
$S_2$	1.8	130	4.7	66
$K_1$	3.4	40	2.9	329
$O_1$	2.4	24	1.1	333
<b>NSD 17 meters AB</b>				
$M_2$	21.5	327	41.5	345
$N_2$	5.4	292	9.3	320
$S_2$	4.1	144	2.6	82
$K_1$	2.3	25	3.2	306
$O_1$	0.6	274	0.5	187

The SBE-25 was attached to a  $\frac{1}{4}$ -inch polypropylene line and was lowered at a rate of about 0.5 m/s to within 2-5 meters of the bottom at each station. The SeaBird software package SEASOFT was used to convert the raw hexadecimal P/T/C time-series output into engineering units. The salinity was computed from the

Table 2.6: The moored ADCP (at 6.35 and 8.35 meters AB) and bottom pressure (BP) time series bulk statistics of the observed and the residual velocities and pressures (tides-removed) in a depth of approximately 12.5 meters.

	Height	Observed		Residual		Res. $\sigma^2$ /Obs. $\sigma^2$
		AB(m)	mean (cm/s)	$\sigma^2$ (cm/s) <sup>2</sup>	mean (cm/s)	
v	6.35	-8.0	857	-8.0	90	0.11
	8.35	-8.5	951	-8.5	11	0.12
u	6.35	-4.2	259	-4.2	26	0.10
	8.35	-4.1	296	-4.1	30	0.10
		(dbars)	(dbars <sup>2</sup> )	(dbars)	(dbars <sup>2</sup> )	-
BP	2.00	0.0016	0.72	0.0016	0.07	0.10

Table 2.7: Station information for the 27 January 2009 shipboard CTD survey.

St.	Lat. °N	Lon. °W	Dep.(m)	Time(GMT)	NSDist. (Km)	Cum. Dist. (Km)
01	41.65	69.92	13.5	1737	2.20	-
02	41.66	69.90	20.0	1730	2.20	2.20
03	41.67	69.87	21.1	1721	2.20	4.41
04	41.67	69.85	26.7	1713	2.20	6.59
05	41.68	69.83	33.8	1700	2.18	8.79
06	41.68	69.80	42.5	1644	2.20	10.98
07	41.69	69.77	53.0	1618	2.20	13.19

measured conductivity and temperature, based on the salinity scale of 1980 (Fofonoff and Millard 1983). Back in the laboratory, the CTD data were processed using a series of SeaBird SEASOFT programs as described in Brown et al. (2009). The hydrographic survey revealed well-mixed winter conditions (Fig. 2.5) between stations 1 and 6, while station 7 shows a less well-mixed condition. The temperature section (Fig. 2.5 top panel) shows typical winter conditions, where the near-surface temperatures are colder than temperatures at depth. The lowest temperature were near the coast, where the influence of the cold atmospheric temperature was more pronounced. Despite apparent unstable temperature

Table 2.8: The SBE-25 specifications.

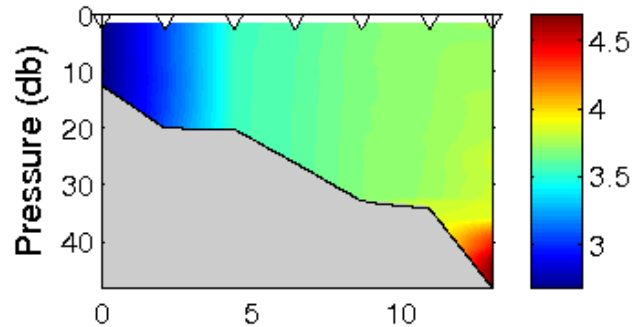
	Temp.(°C)	Conductivity(S/m)	Pressure(db)
Range	-5 to +35	0 to 7	0 to 350
Accuracy	$\pm 0.002$	$\pm 0.0003$	$\pm 0.1\%$ of full-scale range
Resolution	$\pm 0.0003$	$\pm 0.00004$	$\pm 0.015\%$ of full-scale range

stratification, water column stability is mainly controlled by salinity distribution. These measurements are consistent with the results found by Shcherbina and Gawarkiewicz (2008) during wintertime.

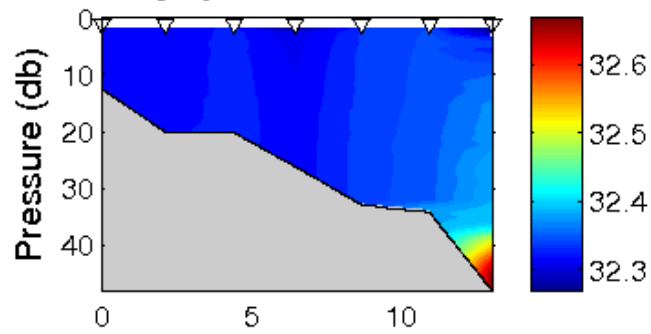
## 2.3 Chapter Summary

This chapter defines the basic tidal flow and level of stratification, during wintertime, based on observations for the region where the eddy motion is formed. The measurements presented have shown that the basic deep ocean tidal motion drives the currents and the sea-surface elevation in this region. Harmonic analysis indicates that the series are dominated by the semidiurnal tides, with  $M_2$  being the most important constituent in terms of both currents and sea-surface elevation. The hydrographic survey revealed well-mixed winter conditions, where stratification is mainly controlled by salinity distribution.

**Temperature ( $^{\circ}\text{C}$ ) – 27 Jan 2009**



**Salinity (psu) – 27 Jan 2009**



**Density ( $\text{kg/m}^3$ ) – 27 Jan 2009**

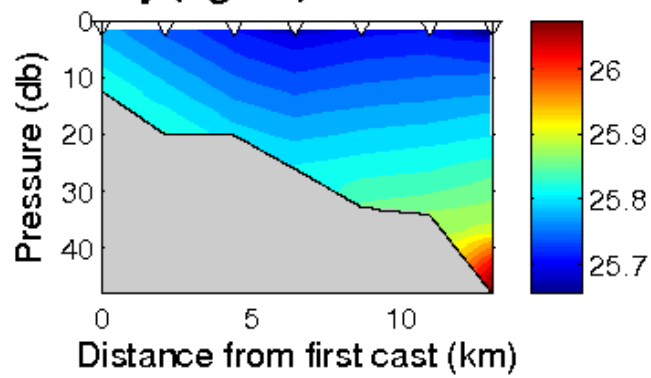


Figure 2.5: The 27 January 2009 vertical sections of (top) temperature, (middle) salinity and (bottom) density anomaly (sigma-t).

# Chapter 3

## Numerical Model Simulations

### 3.1 Model Description

The three-dimensional, nonlinear, prognostic,  $f$ -plane, finite-element coastal ocean circulation model QUODDY, as described in Lynch et al. (1996), was used in this thesis research. This model uses the Mellor-Yamada level-2.5 turbulent closure model (MY25) in the vertical, with a linearized partial-slip condition enforced at the bottom. The horizontal viscosity can be either uniform or velocity and mesh-size dependent. The model can be run in the barotropic mode, in which water properties are homogeneous, or the baroclinic mode, in which water properties are variable. The QUODDY model mesh used here was defined by the Holboke (1998) GHSD mesh (Fig. 3.1). The resolution of this mesh varies from about 10 km in the gulf to about 5 km near the coastlines (i.e., around Cape Cod), with even finer resolution (1.5 km) in the regions of steep bathymetric slopes like the north flank Georges Bank. A 10-meter minimum depth was adopted for the coastal boundary elements. Twenty-one (21) sigma layers are used in the vertical. In this application, a velocity shear dependent method (Smagorinsky 1963) is used to calculate horizontal viscosity. The model assumes that bottom flow  $\bar{u}_b$  is subject to quadratic bottom

boundary stress, according to  $C_d|\bar{u}_b|\bar{u}_b$ , where the time/space constant bottom drag coefficient  $C_d$  used here is 0.005 (see section on sensitivity tests for details).

## 3.2 Boundary Conditions

### 3.2.1 Tidal elevations

The three principal semidiurnal ( $M_2$ ,  $N_2$  and  $S_2$ ) and two principal diurnal ( $K_1$  and  $O_1$ ) tidal elevation constituents were used to force QUODDY at the deep ocean and western cross-shelf sections (red line in Fig. 3.1). These tidal-forcing elevations were calculated using the EastCoast 2001 tidal harmonics database by Mukai et al. (2002), which was based on a harmonic analysis of the AAdvanced CIRCulation (ADCIRC) finite-element hydrodynamic numerical model simulations. The EastCoast 2001 grid resolution varies from 1 to 4 km along the land boundaries to a maximum of 25 km in the deep ocean. The quality of the EastCoast 2001 database is based on 101 tidal elevation stations with high-quality observational data derived from several sources. The EastCoast 2001 computed harmonic constants compared to within 6 to 13 percent to measured amplitude data and to within 7 to 13 degree to measured phase data on a globally-averaged basis (Mukai et al. 2002). The EastCoast 2001 tidal database comes with a FORTRAN code that extracts the tidal information for the set of user-specified coordinates.

### 3.2.2 Normal flow

Normal flow boundary conditions are used along boundary in the Bay of Fundy section (see blue line in Fig. 3.1) (Holboke 1998). This type of boundary is used to simulate the net effects of the Bay of Fundy, a small land-locked regime. Therefore,

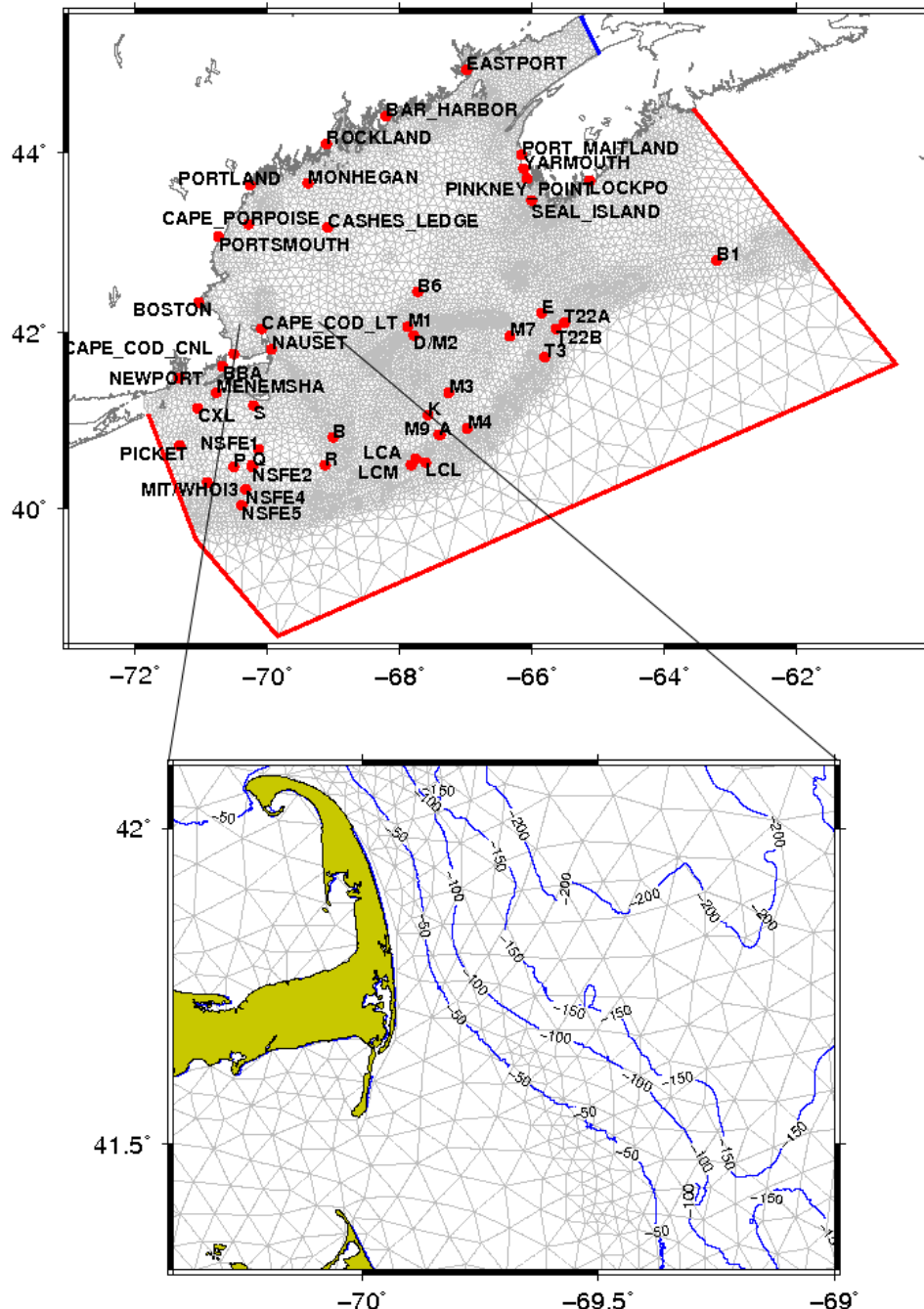


Figure 3.1: (top) The Holboke (1998) GHSD mesh for the QUODDY model domain, with the open ocean boundaries highlighted by a thick red line and the Bay of Fundy boundary highlighted by a thick blue line. The observed sites (Moody et al. 1984) used for the model-observation comparison studies are also shown. (bottom) The Great South Channel study region showing the mesh resolution and bathymetric countours.

although the net transport through the boundary must be zero, the tidal transport may still be significant at times. The importance of this boundary condition is that, while it enforces the correct tidal amplitudes, it also allows low-frequency elevation to respond to variations in forcing, like wind. Although the tides were the only forcing used in this study, the normal flow boundary condition was applied in order to facilitate future research.

The Bay of Fundy normal boundary flows for the  $M_2$ ,  $M_4$ ,  $M_6$ ,  $N_2$ ,  $S_2$ ,  $K_1$  and  $O_1$  tidal constituents were calculated using a 3-D linear, finite-element, diagnostic numerical model (Lynch et al. 1992) referred to as FUNDY6 on the GHSD mesh (Figure 3.1) at the open ocean boundaries (lines blue and red on Fig. 3.1) with the EastCoast 2001 derived elevations. The resulting depth-averaged velocities (amplitudes and phases for  $u$  and  $v$ ) at the Bay of Fundy section (blue line in Fig. 3.1) were then extracted and used in QUODDY, which then converts them to normal flow.

### 3.3 Model Operation

This QUODDY model application was run in the barotropic mode and with tidal forcing only. Each prescribed tidal sea level forcing ( $M_2$ ,  $S_2$ ,  $N_2$ ,  $K_1$  and  $O_1$ ) was linearly increased (i.e., ramped-up) to full forcing during the first six  $M_2$  tidal cycles. This initial “ramp-up” of the forcing was applied so that the model nonlinearities and advection could dynamically adjust to the initial fields, as shown by Holboke (1998). The model was run with a 21.83203125-second (= the 12.42-hour  $M_2$  tidal period/2048) time-step for two months, with the results being saved every 10.18 minutes.

Table 3.1: Description of the numerical simulations that were conducted in order to examine the model's sensitivity to bottom drag coefficient ( $C_d$ ).

Simulation #	$C_d$
01	0.005
02	0.003
03	0.01

### 3.4 Model Sensitivity and Validation

The QUODDY model solutions were tested for sensitivity to the values of bottom coefficient. Three different model simulations (Table 3.1), with varying bottom friction values, were analyzed based on sea level tidal analyses for the five most important tidal constituents in the region ( $M_2$ ,  $N_2$ ,  $S_2$ ,  $K_1$  and  $O_1$ ). For each simulation, model sea level time series (1 month long) were extracted at the 49 model nodes that were nearest to the corresponding Moody et al. (1984) observed stations (Fig. 3.1 top). The average model-versus-observed results for the 49 stations (Table 3.2) suggest that the semi-diurnal constituents are sensitive to bottom friction values, whereas the diurnal constituents are less sensitive to this parameter. The  $M_2$ ,  $N_2$ ,  $S_2$ ,  $K_1$  and  $O_1$  tidal sea-level harmonic constants derived from simulation 01 for each of the nearest model nodes are schematically compared with those from Moody et al. (1984) in Figures A.1 to A.10 (see Appendix A). In general, simulation 01, in which  $C_d=0.005$ , produced the most reliable (smaller amplitude errors and phase differences) tidal sea levels over the entire model domain. Therefore, this was the bottom friction value used for all the results presented in this thesis.

In addition to sea-level harmonic constants, the numerical model results were also

Table 3.2: Comparison between the three simulations based on averages and standard deviations for the amplitude % error and phase difference (model-observations).

	Simulation 01 Cd=0.005				Simulation 02 Cd=0.003				Simulation 03 Cd=0.01			
	Amp. Err. %		Pha. Dif. °		Amp. Err. %		Pha. Dif. °		Amp. Err. %		Pha. Dif. °	
	Ave.	Std.	Ave.	Std.	Ave.	Std.	Ave.	Std.	Ave.	Std.	Ave.	Std.
$M_2$	8.8	6.12	3.6	4.0	17.9	11.7	6.2	3.8	23.7	23.4	7.5	6.1
$N_2$	6.3	5.1	18.3	6.6	5.2	4.9	13.4	7.2	15.7	21.9	13.9	9.8
$S_2$	10.9	7.2	17.8	7.7	17.2	10.1	18.9	8.1	18.6	11.3	18.7	12.6
$K_1$	20.9	10.3	17.1	13.7	21.7	11.1	16.5	13.9	20.0	9.7	17.7	13.6
$O_1$	33.5	14.0	13.8	10.9	34.3	14.3	13.3	11.8	32.5	13.6	14.1	10.8

compared with observed  $M_2$  tidal current ellipses and surface currents derived from Coastal Ocean Dynamics Application Radar (CODAR). Figure 3.2 and Table 3.3 present a comparison between (1) tidal current ellipses for average measured currents at stations NSA, NSB and NSD (derived from Moody et al. 1984), and station TTE (described in Chapter 2), and (2) the model’s depth-averaged currents derived from the nodes nearest the observations. Overall, the numerical model tends to overestimate the magnitudes and underestimate the phases. The discrepancy is most significant in shallower regions. However, the numerical model seems to capture the principal characteristics of the main tidal flow (divergence/convergence). In future applications, the adoption of a depth-dependent bottom friction scheme may provide better results.

Figure 3.3 compares hourly-averaged snapshots of sea surface currents derived from the CODAR stations with hourly-averaged model results (6 outputs averaged over 1 hour) during the formation and evolution of a CW eddy motion. The CODAR maps are derived from the returns of a pair of 5 MHz long-range stations facing eastward from Nauset and Nantucket, MA (red dot and blue dot, respectively in Fig. 3.3a). A

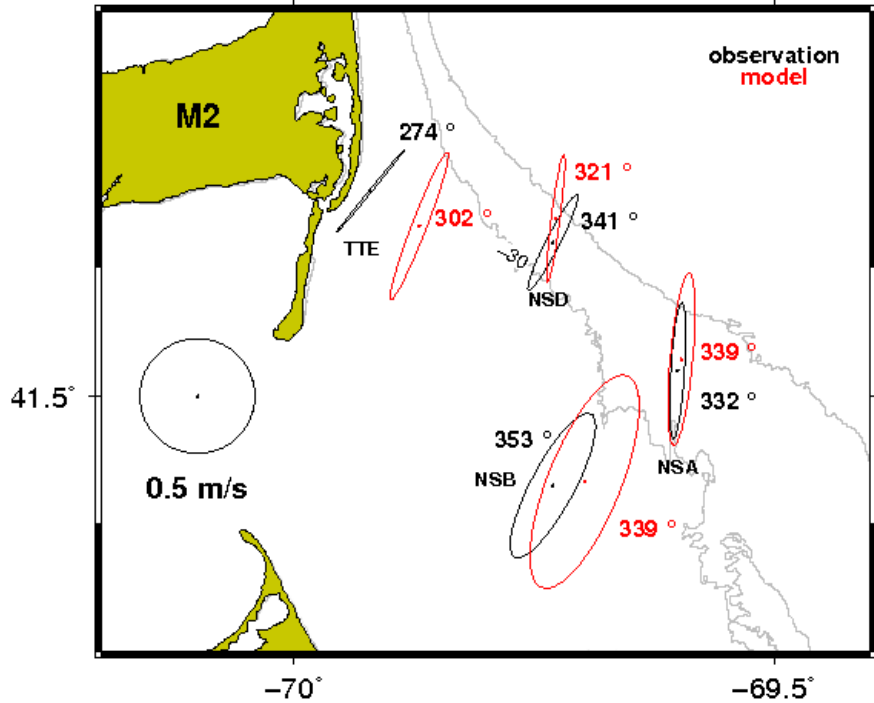


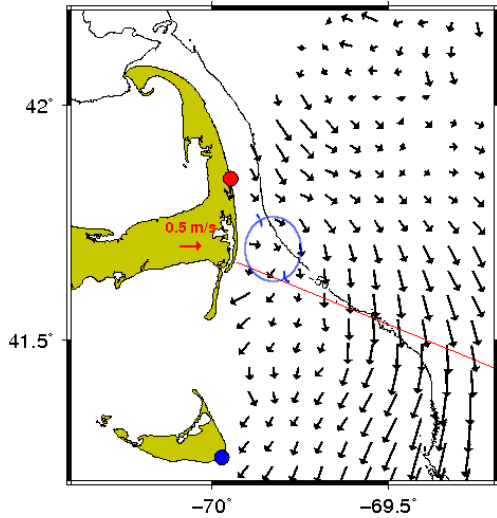
Figure 3.2: The  $M_2$  tidal current ellipses for average measured currents (black) at stations TTE, NSA, NSB and NSD. The tidal current ellipses for the depth-averaged model results (red) closest to these stations are also shown. The Greenwich phases of the maximum ellipse currents are such that the lower values lead the higher values (see also Table 3.3).

detailed description regarding operation and characteristics of these CODARs can be found in Brown et al. (2009). Overall, these results suggest a qualitative agreement between CODAR and model.

### 3.5 Basic Model Eddy Motion

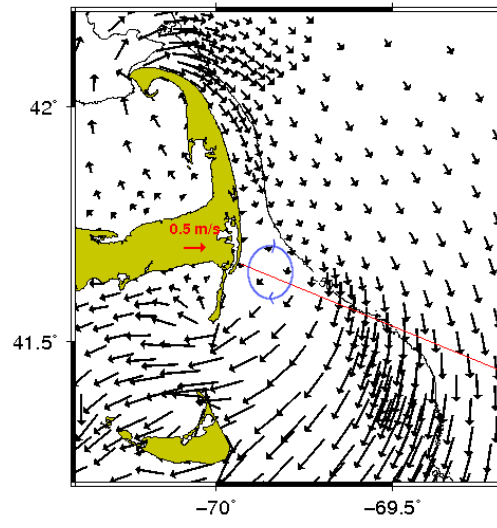
In this section, the basic eddy motion in the Great South Channel is discussed in terms of circulation and relative vorticity (or the curl of the fluid velocity). The results presented here were generated under spring tide conditions (highlighted in

CODAR SURFACE CURRENTS 09/03/08 1000 GMT



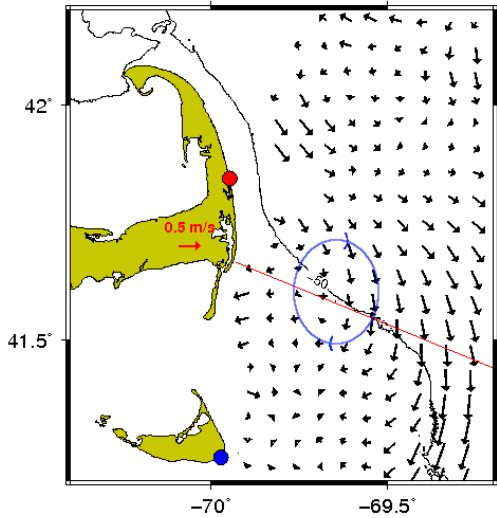
(a) CODAR 10:00 GMT

MODEL SURFACE CURRENTS 09/03/08 1000 GMT



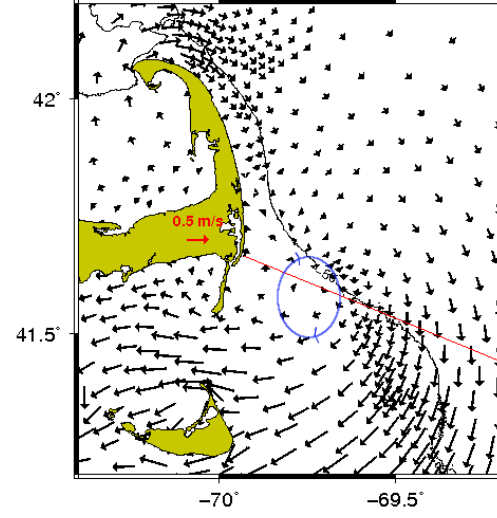
(b) MODEL 10:00 GMT

CODAR SURFACE CURRENTS 09/03/08 1100 GMT



(c) CODAR 11:00 GMT

MODEL SURFACE CURRENTS 09/03/08 1100 GMT



(d) MODEL 11:00 GMT

Figure 3.3: Comparison between surface currents derived from CODAR high-frequency radar sites at Nauset (red dot) and Nantucket (blue dot) to the model results during the presence of a CW eddy motion on 3 September 2008. This transient eddy motion is highlighted by the blue ellipses for visualization purposes.

Table 3.3: The  $M_2$  tidal current ellipses from both model results and observations.

				Current Ellipse Parameters				
Station		Lon.	Lat.	Depth (m)	$U_{maj.}$ (cm/s)	$U_{min.}$ (cm/s)	Phase $^{\circ}G$	Orient. $^{\circ}\text{True}$
NSA	observation model	-69.60	41.52	33	59.2	-5.9	332	3.5
		-69.59	41.53	40	75.0	-9.7	339	5.1
NSB	observation model	-69.73	41.44	22	70.5	-18.9	353	28
		-69.70	41.43	23	99.3	-31.7	339	21.9
NSD	observation model	-69.73	41.62	33	46.4	5.9	341	27
		-69.73	41.64	50	55.5	3.8	321	7.3
TTE	observation model	-69.92	41.66	12.5	46.7	1.2	274	29.3
		-69.87	41.63	21	68.2	-6.4	302	21

yellow in Fig. 3.4, with Table 3.4 as reference). Previous results under neap tide conditions (highlighted in red in Fig. 3.4) are similar to these spring tide results, but with less intensity. Figure 3.5 indicates the location of the reference node (R) used to define the phase of the tide, and the location of the nodes used in the time series analysis (points I and O; see also Table 3.5 for the exact location of these nodes).

Table 3.4: Times in hours selected for analysis from Figure 3.4 and their designated letters.

Time (hours)	Letter	Time (hours)	Letter
0	A	6.5	E
1.9	B	8.5	F
3.1	C	9.7	G
4.4	D	10.9	H

### 3.5.1 Snapshots of circulation and relative vorticity

The sequence of depth-averaged current and relative vorticity maps presented in Figure 3.6 cover the tidal cycle, at the reference node (R), from maximum flood to

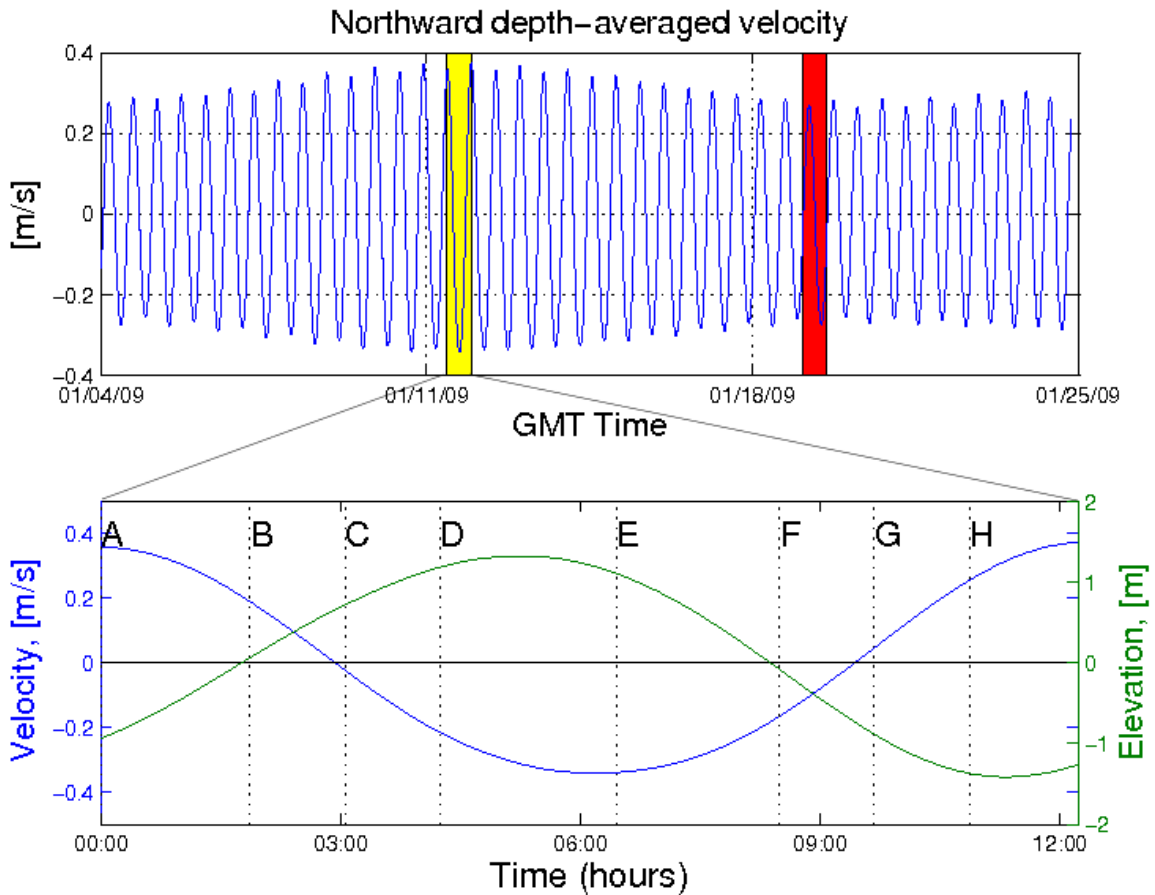


Figure 3.4: (top) Northward depth-averaged velocity time series at the reference (R) model node (located in Fig. 3.5). The spring and neap phases are highlighted by yellow and red, respectively. (bottom) The times selected for analysis, which were under spring tide conditions, are indicated with letters A to H (see also Table 3.4).

Table 3.5: Location of the nodes used to reference the tides (R) and of the inner (I) and outer (O) nodes used in the time series analysis.

Node	Latitude	Longitude
R	41.7600	-69.7680
I	41.7010	-69.8510
O	41.7980	-69.3820

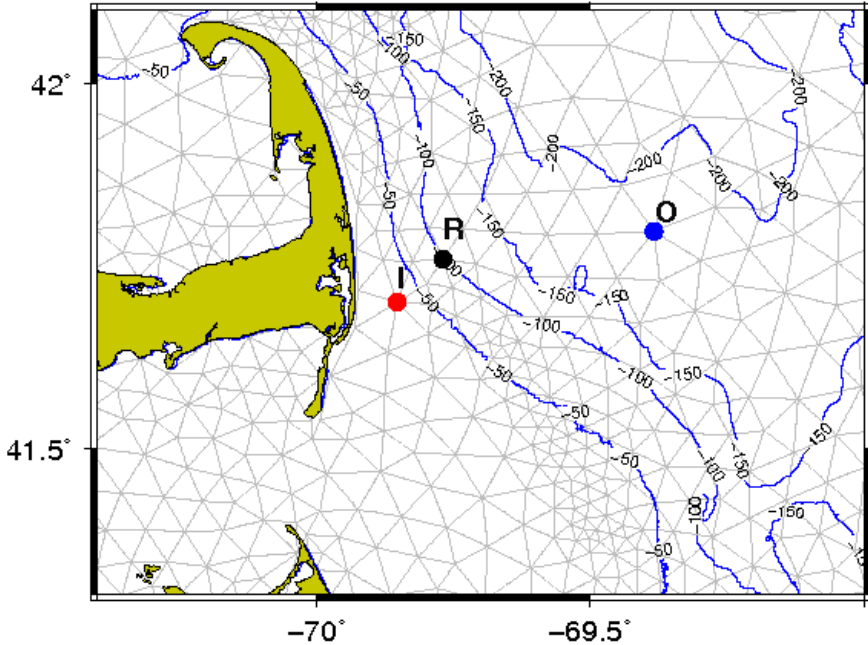


Figure 3.5: Locations of the reference node (R), in black, and the nodes at which time series of elevation, velocity, vorticity and the terms in Eqs. (4.3) and (4.4) are presented. Point I (red) characterizes the flow influenced by the eddy motion, and Point O (blue) the flow away from the influence of the coast (see also Table 3.5).

the first half of ebb. The reference time that we have chosen for the cycle (Time A) coincides with the maximum flood flow pattern in Figure 3.6a that is associated with strong positive vorticity in the region of Monomoy Island (MI). The 50-meter isobath (Fig. 3.6a) appears to be a natural boundary of the CBL, delimiting the nearshore area where vorticity is produced. Note that the negative vorticity seen

offshore is associated with the eddy motion formed on the previous half tidal cycle. At time B, which is 1.9 hours after maximum flood, anticlockwise (ACW) eddy motion starts forming in the CBL off Chatham, MA (Fig. 3.6b). By time C, the eddy motion, with its relatively high vorticity, has translated southeastward along the 50-meter isobath (Figs. 3.6c and 3.6d).

The ebb-flow sequence in Figure 3.7, from maximum ebb (Time E) to the first half of flood (Time H), depicts the generation and evolution of clockwise (CW) eddy motion . In this case, the eddy motion forms just after time F (between Figs. 3.7b and 3.7c), which is approximately 9 hours after maximum flood and 2.5 hours after maximum ebb. Therefore the CW eddy motion forms approximately 0.6 hours later in the cycle as compared to the ACW case.

### 3.5.2 Time series at fixed locations

To further illustrate the behavior of the flow, time series of elevation, velocity and vorticity are shown for two nodes that characterize different dynamical regimes (Fig. 3.8). The time selected for analysis corresponds to time indices presented in the lower panel of Figure 3.4. Point I is located off Chatham, MA, inside the CBL where the eddy motion is formed, and Point O is located away from the CBL in a region not influenced by the eddy motion (see Fig. 3.5 for reference).

At the nearcoast node (Point I) the time series of elevation and velocity are dominantly sinusoidal. However, there is a noticeable asymmetrical response (indicating nonlinearity effects) in the relative vorticity field (Fig. 3.8a). The elevation and northward velocity are approximately  $180^\circ$  out of phase, indicating the presence of a progressive tidal wave. The relative vorticity oscillates between positive and negative, which indicates the presence of the ACW and CW eddy

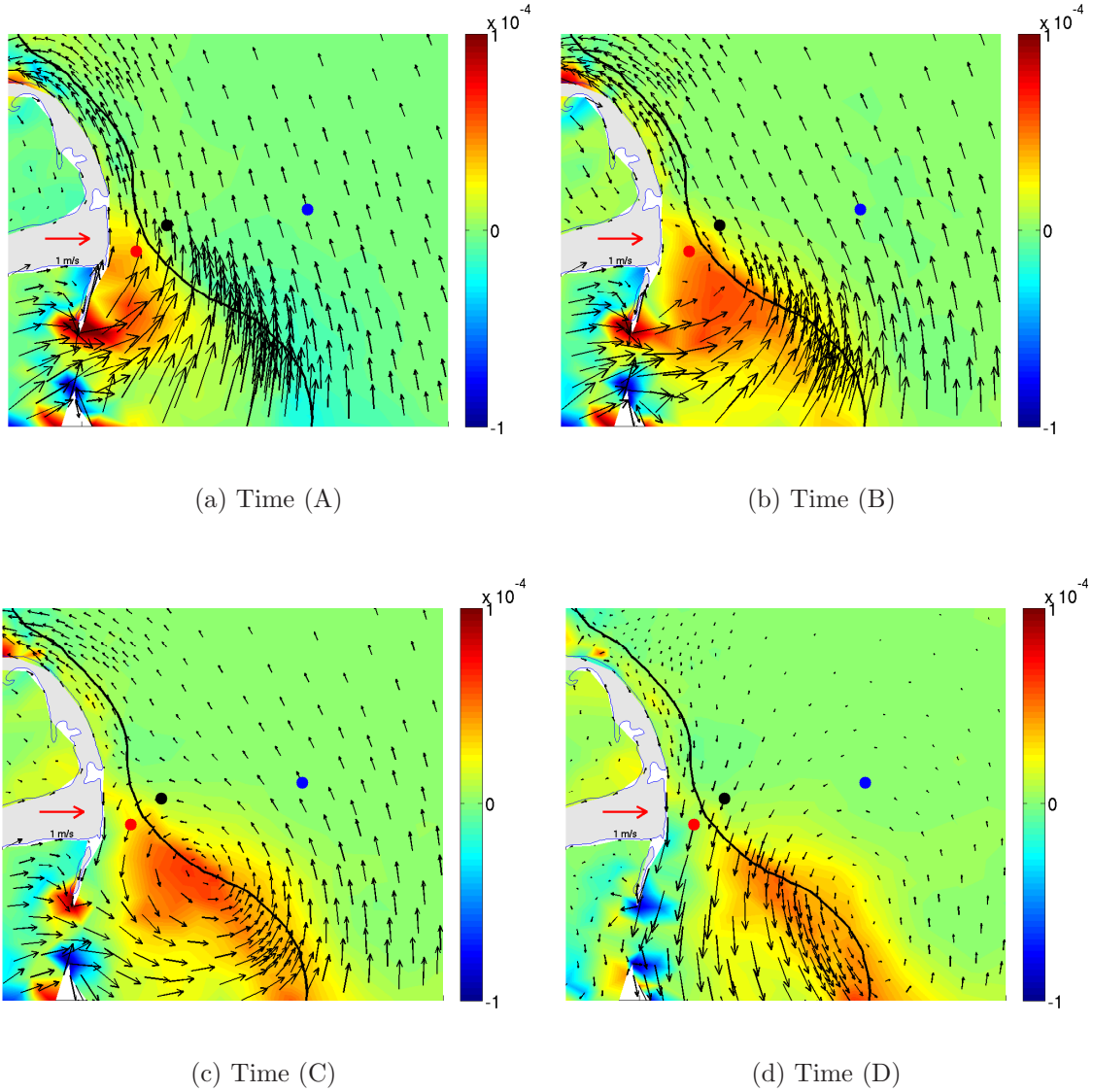


Figure 3.6: Depth-averaged vector currents with color-coded relative vorticity from maximum flood (Time A) to first half ebb (Time D) (see Figure 3.4 for reference). The 50-meter isobath (black line) defines the boundary of the CBL, and the dots locate the reference nodes defined in Figure 3.5.

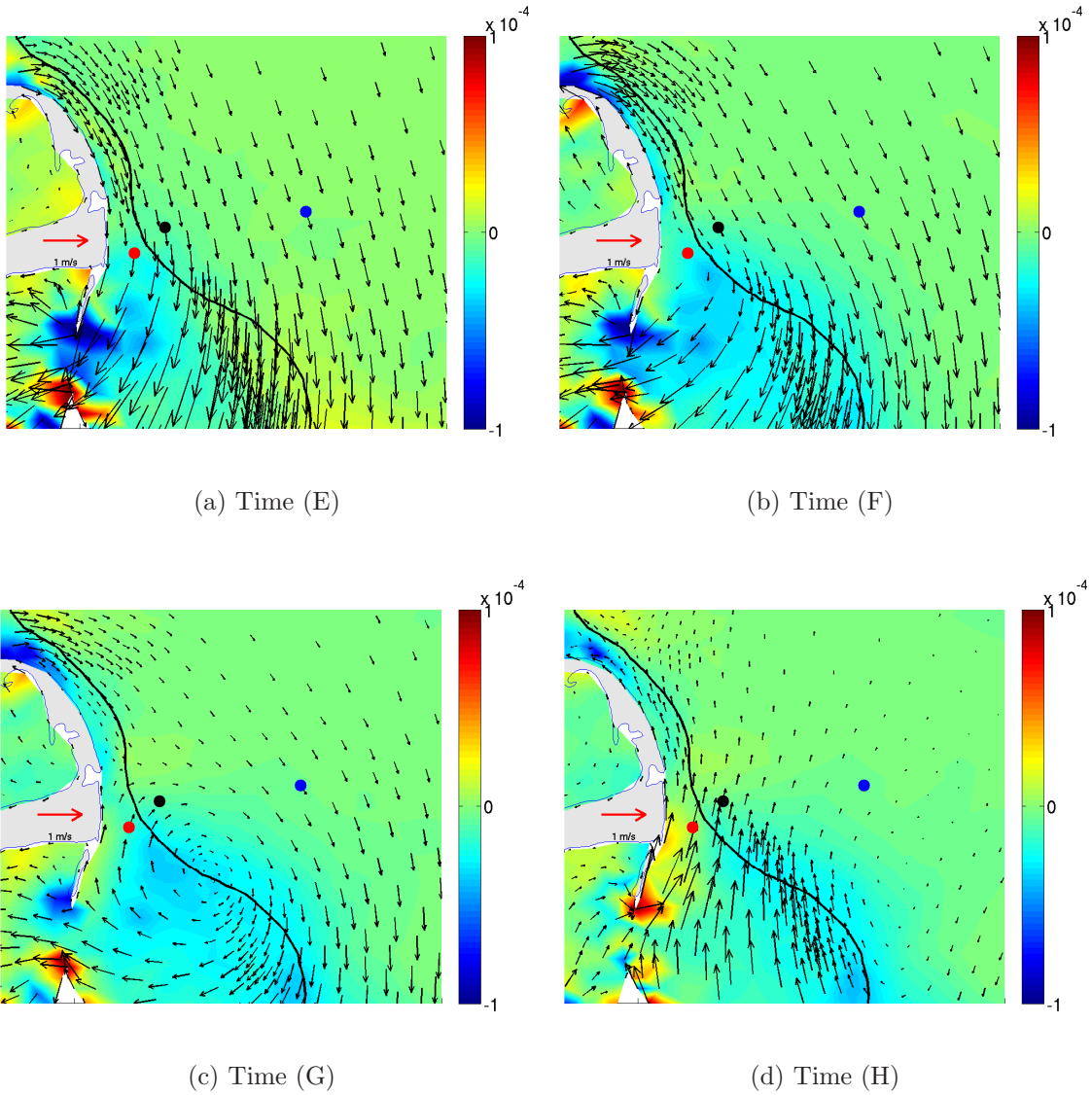


Figure 3.7: Depth-averaged vector currents with color-coded relative vorticity from maximum ebb (Time E) to first half flood (Time H) (see Figure 3.4 for reference). The 50-meter isobath (black line) defines the boundary of the CBL, and the dots locate the reference nodes defined in Figure 3.5.

motions, respectively. Relative vorticity generated during the flood cycle is approximately  $2 \times 10^{-5} \text{ s}^{-1}$  stronger than that generated during the ebb cycle. At the offshore reference node (Point O) the time series of elevation, velocity and relative vorticity are very symmetrical (Fig. 3.8b). The tidal flow specified at the

model open boundaries results in a nearly standing tidal wave with amplitude around 0.4 m/s, where the northward velocity and elevation are approximately  $90^\circ$  out of phase (Brown 1984). The component of cross-shore depth-averaged velocity ( $U$ ) is directed onshore during the westward half cycle and offshore during the eastward half cycle, with maximum amplitude similar to Point O ( $\sim 0.25$  m/s). The alongshore depth-averaged velocity ( $V$ ), however, has smaller amplitudes than at point I. The vorticity amplitude is negligible, much less than  $3 \times 10^{-6}$  s $^{-1}$ .

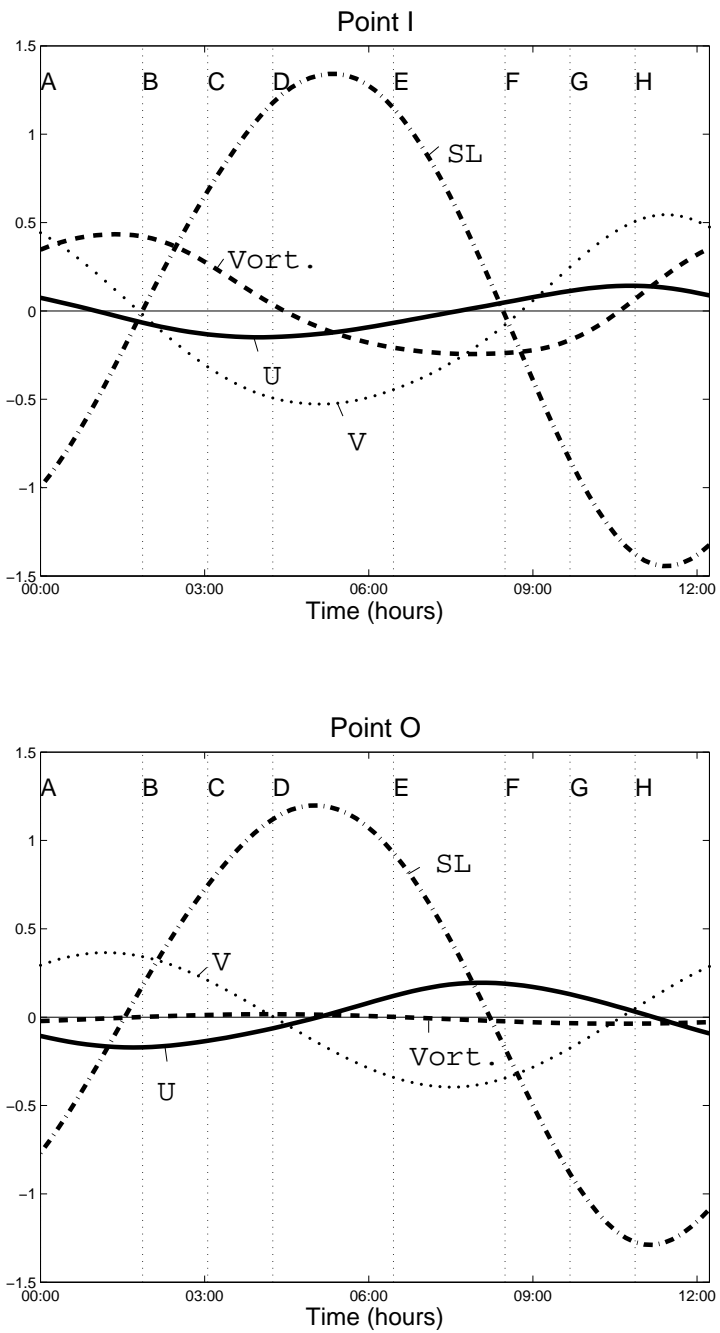


Figure 3.8: Model-derived time series at points I and O (see Fig. 3.5 and Table 3.5 for locations of points). The sea-surface elevation (m, dash-dot), depth-averaged northward (alongshore) velocity ( $\text{m.s}^{-1}$ , dotted), depth-averaged eastward (cross-shore) velocity ( $\text{m.s}^{-1}$ , solid), and relative vorticity ( $\text{s}^{-1}$ , dashed). Vorticity values have been multiplied by  $10^4$ .

# Chapter 4

## Dynamics of the Basic Eddy Motion

In this chapter, the temporal and spatial dynamic variabilities of the basic eddy motion are studied from a streamwise-normal coordinate system perspective (see Chapter 1 for coordinate system explanation).

### 4.1 Depth-Averaged Momentum Balance Calculations

Following Hench and Leutttich (2003), we employed the shallow-water, depth-averaged  $x$ - $y$  momentum equations (Eqs. (4.1) and (4.2)), with the horizontal diffusion terms (which tend to be much smaller than the other terms) omitted.

$$\frac{\partial U}{\partial t} + U \frac{\partial U}{\partial x} + V \frac{\partial U}{\partial y} - fV + g \frac{\partial \eta}{\partial x} + \frac{(C_D \sqrt{U^2 + V^2})U}{H} = 0 \quad (4.1)$$

$$\frac{\partial V}{\partial t} + U \frac{\partial V}{\partial x} + V \frac{\partial V}{\partial y} + fU + g \frac{\partial \eta}{\partial y} + \frac{(C_D \sqrt{U^2 + V^2})V}{H} = 0, \quad (4.2)$$

where  $U$  and  $V$  are depth-averaged velocity components in the  $x$  and  $y$  direction,

respectively,  $g$  is the acceleration due to gravity,  $f$  is Coriolis parameter,  $\eta$  is the surface elevation,  $C_D$  is the bottom friction coefficient and  $H$  is the total water depth ( $H = h + \eta$ ).

Equations (4.1) and (4.2) were then rotated into a streamwise-normal ( $s$ - $n$ ) coordinate system (see Fig. 1.2; a complete description of this coordinate transformation can be found in Hench and Leutich (2003)). The resulting  $s$ - $n$  momentum equations are:

$$\overbrace{\frac{d}{dt}U_s}^d + \overbrace{U_s\frac{\partial U_s}{\partial s}}^e + \overbrace{g\frac{\partial \eta}{\partial s}}^f + \overbrace{\frac{C_D U_s^2}{H}}^g = 0 \quad (4.3)$$

$$U_s \overbrace{\frac{\partial \alpha}{\partial t}}^h + \overbrace{\frac{U_s^2}{R_s}}^i + \overbrace{fU_s}^j + \overbrace{g\frac{\partial \eta}{\partial n}}^k = 0, \quad (4.4)$$

where  $U_s(x, y, t)$  is the streamwise velocity,  $\alpha(x, y, t)$  is the angle between the local streamwise flow vector and the positive  $x$  axis, and  $R_s(x, y, t)$  is the radius of streamwise flow curvature. In the streamwise momentum Eq. (4.3), term d is the local streamwise acceleration, term e is the streamwise advective (or Bernoulli) acceleration, term f is the streamwise pressure gradient and term g is the nonlinear bottom friction. In the normal momentum Eq. (4.4), term h is the local rotary acceleration, term i is the centrifugal force, term j is the Coriolis force and term k is the normal-direction pressure gradient.

The model  $x$ - $y$  velocity and elevation fields in the unstructured grid were used to construct the momentum terms-d through k of Eqs. (4.3) and (4.4) at each computational node. The gradient terms at each node location were computed using a method based on the Kelvin-Stokes theorem (see Appendix B for details). The

local acceleration terms were treated with a forward-Euler finite-difference scheme. Conservation of momentum was evaluated at each node, based on the ratio between (1) the sum of the terms  $d$  to  $g$  in Eq. (4.3) and  $h$  to  $k$  in Eq. (4.4), and (2) the sum of the absolute values of these terms. Momentum was conserved (typically to within one percent) at all grid points in the  $x$  and  $y$  directions, as well as in the  $s$  and  $n$  directions.

To provide a more physically intuitive picture of the momentum balances, results in the following subsections are presented in terms of momentum fluxes (obtained by multiplying each term of Eqs. (4.3) and (4.4) by the instantaneous full water depth  $H$ , where  $H = \eta + h$ ). In the following sections the temporal and spatial variability of each term in Eqs. (4.3) and (4.4) are investigated.

## 4.2 Temporal Variabilities at Fixed Locations

The temporal variability of the terms in Eqs. (4.3) and (4.4) are shown for nodes I and O, located inside and outside of the CBL, respectively (Fig. 3.5). The times selected for analysis corresponds to time indices in the lower panel of Figure 3.4.

At point I, the momentum terms time series in the streamwise (Fig. 4.1a) and normal (Fig. 4.1c) directions exhibit considerable asymmetry, except for terms-g (bottom friction) and h (rotary acceleration). The predominant momentum balance in the streamwise direction is between local acceleration (term d) and pressure gradient (term f), with important influence from bottom friction (term g) during strong flood/ebb. In the normal direction, the predominant momentum balance is between Coriolis force and pressure gradient force (i.e., geostrophy). The streamwise adverse (i.e., positive) pressure gradient generated after maximum flood is higher

than the counterpart generated after maximum ebb. Interestingly, at the times of eddy motion formation (i.e., flow separation) the terms in the streamwise direction tend to instantaneously vanish (Fig. 4.1a). At the same time, in the normal direction, rotary acceleration (term h) and pressure gradient (term k) become stronger, and Coriolis force weaker (Fig. 4.1c).

At the outer node (point O) the momentum terms time series in the streamwise (Fig. 4.1b) and normal (Fig. 4.1d) directions exhibit a stronger symmetry when compared to point I (note the scale changes). The streamwise direction primary balance is between local acceleration (term d) and pressure gradient (term f) (Fig. 4.1b). In the normal direction, the primary balance is between Coriolis force (term j) and pressure gradient (term k), except during the change of tides, when the balance is between pressure gradient and rotary acceleration (term h)(Fig. 4.1d).

## 4.3 Spatial Variability

In this section the spatial variability of the terms in Eqs. (4.3) and (4.4) is investigated. As the time series results presented in the previous section revealed, in terms of momentum balance, the flood-to-ebb (time indices A to D) scenario is equivalent to the ebb-to-flood scenario (time indices E to H), and therefore just the flood-to-ebb scenario is described here.

### 4.3.1 Maximum flood (A)

The distribution of momentum fluxes associated with each term in the  $s$  and  $n$  direction at maximum flood (or point A in Fig. 3.4) is shown in Figure 4.2. At this phase the coastal flow (i.e., flow near point I) has reached a point of near-zero local acceleration (Fig. 4.2d), consistent with the maximum in the vertically averaged

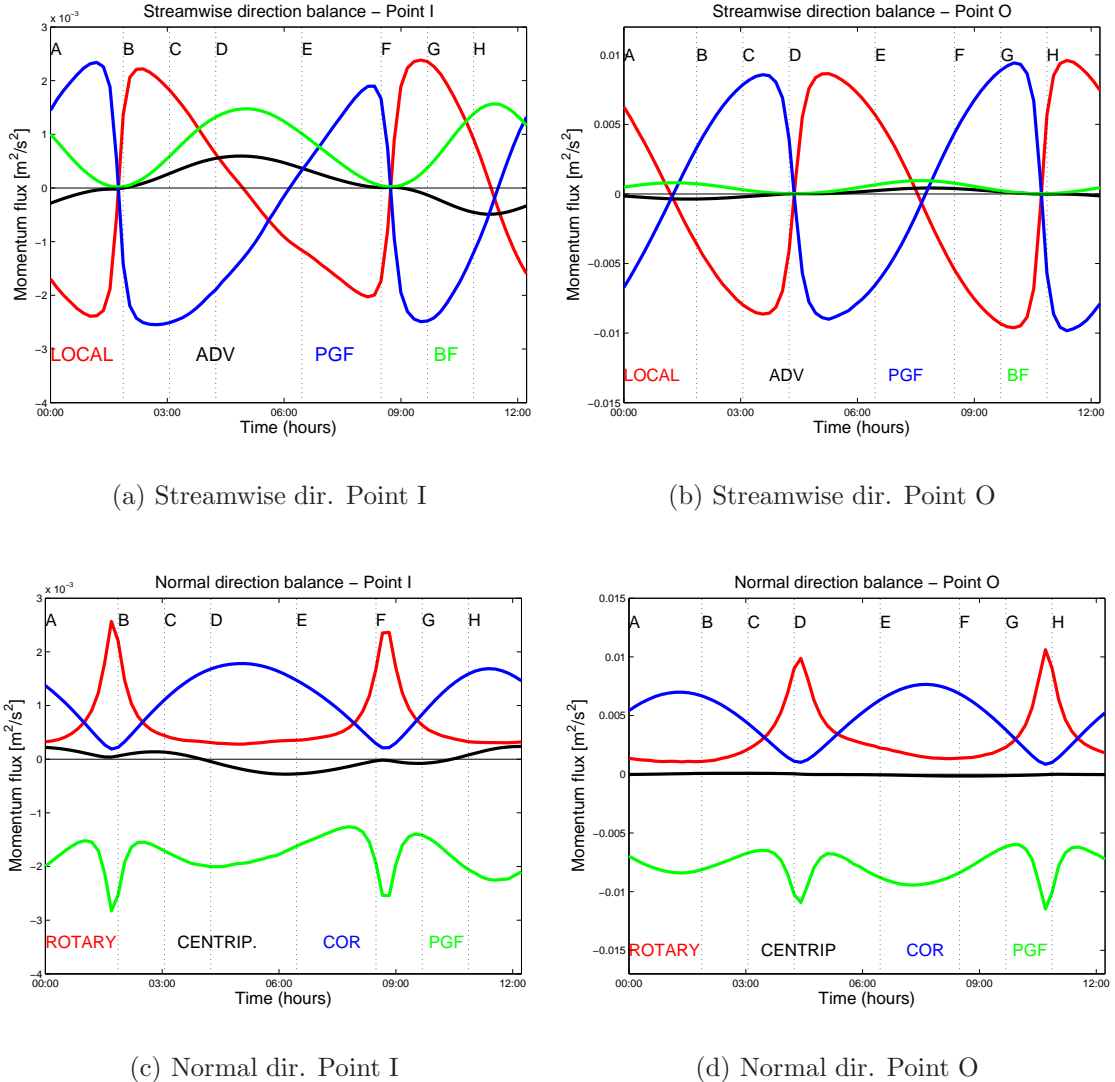


Figure 4.1: Time series of momentum flux at nodes I and O. The streamwise direction terms are: local (red), advective (black), pressure gradient (blue) and bottom friction (green); the normal direction terms are: rotary (red), centripetal acceleration (black), Coriolis (blue) and pressure gradient (green). (See Eqs. (4.3) and (4.4) for more details.)

flow, while the offshore flow is still accelerating. The rotary acceleration map (Fig. 4.2h), which indicates how the flow direction evolves over time, shows a strong positive (ACW) temporal change in the flow direction inshore. Streamwise advective acceleration (Fig. 4.2e) is insignificant, while the streamwise bottom

friction (Fig. 4.2g) is large and positive in the shallower regions. The streamwise pressure gradient (Fig. 4.2f) is large and negative (i.e., favorable) offshore and weak and positive (i.e., adverse) onshore. Therefore, the primary onshore balance in the streamwise direction is between pressure gradient, bottom friction and local acceleration, while the primary offshore balance is between pressure gradient and local acceleration. The contrasts (change of sign in the onshore/offshore direction) in the local acceleration and pressure gradient terms suggest that these regions are under distinctly different dynamical conditions. In the onshore region off Chatham, MA, the combined effects of streamwise adverse pressure gradient and bottom friction are responsible for decelerating the flow as time advances, resulting in flow separation (eddy motion generation).

In the direction normal to the flow, the primary balance is between Coriolis force (Fig. 4.2k) and pressure gradient (Fig. 4.2j), and thus the dynamical balance is close to geostrophy. From Figure 4.2b, one can estimate a northeastward geostrophic velocity of approximately 0.4 m/s, which is very close to the model-computed velocity. The fact that the centripetal acceleration (Fig. 4.2i) is very small suggests that the radius of flow curvature ( $R_s$ ) is very large compared to the streamwise velocity squared.

### 4.3.2 Second half flood (B)

As flood advances toward slack the main offshore streamwise balance is still between local acceleration (Fig. 4.3d) and pressure gradient (Fig. 4.3f), as during maximum flood, with bottom friction being important in the Great South channel region and in part of the offshore region (Fig. 4.3g). Off Chatham there is a marked localized area of positive local acceleration (Fig. 4.3d) and negative pressure gradient

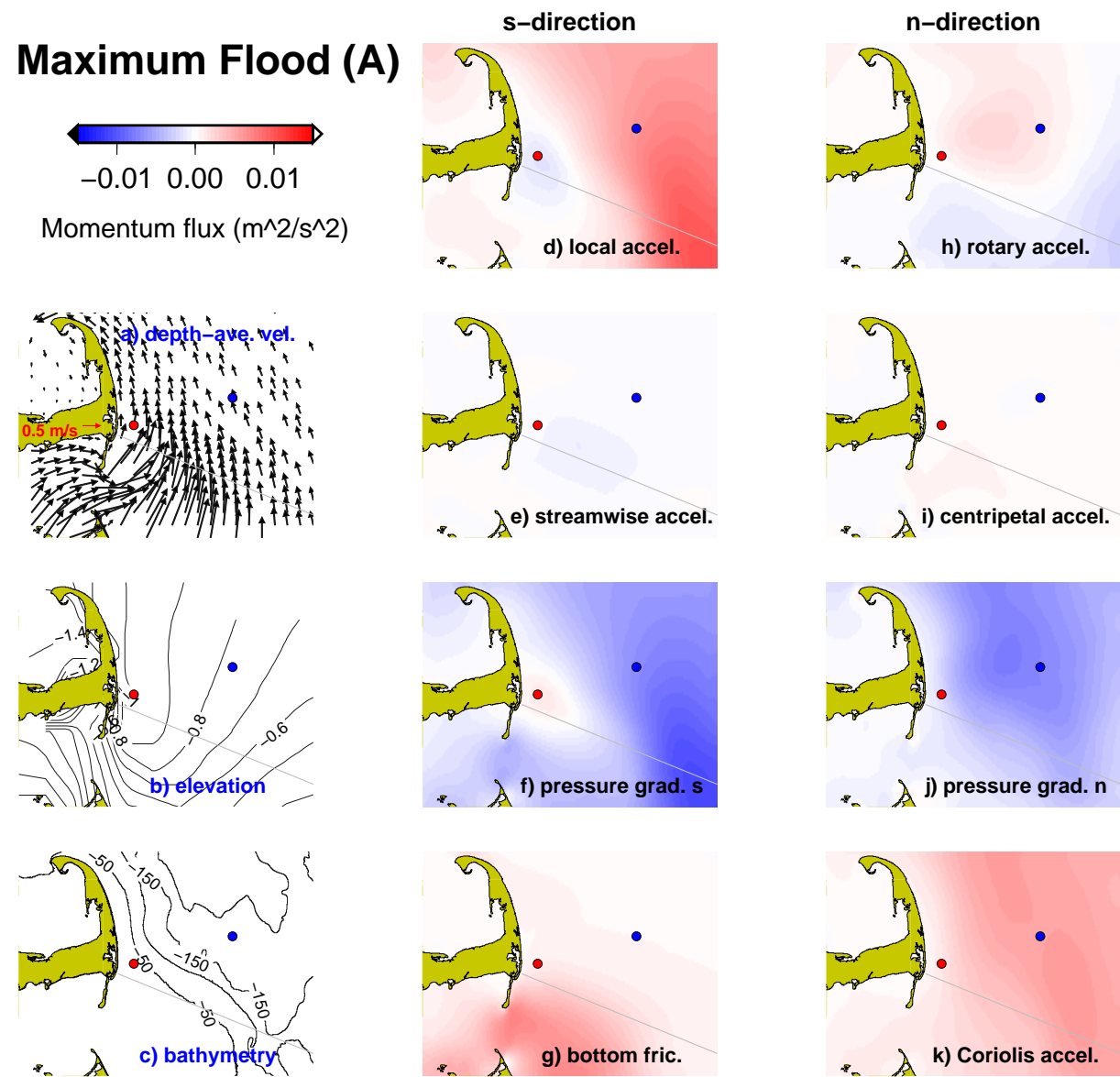


Figure 4.2: Circulation and momentum balance at maximum flood (time A) in terms of: (a) depth-averaged velocity, (b) free-surface elevation with 0.1-meter contour intervals, (c) bathymetry with 50-meter contour intervals, and (d) to (k) distribution of individual momentum flux terms (see legend above left and Eqs. (4.3) and (4.4) for term definitions). Points I and O and the transect of reference are plotted in red, blue and gray, respectively.

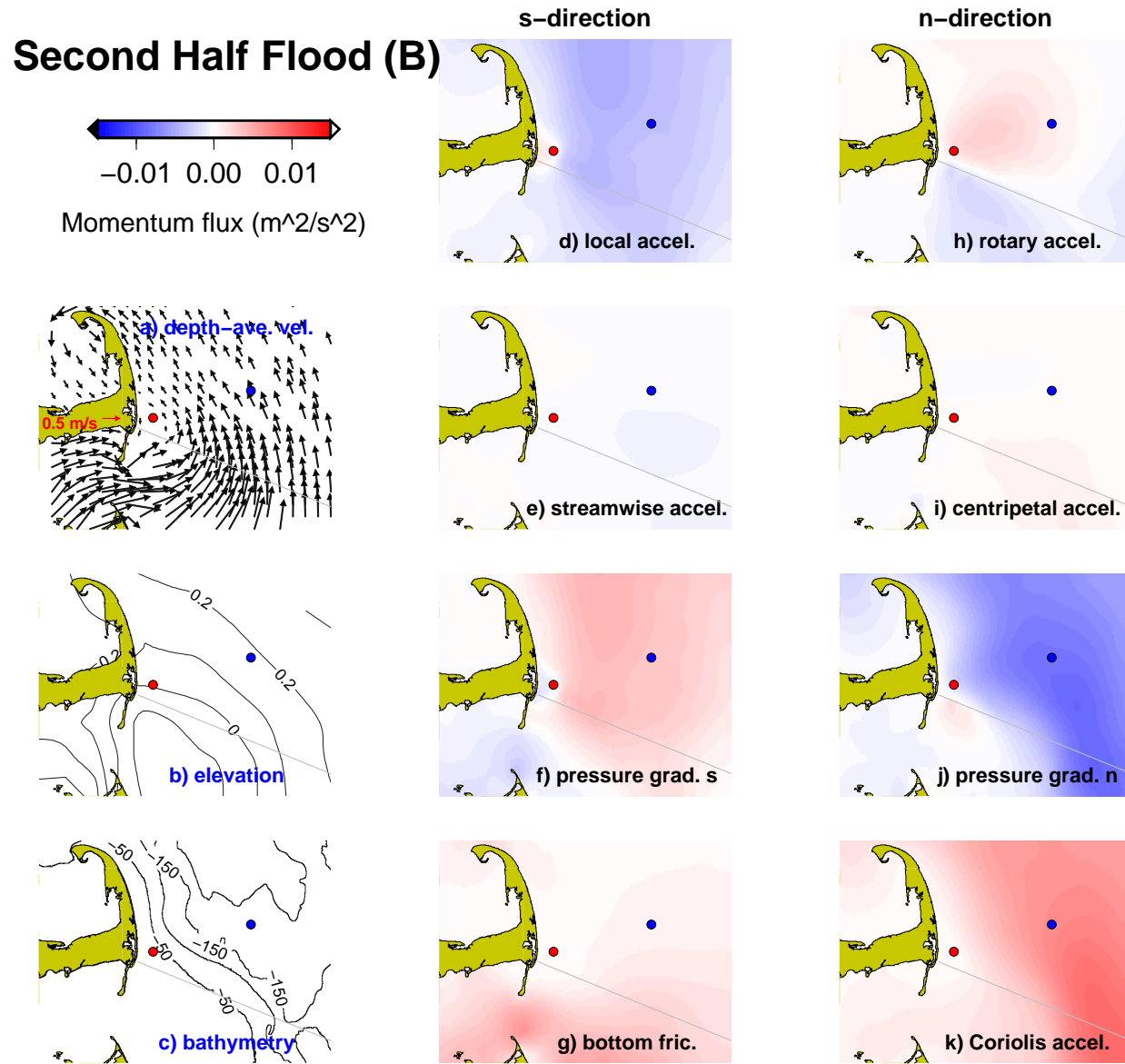
(Fig. 4.3f), features associated with flow separation (Fig. 4.3a). Offshore the direction of the isopleths of elevation has changed from E-W (at maximum flood) to SW-NE (Fig. 4.3b), and the flow is subject to a positive (i.e., adverse) pressure gradient (Fig. 4.3f). In the normal direction the primary offshore balance remains the same, between Coriolis force (Figure 4.3k) and pressure gradient (Fig. 4.3j). However, the balance just off Chatham has changed slightly, with rotary acceleration (Fig. 4.3h) being balanced by pressure gradient (Fig. 4.3j) as a result of flow separation in that region (Fig. 4.3a). The centripetal acceleration has a small contribution in the southeastern region, where the flow has high velocities and a small radius of curvature (Fig. 4.3i).

### 4.3.3 Slack before ebb (C)

At the start of ebb the streamwise dominant terms have increased significantly in magnitude from second-half flood, and they also show different spatial patterns. The main streamwise balance remains between local acceleration (Fig. 4.4d) and pressure gradient (Fig. 4.4f), but now the onshore localized area of positive local acceleration (Fig. 4.4d) and negative pressure gradient (Fig. 4.4f) has grown. The onshore contribution of bottom friction has decreased, since the the flow has just started to ebb. This balance is consistent with the depth-averaged velocity distribution (Fig. 4.4a), where the pressure gradient is negative (i.e., favorable) and the local acceleration is positive (i.e., accelerating). In the offshore region the flow is reaching the end of flood with these two terms being unfavorable (positive pressure gradient and decelerating local acceleration).

In the normal direction the main balance has changed from the previous situation. The rotary acceleration term (Fig. 4.4h) has increased significantly in magnitude as

Figure 4.3: As in figure 4.2, but for second half flood (time B).

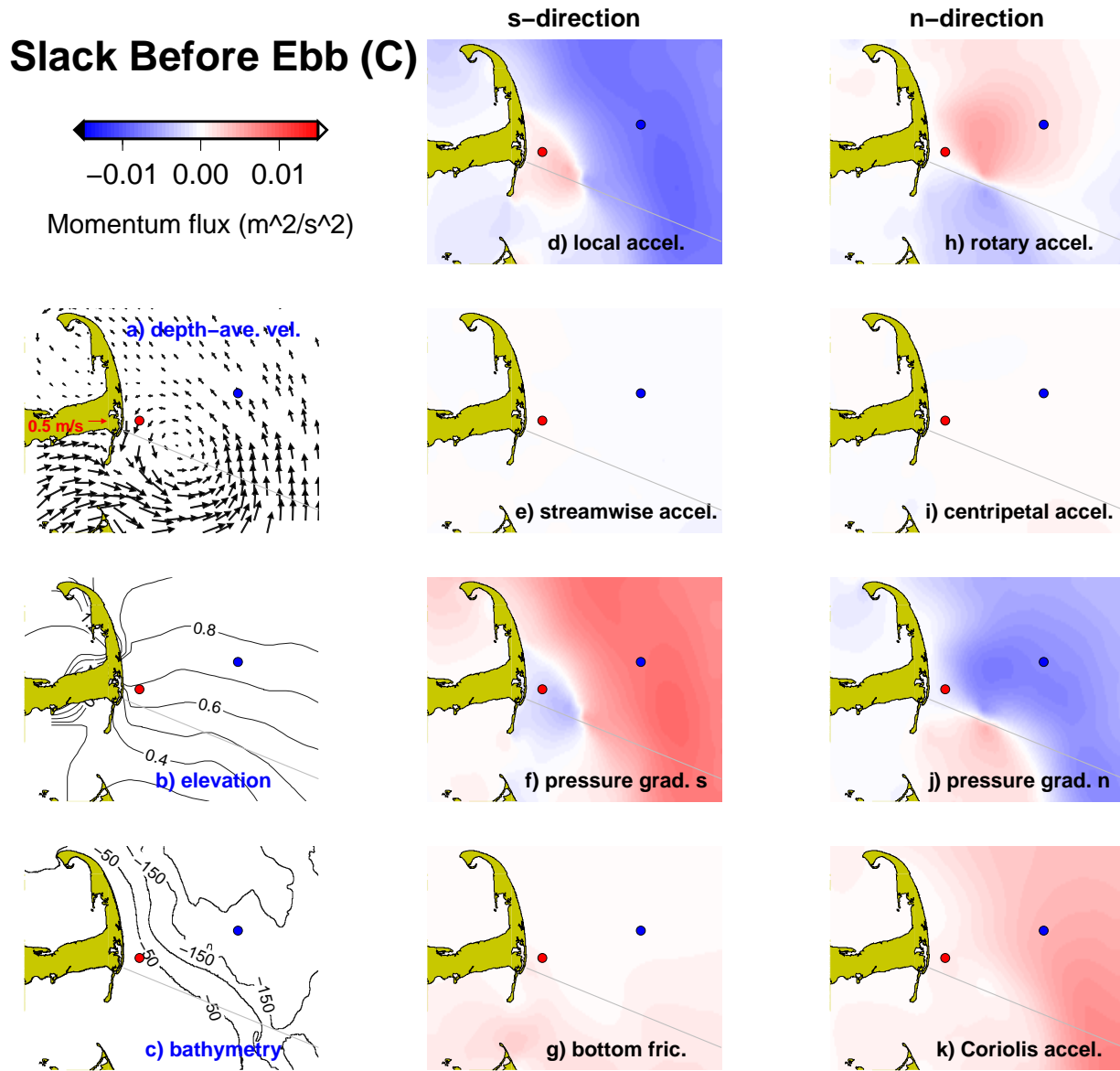


a result of the eddy motion growth. Three dynamical states are present: a) onshore, there is a balance between rotary acceleration (Fig. 4.4h) and pressure gradient (Fig. 4.4j); b) offshore, the balance is between pressure gradient and Coriolis (or a geostrophic balance); and c) between these two regions, all three terms are important. In the northern region the positive value of rotary acceleration indicates that the flow is changing cyclonically ( $\alpha_{t=2} > \alpha_{t=1}$ ), while in the southern region the negative value indicates the flow is changing anti-cyclonically (towards ebb). The Coriolis force (Fig. 4.4k) has weaken, specially onshore, as a result of the small velocities during slack time. Altought an ACW eddy motion is present, the centripetal acceleration does not contribute to the momentum flux balance (Fig. 4.4i). This is mainly due to the weak velocities associated with this eddy motion. .

#### 4.3.4 First half ebb (D)

When the flow accelerates towards maximum ebb the streamwise balance remains between local acceleration (Fig. 4.5d) and pressure gradient (Fig. 4.5f), but now the contribution of bottom friction is restricted to the southward shallower region (Fig. 4.5g). The positive local acceleration (Fig. 4.5e) and negative pressure gradient (Fig. 4.5f) have grown even more and now dominate the entire region. The offshore balance between the negative local acceleration and the positive pressure gradient is consistent with the weak velocities in that region. The primary normal direction momentum balance also remains between pressure gradient (Fig. 4.5j), rotary acceleration (Fig. 4.5h) and a less important Coriolis force (Fig. 4.5k). The rotary acceleration is largest and positive in the deeper region since flow is still turning southward (cyclonically), where the normal direction pressure gradient is

Figure 4.4: As in figure 4.2, but for slack before ebb (time C).



driving this change.

## 4.4 Summary of Results

The model results presented in Chapters 3 and 4 define the formation and evolution of transient tidal eddy motion in the western Gulf of Maine region. Snapshots of depth-averaged velocity and relative vorticity show that the eddy motion accompanies the change of tides in the Great South Channel (GSC), with flow separation occurring about 0.6 hours later during the ebb cycle than during the flood cycle. These results also reveal that the center of eddy motion tends to follow the 50-meter isobath during approximately half of the flood/ebb  $M_2$  cycle. Time series of model elevation, velocity, relative vorticity and momentum flux terms indicate two distinct kinematical/dynamical regions: one nearshore and the other offshore.

The nearshore variability is more asymmetric (non-sinusoidal) than the offshore, apparently due to the relatively greater importance of the nonlinear terms, especially bottom friction. The nearshore kinematic characteristics are close to those of a progressive wave. The nearshore streamwise dynamical balance is generally between local acceleration (LA) and pressure gradient force (PGF), with significant contributions from bottom friction (BF) during times of strong currents. The nearshore normal direction dynamical balance is mainly between Coriolis force and PGF, with the balance shifting briefly to rotary acceleration and PGF during change of tides (and/or in the presence of eddy motion).

The offshore time series variability is mode sinusoidal, indicating that the flow dynamics are much more linear. The kinematic characteristics in the offshore region

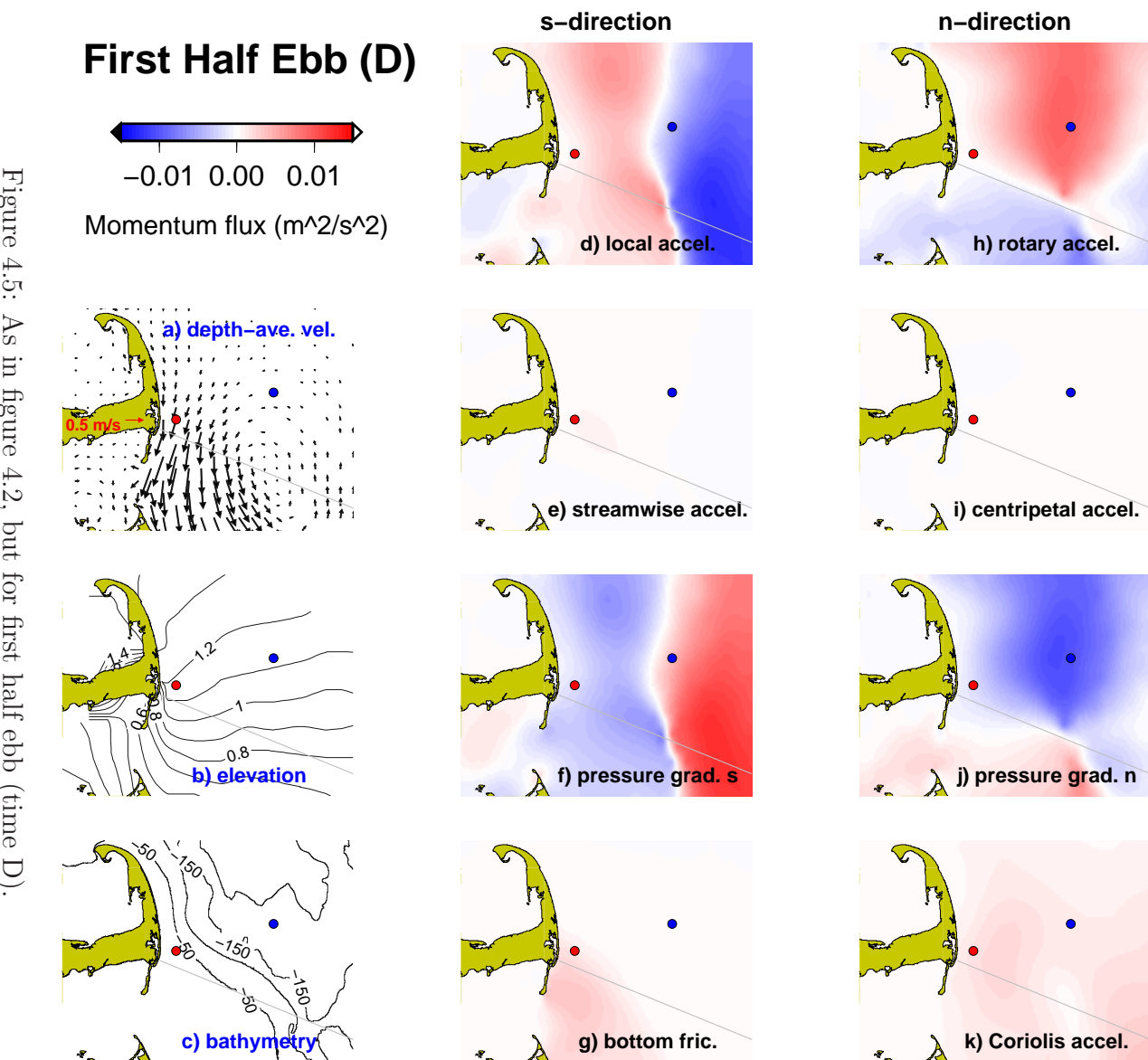


Figure 4.5: As in figure 4.2, but for first half ebb (time D).

are close to those of a standing wave. The offshore region streamwise dynamical balance is dominated by an LA and PGF balance (with negligible friction contributions). The offshore normal dynamical balance is the same as that in the nearshore region.

He and Wilkin (2006), who studied  $M_2$  tides in our study region using a numerical model (ROMS), found results consistent with those presented here. Their momentum balance time series at a location close to point I (see Fig. 3.5) indicate a principal dynamical balance in the u-direction (east-west/approximately across-isobath) momentum between Coriolis and pressure gradient, while the principal balance in the v-direction (north-south/approximately along-isobath) momentum was between pressure gradient and local acceleration. The nearshore presence of a streamwise adverse PGF and the strong influence of BF during maximum flood (ebb) results in the formation, due to flow separation, of an anticlockwise (clockwise) eddy motion that translates along the boundary between the two dynamical regions.

# Chapter 5

## Three-Dimensional Circulation

### 5.1 Velocity Structure

In the following subsections we examine the three-dimensional velocity structure during maximum flood and maximum ebb (letters A and E, respectively, in Fig. 3.4), and in the presence of anticlockwise and clockwise eddy motions. These results were generated under spring tide conditions (highlighted in yellow in Fig. 3.4) after analysis during neap tide conditions revealed similar results.

#### 5.1.1 Maximum flood (A)

Figure 5.1 shows the three-dimensional flow structure at maximum flood (time index A in Fig. 3.4). Figure 5.1a shows the evidence of an anticlockwise flow, with sea surface elevation field indicating an onshore-directed pressure gradient force along the transect of reference (red line in Fig. 5.1a). Close to the coast the normal velocity is directed onshore near the bottom and offshore near the surface (Fig. 5.1b). However, the normal velocity in the offshore region (waters deeper than 60 meters) is directed offshore near the bottom and onshore near the surface. The vertical velocity along the transect shows the occurrence of downwelling near the

bathymetry break (Fig. 5.1c), where the normal velocity converges near the surface and diverges near the bottom. The maximum strength in the vertical velocity (up to -1.5 mm/s) occurs close to the bottom in the depth range of 30 to 50 meters. To better understand the three-dimensional structure, snapshots of the depth-averaged velocity divergence are presented in Figure 5.2. These fields provide a qualitative idea of the locations of the principal velocity divergences, consistent within the 21 model layers. During maximum flood (time A) the visual convergence of the depth-averaged velocity (Fig. 5.2a) in the region of the reference transect seems to be consistent with the occurrence of downwelling near the coast (Fig. 5.1c). Therefore, (a) close to the coast downwelling seems to be controlled by the main flow and not by the normal velocity, (b) while at the bathymetry break it seems to be controlled by both main flow and normal velocity. The streamwise flow along the transect shows both a modest amount of vertical shear in the shallow, nearshore region, and a significant transverse variation (Fig. 5.1d).

### 5.1.2 Slack before ebb (C)

At slack before ebb (time C in Fig. 3.4) an anticlockwise eddy motion (that developed near the coast at time B) is evident in the depth-averaged velocity results (Fig. 5.3a). The sea surface elevation field (Fig. 5.3a) indicates a predominantly southward pressure gradient force. The nearshore normal velocity pattern observed during maximum flood (Fig. 5.1b) has moved offshore (Fig. 5.3b). Interestingly, the normal velocity in both shallower and deeper regions is directed onshore near the bottom and offshore near the surface (Fig. 5.3b), connected by a wide band of upwelling near the coast (Fig. 5.3c). As shown in Figure 5.2b, this coastal upwelling is also supported by the positive values of the depth-averaged velocity divergence.

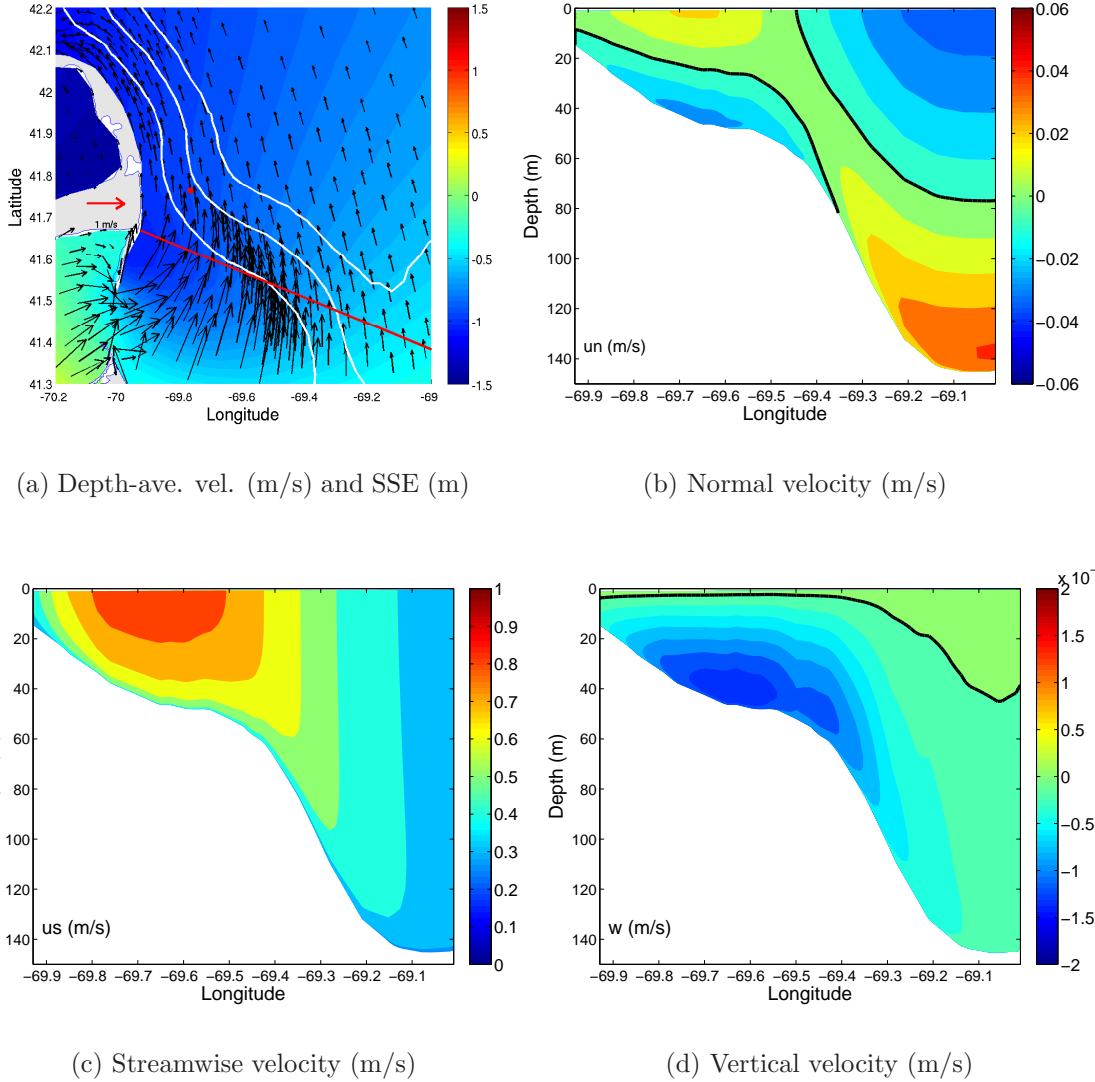


Figure 5.1: Model result at maximum flood (time A) in terms of a) depth-averaged velocity (m/s) and sea-surface elevation (SSE, m). (The red line and red dot on a) are the section location and the node of reference for the tidal phase, respectively; the 50-, 100- and 150-meter isobaths are also shown.); b) normal or secondary velocity (m/s), where for visualization purposes corrections were made so that positive value means away from the coast; c) streamwise velocity (m/s); and d) vertical velocity (m/s). The black lines in b) and c) indicate the zero countour value.

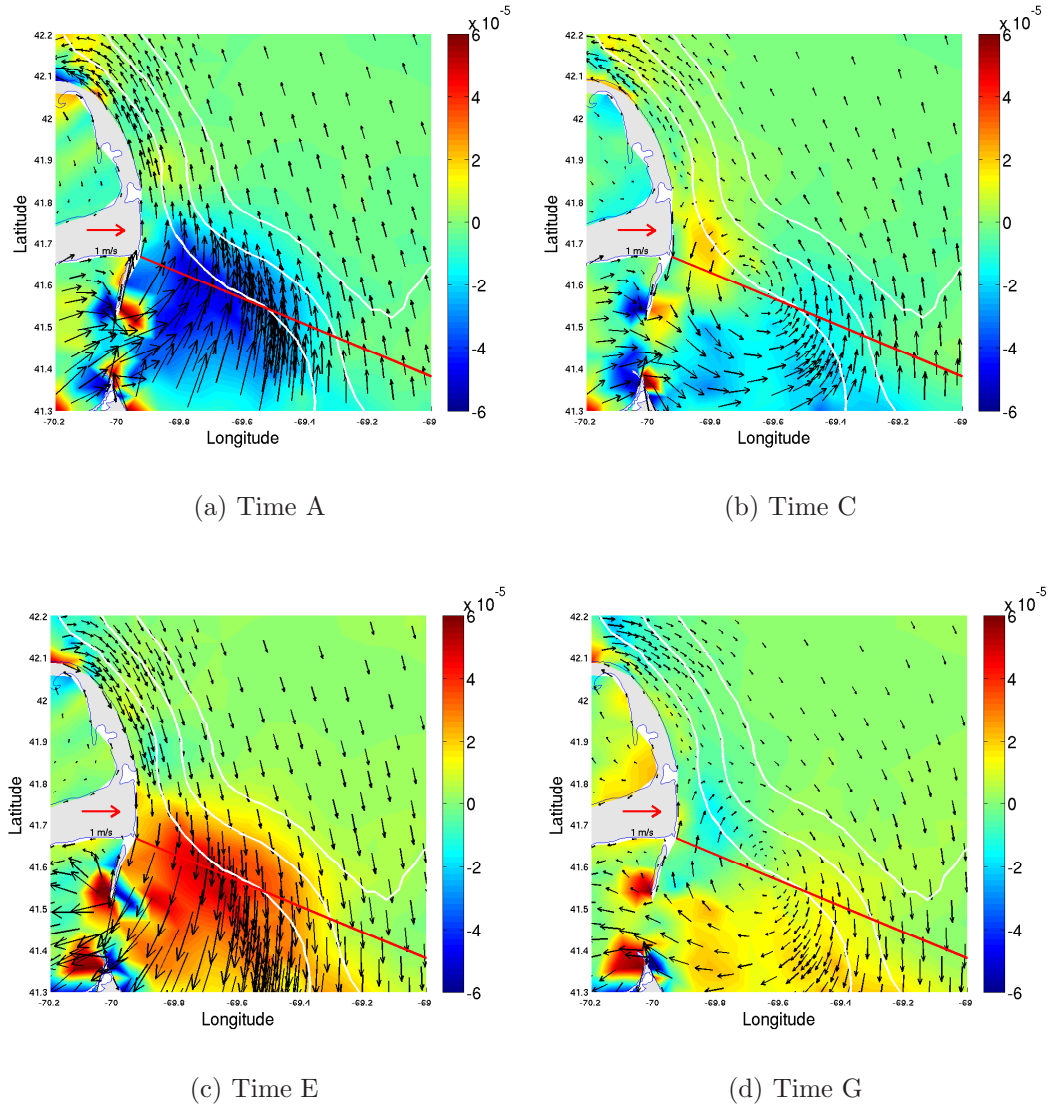


Figure 5.2: Depth-averaged velocity (m/s) and its divergence (color coded, 1/s) during (a) maximum flood, time A; (b) slack before ebb, time C; (c) maximum ebb, time E; and (d) slack before flood, time G. The red line marks the section location. The 50-, 100- and 150-meter isobaths are shown in white.

The maximum strength in the normal velocity section occurs at the bathymetry slope region, where the near-bottom and near-surface velocity magnitudes are close to 4 cm/s. Although the normal flow is toward the same direction in both these regions, the flow converges at the deeper region (Fig. 5.2b), resulting in downwelling (Fig. 5.3c). The strength of both near-coast upwelling and offshore downwelling (both  $\sim 0.5$  mm/s) are one order of magnitude smaller than the strength of the vertical flow during maximum flood. The streamwise flow along the transect shows strong horizontal variation due to the presence of the eddy motion, where higher velocities occur away from the eddy motion center (Fig. 5.3d). Streamwise vertical shear is still evident, but it is less pronounced than during maximum flood.

### 5.1.3 Maximum ebb (E)

The three-dimensional flow structure at maximum ebb (time E in Fig. 3.4) is shown in Figure 5.4. At this tidal phase the flow shows evidence of a clockwise circulation with a sea surface elevation field that indicates an offshore-directed pressure gradient force along the transect of reference (Fig. 5.4a). Close to the coast, the normal velocity is directed offshore near the bottom and onshore near the surface (Fig. 5.4b). Like during maximum flood, the situation is reversed in the offshore regions, where the normal velocity is directed onshore near the bottom and offshore near the surface (Fig. 5.4b). The normal velocity is weak in the shallower region, and reaches its maximum strength in deeper waters. The bathymetry break region divides these two different regions, with flow converging at the bottom and diverging at the surface, resulting in upwelling (Fig. 5.4c). The maximum strength in the vertical velocity (up to 1.5 mm/s) occurs close to the bottom in the depth range of 30 to 60 meters. As shown in Figure 5.2c, the positive values of the

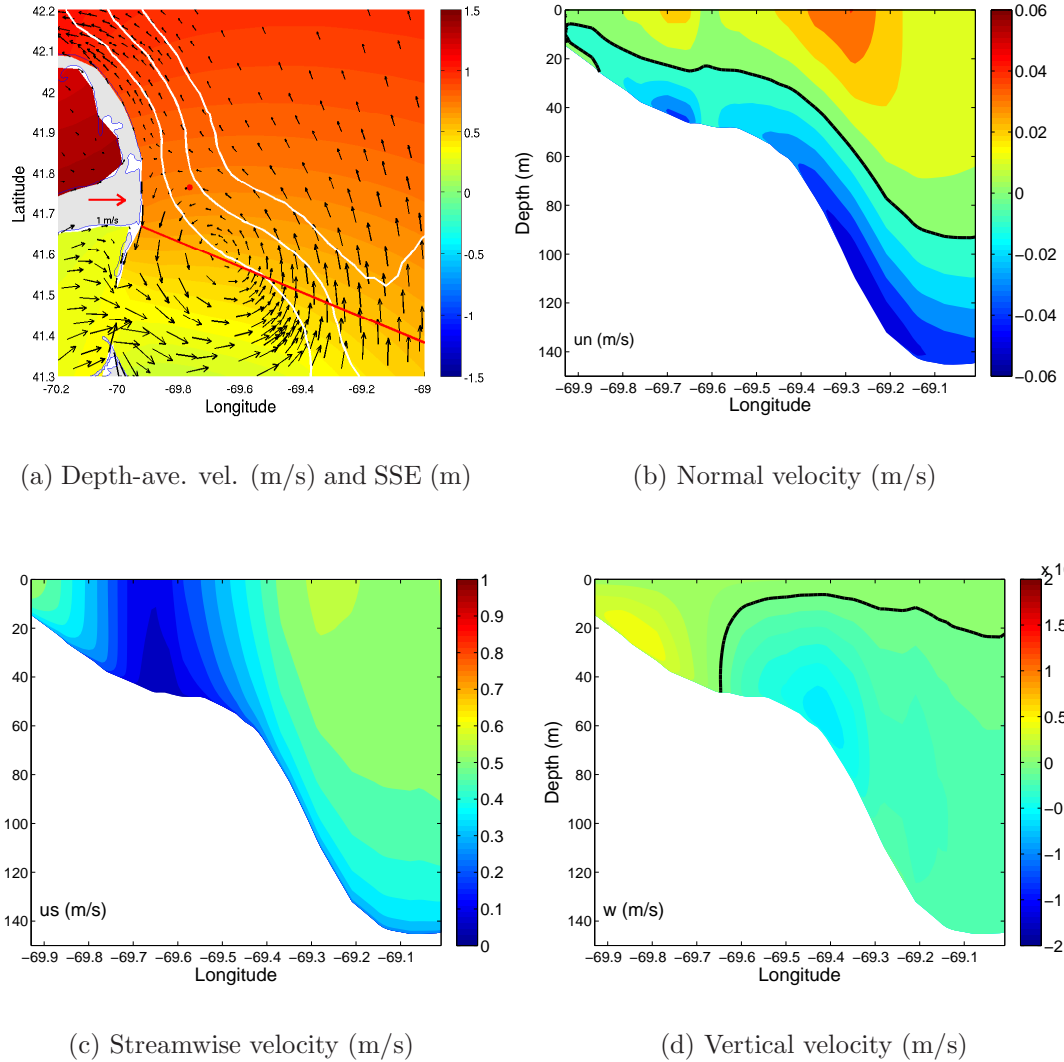


Figure 5.3: As in figure 5.1, but for slack before ebb (time C), when an anticlockwise eddy motion is present.

depth-averaged velocity divergence along the reference transect suggest that the coastal upwelling is controlled by the main flow. Again, the streamwise flow along the transect shows a modest amount of vertical shear in the shallow region and a strong horizontal variation (Fig. 5.4d). However, this horizontal variation is weaker than that observed during maximum flood.

#### 5.1.4 First half flood (G)

In the presence of a clockwise eddy motion (time G in Fig. 3.4), the sea surface elevation results (Fig. 5.5a) indicate a predominantly northward pressure gradient force. The nearshore normal velocity pattern observed during maximum ebb (Fig. 5.4b) has moved offshore. The normal velocity in both shallower and deeper regions is directed offshore near the bottom and onshore near the surface (Fig. 5.5b). The maximum strength of the secondary flow occurs in the offshore region, where both the near-bottom and near-surface velocities are up to 4 cm/s. The vertical velocity section shows downwelling near the coast and upwelling in the offshore region (Fig. 5.5d), consistent with the normal velocity (Fig. 5.5b) and depth-averaged divergence (Fig. 5.2d) results, respectively. Again, the strength of both near-coast downwelling and offshore upwelling ( $\sim 0.4$  mm/s) are small compared to the strength of the vertical velocities during maximum ebb. Like during the presence of an ACW eddy motion, the streamwise flow shows strong horizontal variation, with higher velocities occurring away from the eddy motion center, and a weak vertical shear compared to the scenario during maximum ebb (Fig. 5.5d).

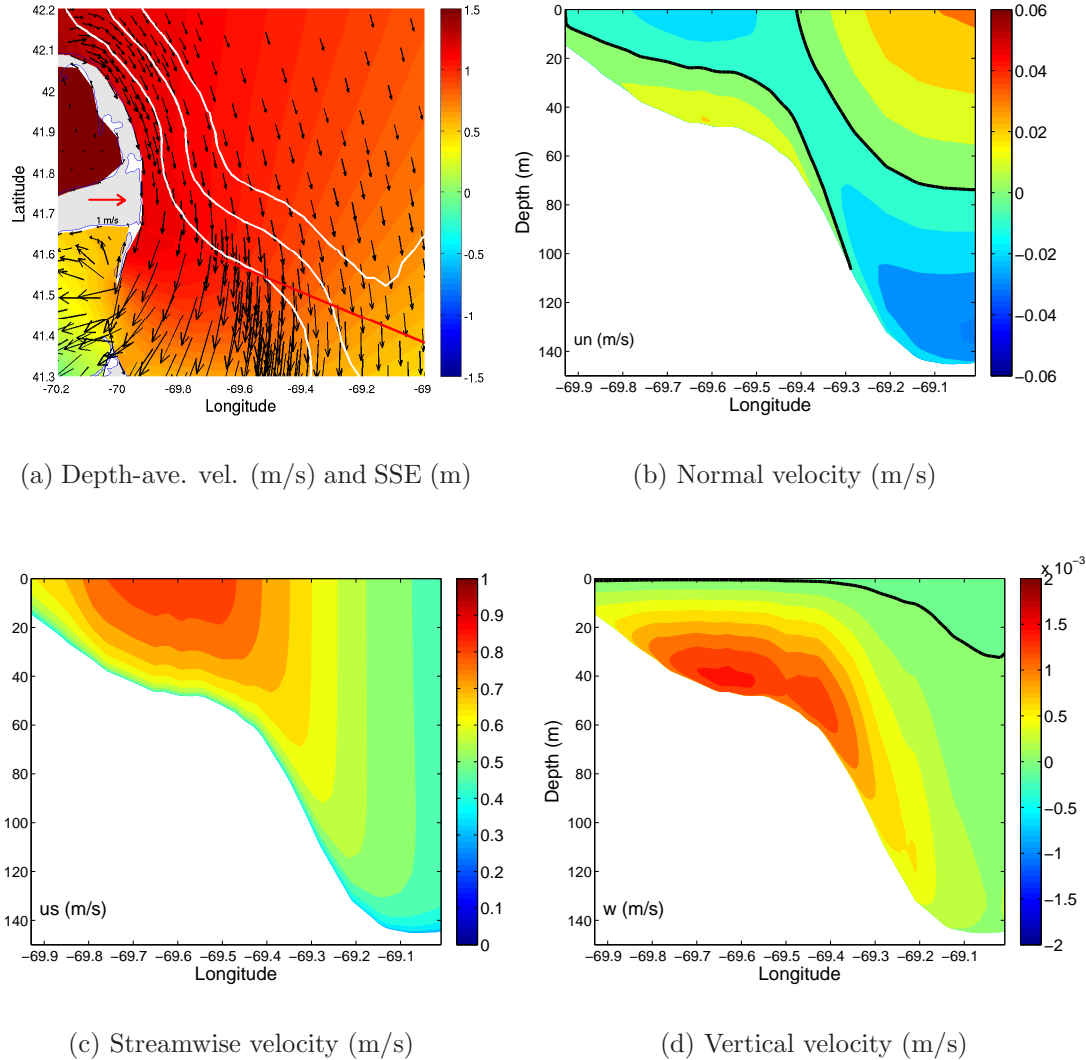


Figure 5.4: As in figure 5.1, but for maximum ebb (time E).

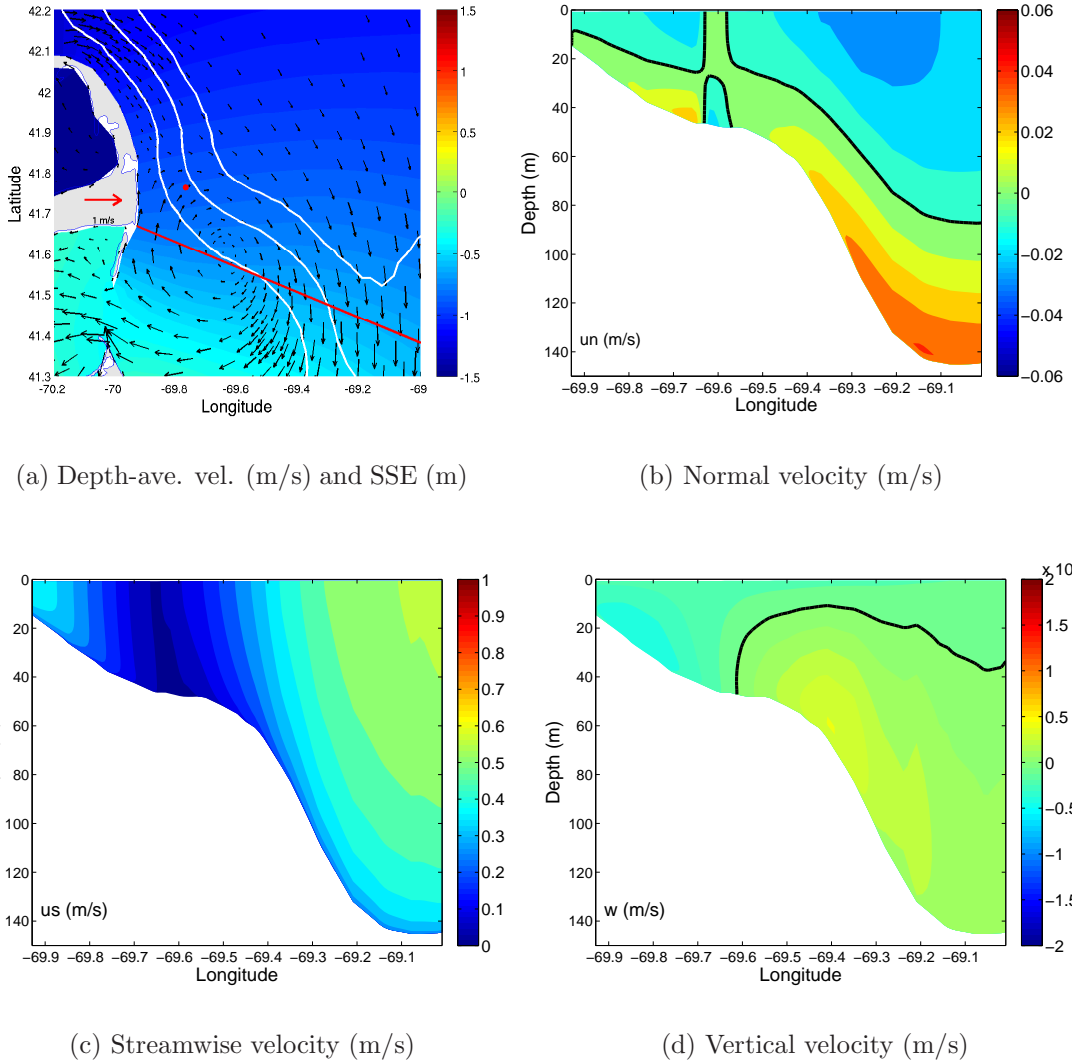


Figure 5.5: As in figure 5.1, but for slack before flood (time G), when a clockwise eddy motion is present.

## 5.2 Three-Dimensional Residual Circulation

In this section, three-dimensional circulation results averaged over 31 days (residual) are presented in order to define the long-term residual tidal flow transport pattern along the two transects depicted in Figure 5.6. Transect 1 is located off the “elbow” of Cape Cod, where the eddy motion forms and translates. Transect 2 is located off the northern reach of Cape Cod, where the isobaths tend to be parallel to the coastline.

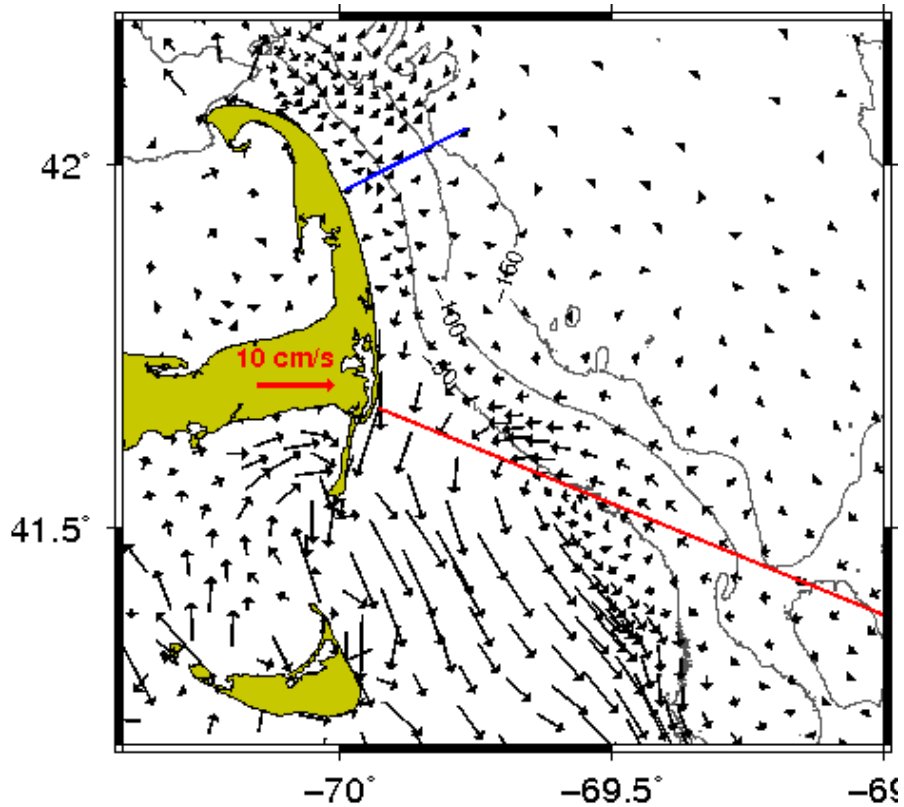


Figure 5.6: Residual depth-averaged circulation. Transects 1 (red) and 2 (blue) are located.

Figure 5.6 shows a snapshot of the depth-averaged residual circulation. An ACW circulation is evident in the transect 1 region . At the nearshore end of transect 1, the depth-averaged residual velocities are approximately southward (ranging from

7-10 cm/s) and consistent with both the TTE moored-ADCP residual currents (see Chapter 2) and the residual currents measured by Chen et al. (1995) during late spring. This reinforces the idea (Lynch and Naimie 1992; Chen et al. 1995) that the residual currents over the shallower sides of the GSC are mainly due to tidal rectification.

The residual secondary flow distribution along transect 1 is shown in Figure 5.7a. For depths greater than 40 meters, the results show a residual flow directed offshore in the upper layer and toward the coast in the lower layer. The opposite occurs for waters shallower than 40 meters. The strongest residual secondary flow in both upper and lower layers takes place at the bathymetry break region (between 60 and 130 meters). Figure 5.7b shows the residual vertical velocity along transect 1. Two upwelling zones are seen in the layers close to the bottom. The nearcoast residual upwelling values are as large as 6.0 m/day, while the offshore values over the slope are about 4.3 m/day. Weak residual downwelling is seen in the extreme eastern region of transect 1. The residual secondary flow along transect 2 is also directed offshore in the upper layer and toward the coast in the lower layer (Fig. 5.7c). The residual vertical flow along transect 2 indicates downwelling over a large area. The intensity of the vertical residual velocities in transect 2 are one order of magnitude smaller than the ones in transect 1.

### 5.3 Summary of Results

Figure 5.8 presents a set of cartoons that summarize the circulation along transect 1 from time A to time G. During maximum flood (time A) the nearshore (offshore) secondary circulation is directed seaward (onshore) near the surface and onshore

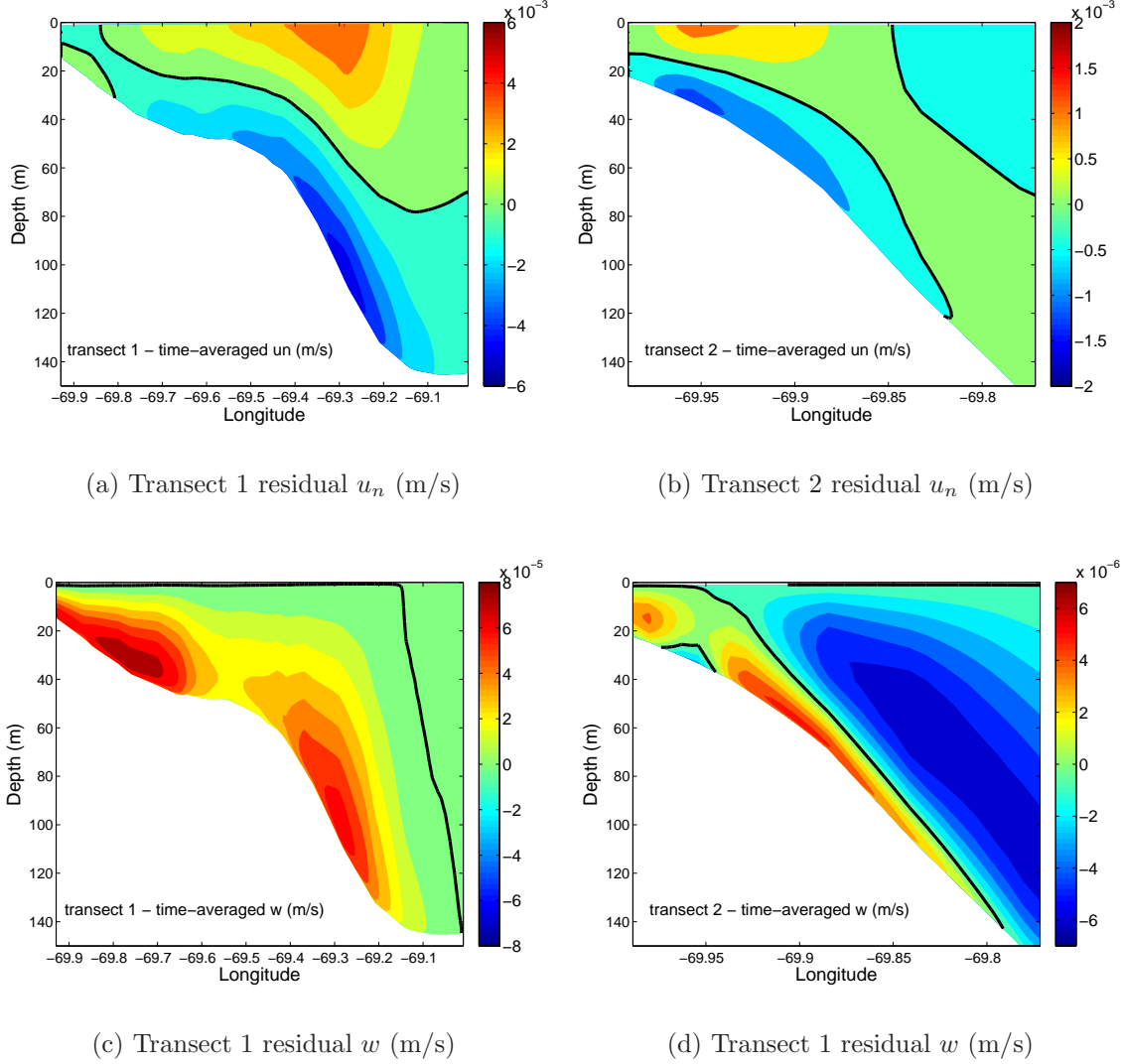


Figure 5.7: The 31-day time-averaged (residual) model results in streamwise/normal coordinates for: a) residual normal velocity,  $u_n$  (m/s), along transect 1, where for visualization purposes corrections were made so that positive value means away from the coast; b) as a) for transect 2; c) residual vertical velocity,  $w$  (m/s), along transect 1; and d) as b) for transect 2. The zero contour lines are shown in black for clarity.

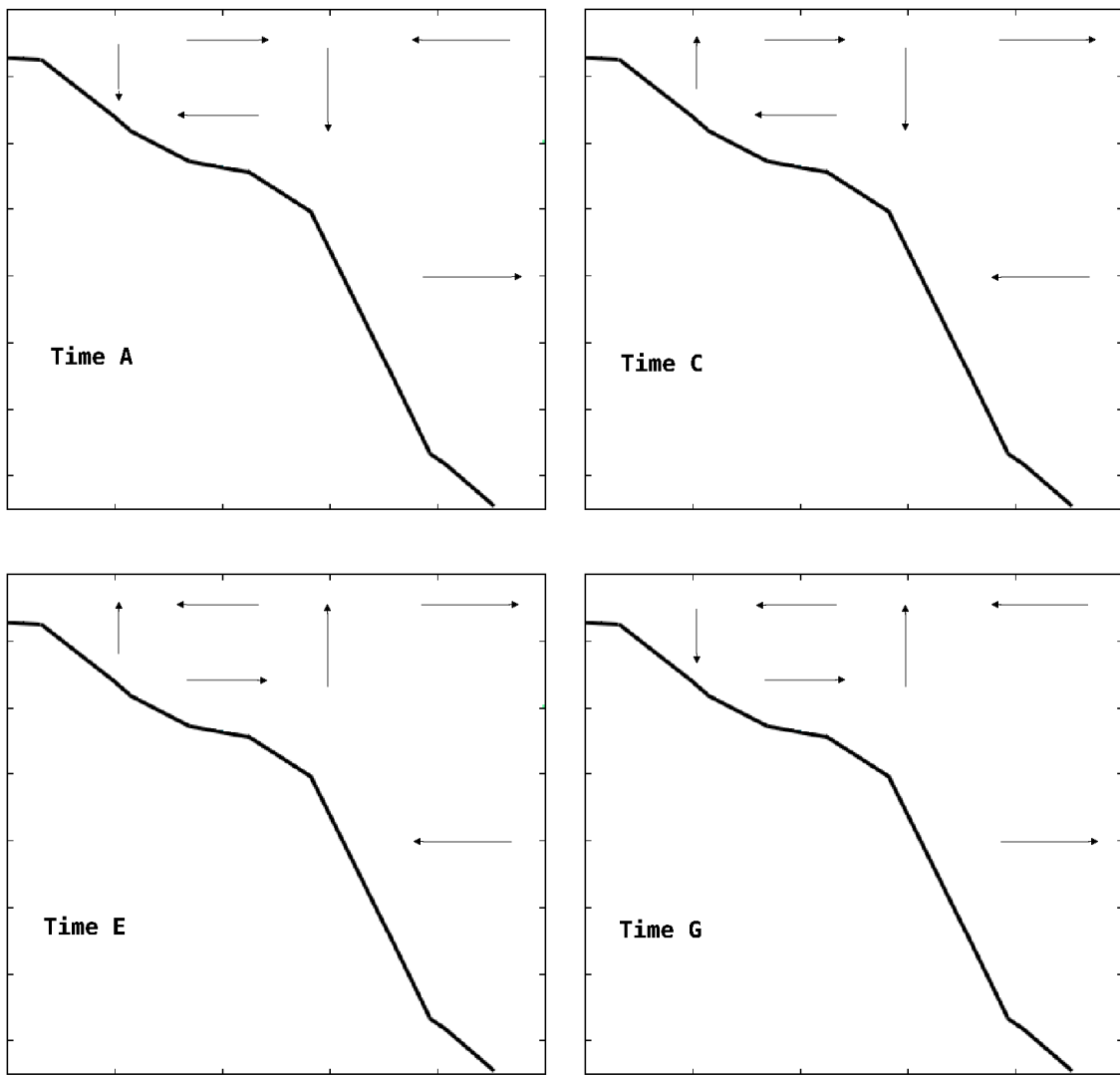


Figure 5.8: Schematic of the tidal circulation along transect 1 from time A to time G.

(seaward) near the bottom, with downwelling occurring close to the coast and at the bathymetric slope. In the presence of an ACW eddy motion (time C), the nearshore pattern observed during maximum flood (time A) has moved offshore. The entire secondary circulation along transect 1 is directed offshore near the surface and onshore near the bottom, with upwelling occurring close to the coast and downwelling occurring at the bathymetric slope. During maximum ebb (time E)

and in the presence of a CW eddy motion (time G), the situations are the opposite of those observed during maximum flood (time A) and in the presence of an ACW eddy motion (time C), respectively.

The depth-averaged residual flow indicates an ACW circulation in a region influenced by the eddy motions (Fig.5.6). As shown schematically in Figure 5.9, the residual secondary circulation along transects 1 and 2 are mostly directed offshore in the upper layers and onshore in the lower layers, except in a shallow (deep) region of transect 1 (2) where the opposite occurs. The residual vertical circulation results show the occurrence of upwelling along transect 1 and downwelling along most of transect 2 (except near the coast).

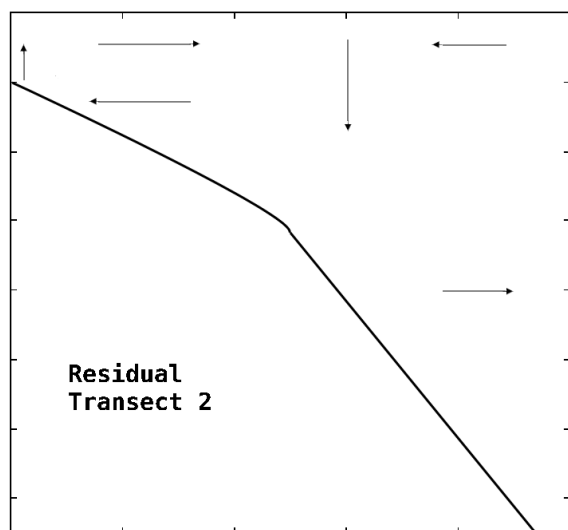
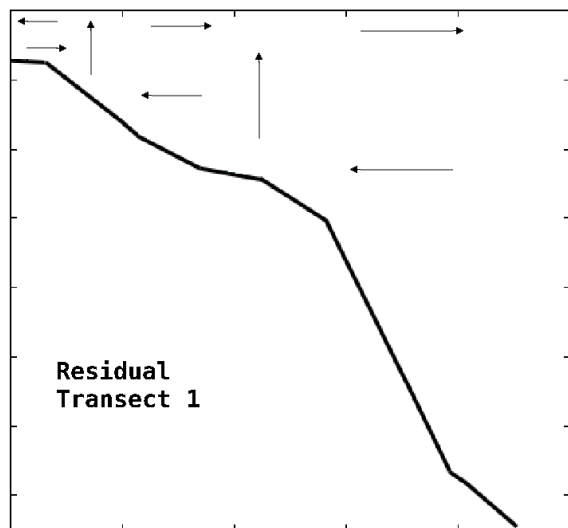


Figure 5.9: Schematic of the residual tidal circulation along transects 1 and 2.

# Chapter 6

## Discussion

### 6.1 Eddy Motion Formation and Evolution

The characteristics of the phase eddy process proposed by Black and Gay (1987) appear to be relevant to the results presented here. Black and Gay (1987) concluded that the formation of phase eddies was due to the strong bottom friction gradient, with low bottom frictional resistance in the deep free stream and high bottom friction resistance in the shallower water of a promontory or subtidal barrier. Both characteristics are present in the study presented here. The Black and Gay (1987) phase eddy was initiated by an oscillatory PGF in a nearshore zone of relatively high friction. Their numerical model results for the Rattray Island study showed that with the onset of the adverse pressure gradient force the shallower nearshore flow slowed rapidly, while the offshore flow could take up to 3 hours to decelerate. Under such conditions, large phase differences develop between the currents in the offshore and nearshore regions.

Our model-derived time series (Fig. 3.8) from the offshore location (point O) show that the flow decelerates approximately 2.4 hours after the onset of the adverse pressure gradient. The flows at the nearshore (point I) and offshore locations show a

phase difference of approximately 3 hours. Like the Black and Gay (1987) study, the strength of the eddy motion studied here was governed by the strength of the inshore (I) versus offshore (O) bottom friction difference.

Some important differences between the tidal eddy motion investigated here and that reported in the literature (Geyer and Signell 1990; Lee et al. 1999; MacCready and Pawlak 2001; Neill et al. 2007; White and Wolanski 2008) should be noted.

First, in the present case, both CW and ACW eddy motions were always formed in the same nearshore location and then translated along the same path. Second, because our eddy motion patterns traveled so rapidly across the GSC, it is not possible to observe them using surface drifters (Brown et al. 2009). Observing these eddy motions using conventional shipboard ADCP techniques would not be effective, since the eddy motion phase speed is approximately 5 m/s, while ADCP transects are conducted at approximately 0.3 m/s. However, because the flow is tidally driven, it would perhaps be possible to observe such eddies by applying recent improved techniques for tidal analysis of moving-vessel ADCP measurements, as described in Vennell and Old (2007).

## 6.2 Momentum Balance and Flow Separation

The momentum balances expressed in Figures 4.1a and 4.2 show that the streamwise tidal flow at point I encounters an adverse (i.e., positive) pressure gradient, which causes it to decelerate due to combined pressure gradient and bottom friction effects, resulting in flow reversal (see Fig. 4.1a). Flow separation occurs at the same location (off Chatham, MA) during both flood and ebb flow phases, suggesting that the local adverse pressure gradient in the CBL is the result

of the large-scale pressure gradient and the seafloor topography.

The results also indicate that flow separates about 0.6 hours later during the ebb cycle as compared to the flood cycle. Pingree (1978) and Park and Wang (2000) pointed that in a CW circulation, curvature and Coriolis effects are opposed and, therefore, for similar current strengths during flood and ebb, the pressure gradient term will be reduced during the CW circulation (i.e., ebb flow in the present study). As shown in Figure 4.1a, this asymmetry in the streamwise pressure gradient term seems to be the reason why flow separates later during ebb than during the flood. Signell and Geyer (1991) used an analytical model to determine the pressure gradient along the CBL of a hypothetical elliptical headland. They solved the boundary layer equation, with a linearized friction term, by using the solution of a steady uniform flow offshore multiplied by  $\sin \sigma t$ . In doing so, they found that for their hypothetical case, flow separation does not occur when the advective term is dominated by either the frictional or local acceleration terms. The results presented here, however, indicate that flow separation occurs in the CBL as a result of a primary balance between the streamwise local acceleration and pressure gradient (with significant contributions from bottom friction during times of large velocities; see Fig. 4.1a and Fig. 4.2). This discrepancy reinforces the fact that the case studied by Signell and Geyer (1991) differs from the case presented here.

## 6.3 Three-Dimensional Circulation

### 6.3.1 Mechanisms controlling the secondary flow

As presented in Section 1.2, the secondary flow can be “driven” by Coriolis or centrifugal forces associated with the streamwise flow (Garrett and Loucks 1976;

Kalkwijk and Booij 1986; Geyer 1993; Alaee et al. 2004; Neill et al. 2007). It is well known that secondary circulation induced by centrifugal force (associated with the streamwise flow) is always directed offshore near the surface and onshore near the bottom, independent of the streamwise current direction (Garrett and Loucks 1976; Kalkwijk and Booij 1986; Geyer 1993). The numerical model results presented here in Chapter 5 show that the directions of the near-bottom and near-surface secondary flow change during the  $M_2$  tidal cycle. Therefore, we conclude that the secondary circulation in our study region is the result of the streamwise flow being turned by the Coriolis force. This conclusion is supported by the Chapter 4 depth-averaged normal-direction momentum balances in which Coriolis dominates over centrifugal forces during the tidal cycle (see Figs. 4.1 to 4.5).

Concerning large-scale flows, in the regions of coastal promontories, Pingree (1978) proposed that the Coriolis force (associated with the streamwise flow) becomes important, acting with or against the centrifugal force depending upon flow direction. In such cases, the intensity of the secondary flow is amplified in ACW and reduced in CW flows (Neill et al. 2007). Our numerical results indicate that the secondary flow is more intense in the presence of ACW flow. For example, after maximum flood and in the presence of an ACW eddy motion (see Figs. 5.1c and 5.3c, respectively), our secondary flow is stronger than in the presence of CW flows (during maximum flood and in the presence of a CW eddy motion; see Figs. 5.4c and 5.5c).

### 6.3.2 Upwelling and downwelling

Vertical water motion in the absence of eddies has been reported for many three-dimensional numerical studies (Alaee et al. 2004; Doglioli et al. 2004; Jones

et al. 2006; White and Wolanski 2008). In our study, we found that during maximum flood/ebb the vertical velocities along transect 1 are not controlled by the secondary flow dynamics (Figs. 5.1 and 5.4). This can be shown quantitatively by using the conservation of mass equation:  $\frac{\partial u_s}{\partial s} + \frac{\partial u_n}{\partial n} = -\frac{w}{h}$ . Using the divergence of the depth-averaged streamwise flow ( $\frac{\partial \bar{u}_s}{\partial s}$ ) as a proxy for the divergence of the streamwise flow ( $\frac{\partial u_s}{\partial s}$ ) and assuming that  $\frac{\partial u_n}{\partial n} = 0$ , then  $w = -h \frac{\partial \bar{u}_s}{\partial s}$ . From Figure 5.2a,  $\frac{\partial \bar{u}_s}{\partial s} \sim \frac{\partial u_s}{\partial s} \sim -2 \times 10^{-5} \text{ s}^{-1}$  for transect 1, where  $h = -50$ , and  $w \sim -1 \times 10^{-3} \text{ m/s}$ . This compares favorably with the range of values in Figure 5.1d. The same reasoning applies during maximum ebb. Therefore, in contrast to previous results in the literature (Alaee et al. 2004; White and Wolanski 2008), the nearshore downwelling (upwelling) during maximum flood (ebb) results from the convergence (divergence) of the main tidal flow.

The above result is illustrated schematically in Figure 6.1 (top) during maximum flood. The results are the opposite during maximum ebb (not shown), with the convergence and divergence of the secondary and primary flows, respectively. The conservation of mass equation also suggests that during maximum flood (ebb) and close to the bathymetry slope break, the vertical velocity seems to be controlled by the convergence (divergence) of both the main flow and the secondary flow.

Figure 6.1 (bottom) shows a schematic representation of this situation during maximum flood. In the presence of an ACW (CW) eddy motion, the near-coast upwelling (downwelling) is also influenced by both the main flow and the secondary flow (Fig. 6.2 top), while close to the bathymetry slope break (Fig. 6.2 bottom) downwelling (upwelling) occurs due to the main flow convergence (divergence). The role of the eddy motions in modifying the typical secondary flow of the

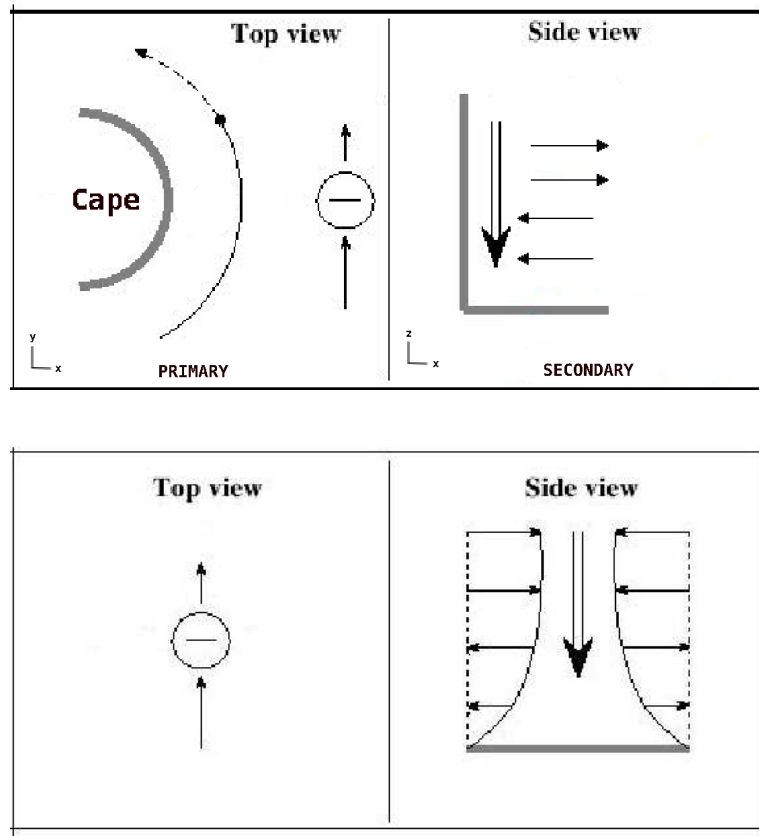


Figure 6.1: Schematic of the transect 1 maximum flood tidal flow (time A) in (top) the nearshore region and (bottom) the bathymetric slope region, where +/- indicate locations of upwelling/downwelling associated with diverging/converging flows, respectively. The primary flow structure is shown in the top views while the secondary flow structure is shown in the side views.

dominant flood or ebb can be examined from the set of cartoons presented in Figure 5.8. The ACW eddy motion formed after maximum flood is responsible for moving the downwelling zone offshore and creating a nearcoast upwelling cell. On the other hand, the CW eddy motion formed after maximum ebb is responsible for moving the upwelling zone offshore and creating a nearcoast downwelling cell.

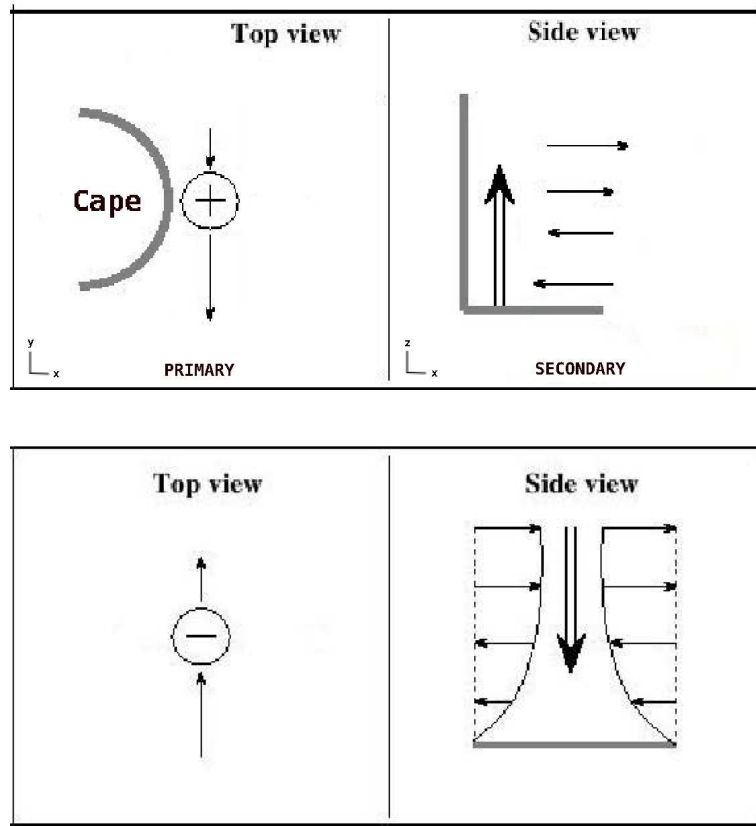


Figure 6.2: Schematic of the transect 1 slack before ebb flow (time C) in (top) the nearshore region and (bottom) the bathymetric slope region, where +/- indicate locations of upwelling/downwelling associated with diverging/converging flows, respectively. The primary flow structure is shown in the top views while the secondary flow structure is shown in the side views.

### 6.3.3 Maximum strength of the secondary flow

How does the surface maximum strength of the secondary flow in our model results compare with that predicted by the Alaee et al. (2004) theory? As presented in Section 1.2, it is essential to determine  $R_{ef} = \frac{h}{C_{db}}$  and  $R_{om} = \frac{2U_s}{fR_s}$  to estimate the strength of the secondary flow based on Table 1.1. Using representative numerical model values during maximum flood (time A) of  $U_s = 0.8$  m/s,  $h = 50$  m,  $b = 2 \times 10^4$  m (streamwise length scale),  $R_s = 10^5$  m,  $f = 9.7 \times 10^{-5}$  s<sup>-1</sup> and

$C_d = 0.005$ , we get  $R_{ef} = 0.5$  and  $R_{om} = 0.2$ , which suggest flow regime A. Using the relevant equation presented in Table 1.1, with the constant  $K_A = 0.026$ , we obtain  $u_n = 0.025$  m/s, which compares favorably with our numerical model surface layer at 50 meters depth in Fig. 5.1b. In fact, the results presented in Chapter 5 suggest that the instantaneous secondary flow is controlled by the Coriolis force. The surface maximum strength of the secondary circulation is approximately 3% of the instantaneous corresponding streamwise tidal flow. This number is much smaller than the percentage found in other studies where the instantaneous  $u_n$  is controlled by the centrifugal force (Geyer 1993; Berthot and Pattiariatchi 2006; Neill et al. 2007). This result suggests that the Alaee et al. (2004) method is reasonable in predicting the surface maximum strength of the secondary circulation off Chatham, MA.

### 6.3.4 Tidal long-term circulation

Which force (centrifugal or Coriolis) drives the secondary flow over the long term? To address this question we computed the 31-day average of the model results. Following Garrett and Loucks (1976), we compare the strength of the model Coriolis ( $fU$ ) and centrifugal ( $\frac{1}{2}\frac{U^2}{R_s}$ ) forces, where  $U$  is the long-term average current,  $f$  the Coriolis parameter,  $U_t$  is the the maximum tidal current magnitude and  $R_s$  its corresponding radius of flow curvature. We shall concentrate the analysis on transect 1, where the asymmetric characteristics of the eddy motions are revealed most strongly in the long-term depth-averaged circulation in that region (Fig. 6.3), which features an ACW flow pattern. The nearshore long-term secondary flow pattern suggests that Coriolis force is more important than centrifugal force. Using the numerical model results for the node highlighted in black (Fig. 6.3), we have the

following: Coriolis =  $(9.7 \times 10^{-5}) \times 0.06 = 5.8 \times 10^{-6} \text{ ms}^{-2}$  and centrifugal  
 $= 0.5 \frac{0.70^2}{1.7 \times 10^5} = 1.6 \times 10^{-6} \text{ ms}^{-2}$ . Based on the direction of the flow presented in  
 Figure 6.3, the two forces are in opposition. Therefore, the small difference between  
 them justifies the weak Coriolis-induced long-term secondary circulation close to the  
 coast (Fig. 5.7a). However, in the offshore region, the long-term secondary flow  
 pattern indicates that centrifugal force dominates. This conclusion is supported by  
 numerical model results which were extracted from the blue-dot node (Fig. 6.3):  
 Coriolis =  $(9.7 \times 10^{-5}) \times 0.03 = 2.9 \times 10^{-6} \text{ ms}^{-2}$  versus centrifugal  
 $= 0.5 \frac{0.75^2}{1 \times 10^4} = 2.8 \times 10^{-5} \text{ ms}^{-2}$ . The onshore centrifugal-induced long-term  
 secondary circulation is one order of magnitude larger than the Coriolis-induced. As  
 a result nearcoast upwelling occurs in the boundary between these two long-term  
 secondary circulation cells (Fig. 5.7c)

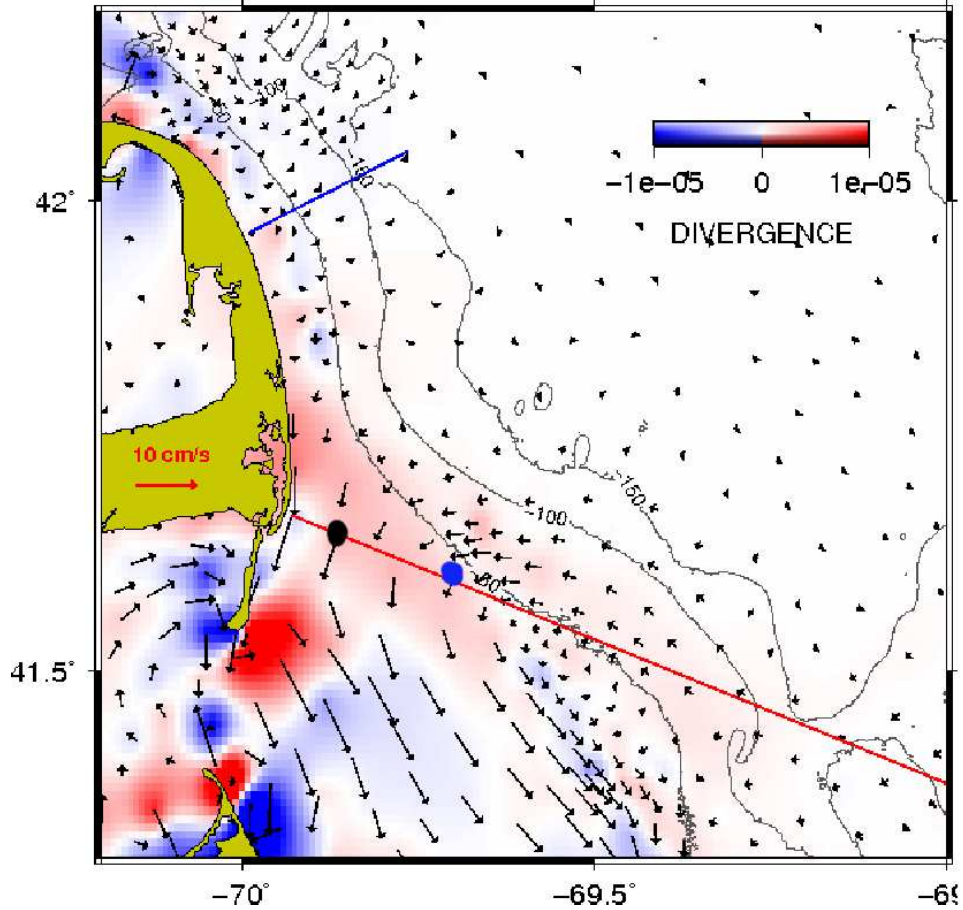


Figure 6.3: Distribution of long-term depth-averaged model flow vectors (cm/s) and its divergence ( $s^{-1}$ , color-coded), in which red means divergence (and blue convergence). Transects 1 (red) and 2 (blue) are located, and the black and blue dots highlight the nodes where the strength of both Coriolis and centrifugal forces are estimated.

# Chapter 7

## Summary and Concluding Remarks

The kinematics and dynamics of the tidal flow in the western Gulf of Maine were investigated, with focus on the secondary circulation, using a validated application of the three-dimensional nonlinear hydrodynamic finite element numerical model, QUODDY. The model was forced with the five most important tidal constituents for the region ( $M_2$ ,  $N_2$ ,  $S_2$ ,  $K_1$  and  $O_1$ ) and operated in the barotropic mode. A direct comparison with observed currents revealed that the model-derived currents on the nearshore side of the GSC region were being overestimated.

Using model-derived results, two-dimensional momentum balance calculations in a streamwise/normal coordinate system were performed to evaluate the overall momentum balance in representative (nearshore and offshore) regions. In the nearshore region, the spatial distribution of the momentum terms during maximum flood/ebb show the presence of a streamwise adverse pressure gradient force off Chatham, MA, and strong bottom friction, resulting in flow separation and eddy motion formation. The shallower-water kinematic characteristics are close to those of a progressive wave, where the principal streamwise dynamical balance is between pressure gradient force (PGF) and local acceleration (LA), with strong influence

from bottom friction (BF) during times of significant currents. In deeper waters, the kinematic characteristics are close to those of a standing wave, where the principal streamwise dynamical balance is between PGF and LA. For both nearshore and offshore regions, the principal normal direction dynamical balance is between PGF and Coriolis force. The eddy motion presented here was found to be a phase eddy consistent with the eddy generation process proposed by Black and Gay (1987), and thus fundamentally different from the mechanism described by Signell and Geyer (1991) for the Gay Head eddies.

A possible mechanism for the instantaneous secondary circulation computed during one  $M_2$  tidal cycle is suggested by a local imbalance between the normal pressure gradient and Coriolis force. Our results and the case studied by Doglioli et al. (2004) are among the few examples of Coriolis-induced ( $R_o < 1$ ) secondary circulation in the literature. Interestingly, the upwelling/downwelling in the study region were not dominated by the secondary circulation. Rather, the model results show that instantaneous vertical motions close to the coast and close to the bathymetric slope are mainly controlled by the divergence/convergence of the main flow. This work is not aimed at quantifying the contribution of the main flow to the vertical velocity, and further work should include that. The model result suggests that the method proposed by Alaee et al. (2004) predicts reasonably well the surface maximum strength of the secondary circulation off Chatham, MA. The long-term (31-day average) model results indicated a centrifugally induced inshore near-bottom transport in the study region, and resulting upwelling. We have not discussed here the density-driven flows that would result from vertical mixing. This clearly requires further investigation.

The present study also provides some useful insights for more realistic modeling in the future. Future studies should include a depth-dependent bottom friction coefficient (e.g., Chezy's C, Black and Gay 1987) in addition to a higher-resolution mesh east of Cape Cod, MA, in order to better represent the currents in shallower waters.

# Appendix A

## Model/Observation Comparisons

Figures A.1 to A.10 show a comparison between modeled and observed sea-level amplitudes and phases for the five most important tidal constituents in the domain ( $M_2$ ,  $N_2$ ,  $S_2$ ,  $K_1$  and  $O_1$ ) derived from simulation 01 ( $C_d=0.005$ ). The results are presented in terms of differences between model results and observations. The amplitude differences are expressed as percentages of the observed values. The average and standard deviation values of the differences between model and observation are also shown in the figures.

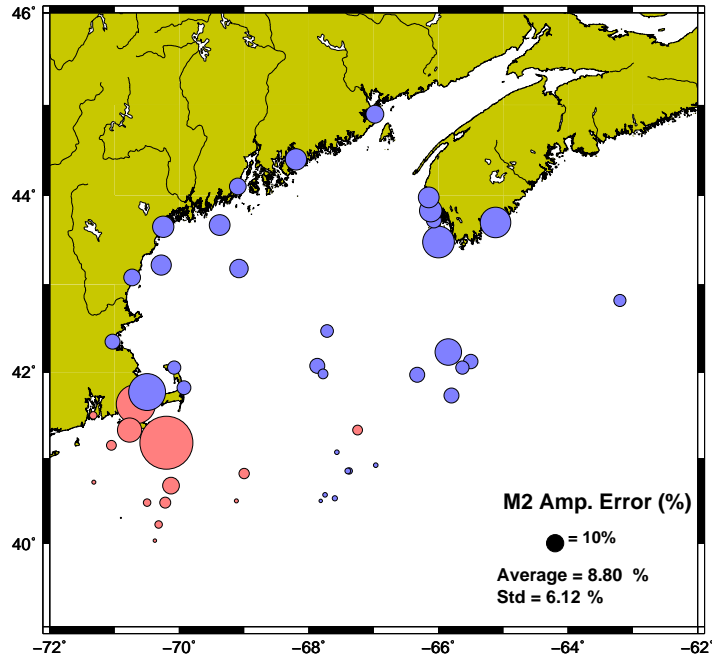


Figure A.1: Difference between modeled and observed  $M_2$  tidal sea level amplitudes expressed in percentage of the observed values. Red circles indicate model underestimation; blue values indicate model overestimation.

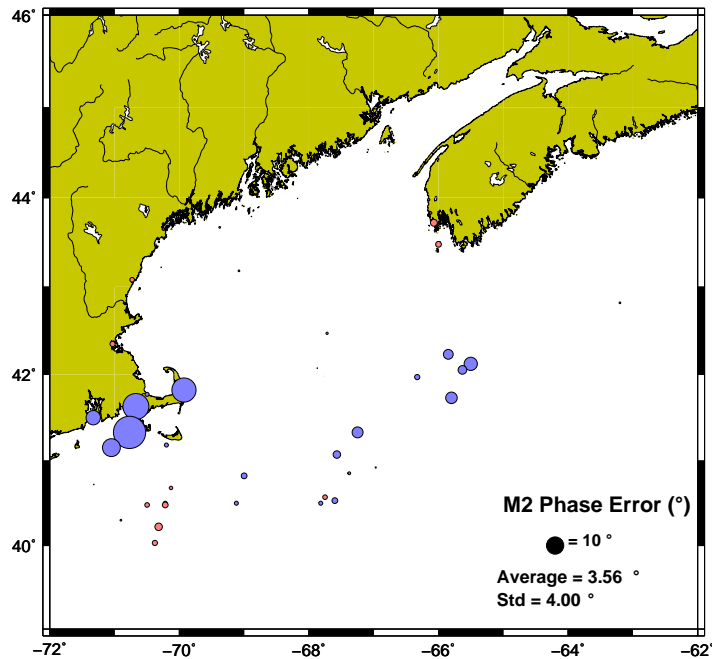


Figure A.2: Difference between modeled and observed  $M_2$  tidal sea level phases expressed in Greenwich epoch (°). Red circles indicate model underestimation; blue values indicate model overestimation.

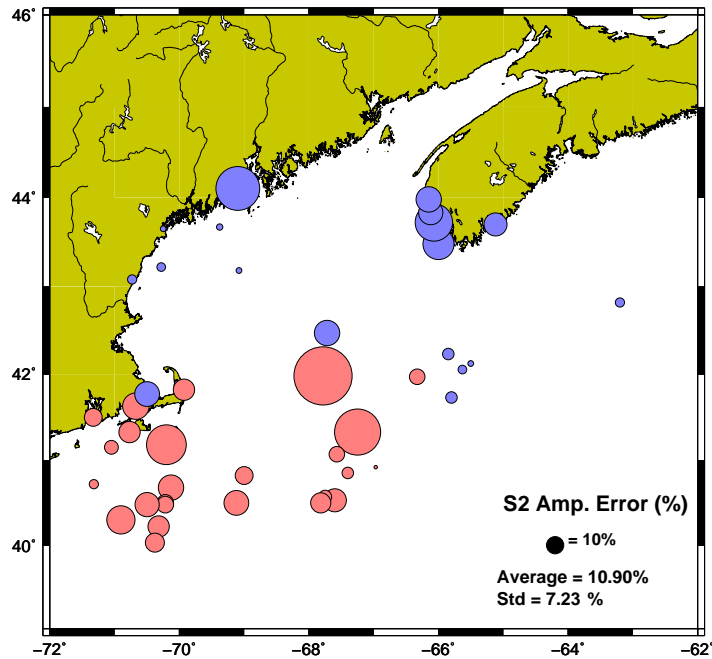


Figure A.3: Difference between modeled and observed  $S_2$  tidal sea level amplitudes expressed in percentage of the observed values. Red circles indicate model underestimation; blue values indicate model overestimation.

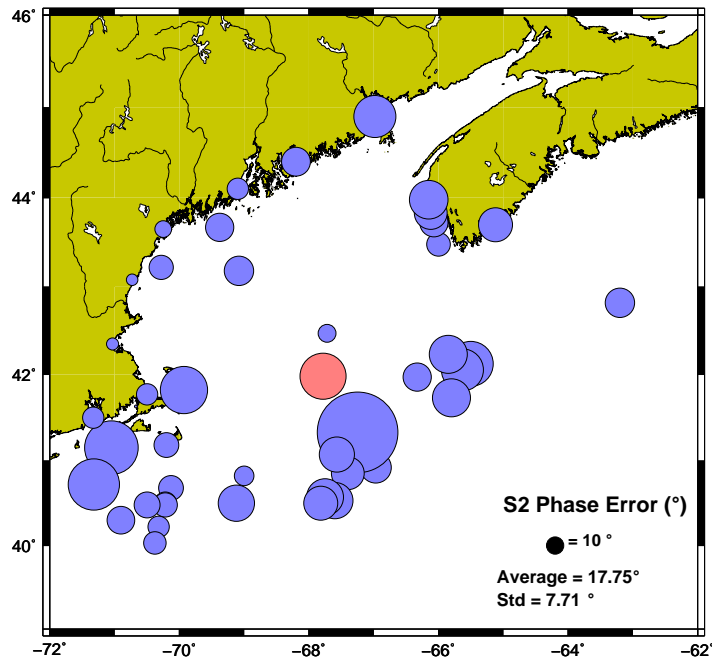


Figure A.4: Difference between modeled and observed  $S_2$  tidal sea level phases expressed in Greenwich epoch (°). Red circles indicate model underestimation; blue values indicate model overestimation.

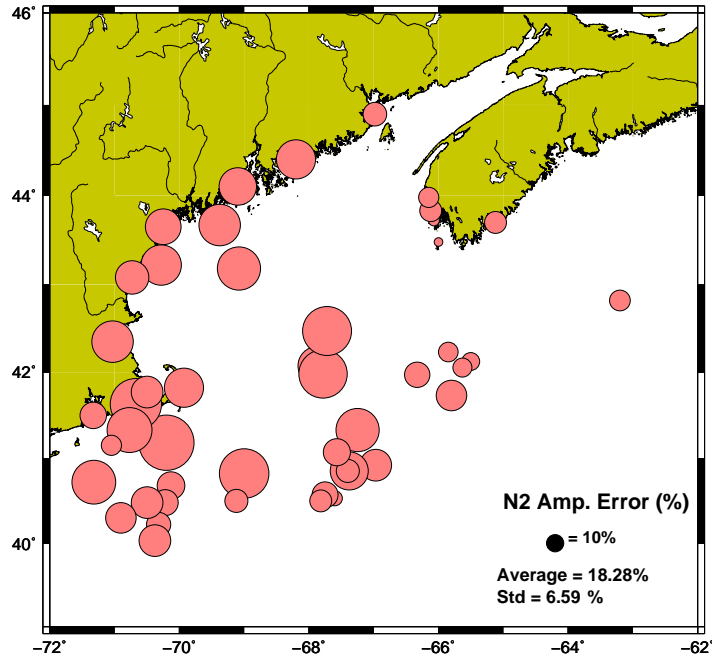


Figure A.5: Difference between modeled and observed  $N_2$  tidal sea level amplitudes expressed in percentage of the observed values. Red circles indicate model underestimation; blue values indicate model overestimation.

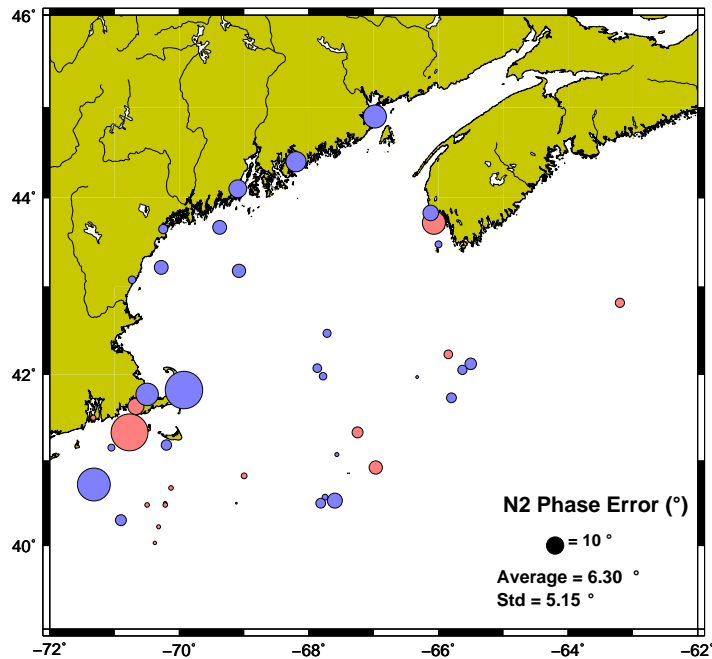


Figure A.6: Difference between modeled and observed  $N_2$  tidal sea level phases expressed in Greenwich epoch ( $^{\circ}$ ). Red circles indicate model underestimation; blue values indicate model overestimation.

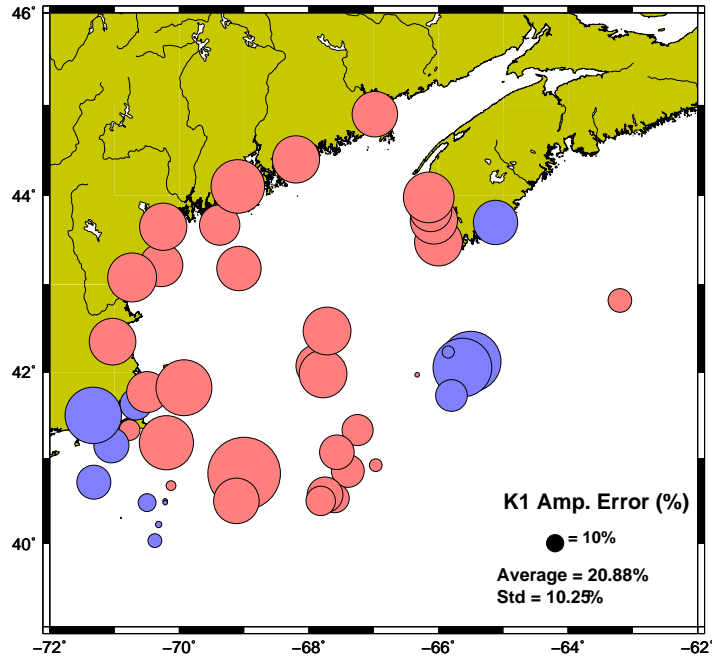


Figure A.7: Difference between modeled and observed  $K_1$  tidal sea level amplitudes expressed in percentage of the observed values. Red circles indicate model underestimation; blue values indicate model overestimation.

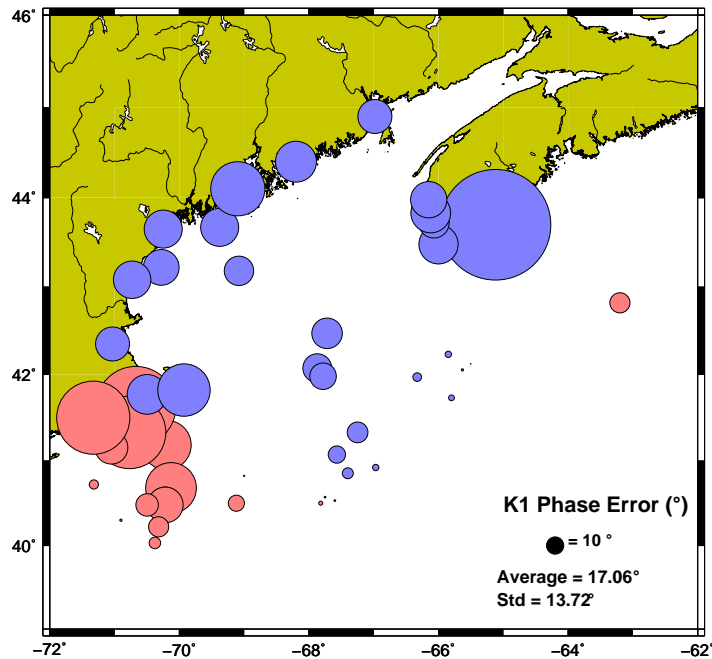


Figure A.8: Difference between modeled and observed  $K_1$  tidal sea level phases expressed in Greenwich epoch ( $^{\circ}$ ). Red circles indicate model underestimation; blue values indicate model overestimation.

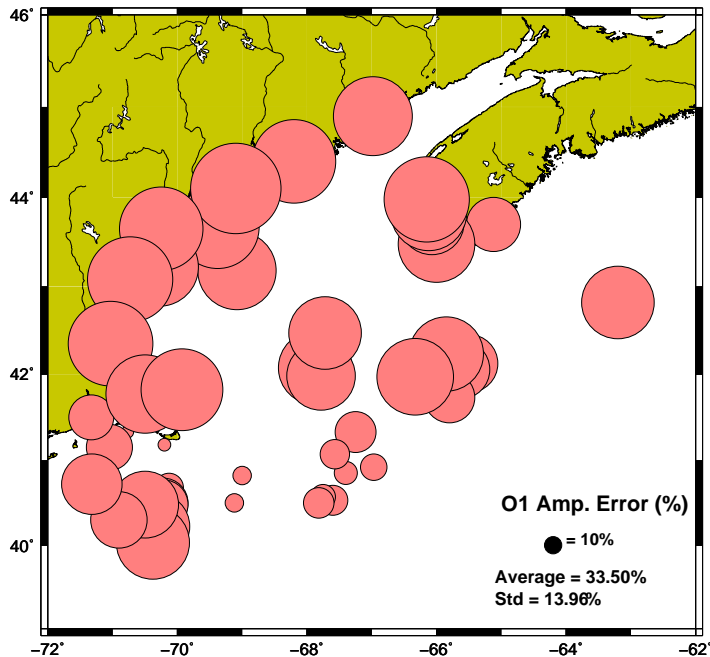


Figure A.9: Difference between modeled and observed  $O_1$  tidal sea level amplitudes expressed in percentage of the observed values. Red circles indicate model underestimation; blue values indicate model overestimation.

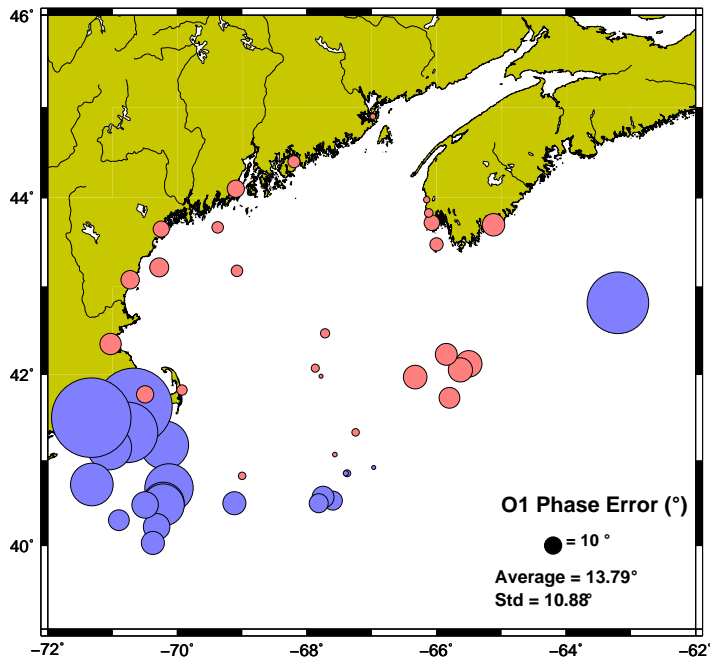


Figure A.10: Difference between modeled and observed  $O_1$  tidal sea level phases expressed in Greenwich epoch ( $^{\circ}$ ). Red circles indicate model underestimation; blue values indicate model overestimation.

## Appendix B

# The Gradient of a Scalar in an Unstructured Grid

The gradient of a scalar in an unstructured grid can be calculated using a method based on the Kelvin-Stokes theorem:

$$\int_{\Sigma} \nabla \times \vec{F} \cdot d\Sigma = \oint_{\partial\Sigma} \vec{F} \cdot d\vec{r}, \quad (\text{B.1})$$

which relates the surface integral of the curl of a vector field ( $\vec{F}$ ) over a surface ( $\Sigma$ ) in Euclidean three-space to the line integral of the vector field over its boundary ( $\vec{r}$ ).

The curve of the line integral ( $\partial\Sigma$ ) must have positive orientation, meaning that  $d\vec{r}$  points counterclockwise when the surface normal ( $d\Sigma$ ) points toward the viewer, following the right-hand rule.

Using Eq. (B.1), the gradient of a scalar (i.e., elevation or velocity component) in the  $x$  and  $y$  directions for a specific grid node can be calculated according to Eqs. (B.2) and (B.3), respectively.

$$\frac{\partial F}{\partial x} = \sum_{i=1}^{nn-1} \left[ \frac{F_i + F_{i+1}}{2} \right] \times [y_{i+1} - y_i] / \sum_{i=1}^{ne} A_i \quad (\text{B.2})$$

$$\frac{\partial F}{\partial y} = \sum_{i=1}^{nn-1} \left[ \frac{F_i + F_{i+1}}{2} \right] \times [x_{i+1} - x_i] / \sum_{i=1}^{ne} A_i, \quad (\text{B.3})$$

where  $nn$  is the number of surrounding nodes,  $ne$  is the number of surrounding elements and  $A_i$  is the area of the  $i^{th}$  element.

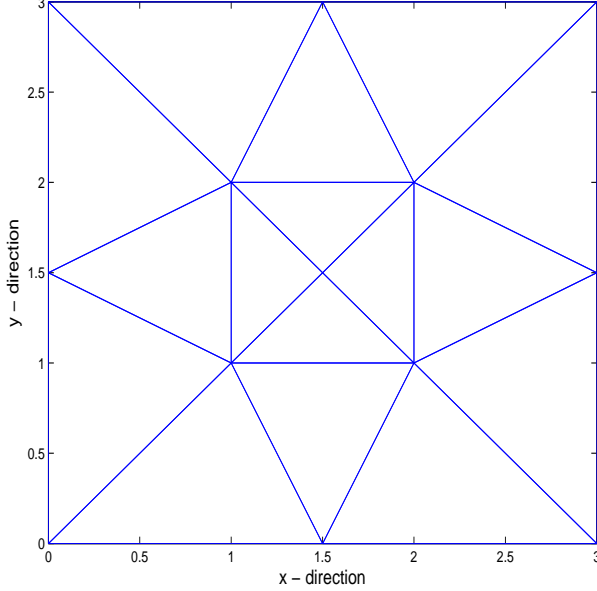


Figure B.1: Idealized unstructured mesh with 13 nodes and 16 elements.

To test the fidelity of this method, a simple idealized unstructured mesh was created (Fig. B.1) to allow basic calculations. Since this is a diagnostic calculation, we use a linear equation to verify the validity of this method.

A linear distribution of a scalar property ( $S$ ),

$$S = 5 \times x + 10 \times y \quad (\text{B.4})$$

was applied to the idealized grid defined by Figure B.2a.

The gradients of  $S$  in the  $x$  and  $y$  directions were computed using Eqs. (B.2) and (B.3), respectively, and their results are shown in Figure (B.2b and c). Notice that the results match the analytical solution of Eq. (B.4) ( $\frac{\partial S}{\partial x} = 5$  and  $\frac{\partial S}{\partial y} = 10$ ).

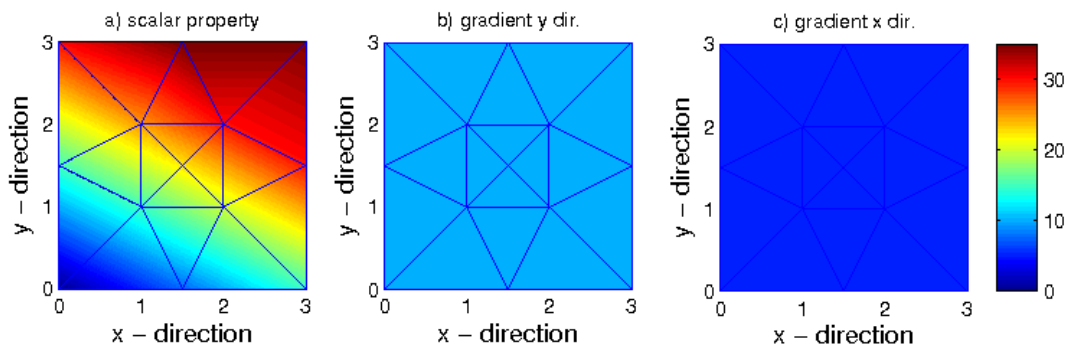


Figure B.2: a) Linear distribution of a scalar  $S$  over the idealized mesh according to Eq. (B.4), b) gradient of  $S$  in the  $y$  direction, and c) gradient of  $S$  in the  $x$  direction.

# Bibliography

- Alaee, M., G. Ivey, and C. Pattiaratchi (2004). Secondary circulation induced by flow curvature and Coriolis effects around headlands and islands. *Ocean Dynamics* 54(1), 27–38.
- Berthot, A. and C. Pattiaratchi (2006). Field measurements of the three-dimensional current structure in the vicinity of a headland-associated linear sandbank. *Continental Shelf Research* 26(3), 295–317.
- Black, K. P. and S. L. Gay (1987). Eddy formation in unsteady flows. *J. Geophys. Res.* 92(C9), 9514–9522.
- Brown, W. (1984). A comparison of Georges Bank, Gulf of Maine and New England Shelf Tidal Dynamics. *Continental Shelf Research* 14(1), 145–167.
- Brown, W., G. M. Marques, S. King, C. Jakubiak, D. Brown, E. Levine, and L. Goodman (2009). Transient tidal eddy project data report: Winter 2008-09. Technical Report 09-0204, School for Marine Science and Technology (SMAST), University of Massachusetts Dartmouth, <http://www.smast.umassd.edu/OCEANOL/reports.php>.
- Brown, W. and Z. Yu (2006). Codar measurement and model simulation of transient tidal eddies in the western Gulf of Maine. Technical Report 06-0503, School for Marine Science and Technology (SMAST), University of

Massachusetts Dartmouth,  
<http://www.smast.umassd.edu/OCEANOL/reports.php>.

Chen, C., R. Beardsley, and R. Limeburner (1995). Variability of currents in late spring in the northern Great South Channel. *Continental Shelf Research* 15, 451–473.

Dennis, R. and E. Long (1971). Users guide to a computer program for harmonic analysis of data at tidal frequencies. Technical Report NOS41, NOAA.

Doglioli, A. M., A. Griffa, and M. G. Magaldi (2004). Numerical study of a coastal current on a steep slope in presence of a cape: The case of the Promontorio di Portofino. *J. Geophys. Res.* 109(C12033), 19.

Fofonoff, P. and R. J. Millard (1983). Algorithms for computation of fundamental properties of seawater. Technical Report 44, Unesco Tech. Pap. in Mar. Sci.

Garrett, C. and R. H. Loucks (1976). Upwelling along the Yarmouth shore of Nova Scotia. *J. Fish. Res. Board Can.* 33, 116–117.

Geyer, W. (1993). Three-Dimensional flow around headlands. *J. Geophys. Res.* 98, 955–966.

Geyer, W. and R. Signell (1990). Measurements of tidal flow around a headland with a shipboard acoustic doppler current profiler. *J. Geophys. Res.* 95, 3189–3197.

He, R. and J. L. Wilkin (2006). Barotropic tides on the southeast New England shelf: A view from a hybrid data assimilative modeling approach. *J. Geophys. Res.* 111(C08002), 1–20.

Hench, J. L. and R. A. Leutich (2003). Transient Tidal Circulation and

- Momentum Balance at a Shallow Inlet. *J. Physical Oceanography* 33, 913–932.
- Holboke, M. (1998). *Variability of the Maine coastal current under spring conditions*. Ph. D. thesis, Thayer School of Engineering-Dartmouth College.
- Jones, O., R. Simons, E. Jones, and J. Harris (2006). Influence of seabed slope and Coriolis effects on the development of sandbanks near headlands. *J. Geophys. Res.* 111(C03020), 1–23.
- Kalkwijk, J. P. T. and R. Booij (1986). Adaptation of secondary flow in nearly horizontal flow. *Journal of Hydraulic Research* 24(1), 19–37.
- Lee, H. J., S. Y. Chao, K. L. Fan, and T. Y. Kuo (1999). Tide-induced eddies and upwelling in a semi-enclosed basin: Nan Wan. *Estuarine, Coastal and Shelf Science* 49(6), 775–787.
- Lynch, D., J. Ip, C. Naimie, and F. Werner (1996). Comprehensive coastal circulation model with application to the Gulf of Maine. *Cont. Shelf Res.* 16, 875–906.
- Lynch, D. and C. Naimie (1992). The M2 tide and its residual on the outer banks of the Gulf of Maine. *J. Physical Oceanography* 23(10), 2222–2253.
- Lynch, D., F. Werner, D. Greenberg, and J. Loder (1992). Diagnostic model for baroclinic, wind-driven and tidal circulation in shallow seas. *Cont. Shelf Res.* 12, 37–64.
- MacCready, P. and G. Pawlak (2001). Tidal eddy generation at Three Tree Point: Theory and numerical modeling. In *Proceedings of the Puget Sound Research Conference*.
- Moody, J. A., B. Butman, R. Beardsley, W. Boicourt, W. Brown, P. Daifuku,

- J. Irish, D. Mayer, H. Mofjeld, B. Petrie, S. Ramp, P. Smith, and W. Wright (1984). Atlas of tidal elevation and current observations on the Northeast American Continental Shelf and slope. Technical Report 1611, U.S. Department of the Interior.
- Mukai, A., R. Westerink, J. Luettich, and D. Mark (2002). Eastcoast 2001, a tidal constituent database for western North Atlantic, Gulf of Mexico, and Caribbean Sea. Technical report, Coastal and Hydraulics Laboratory, US Army Corps of Engineers., <http://www.unc.edu/ims/ccats/tides/tides.htm>.
- Neill, S. P., R. M. Hashemi, and A. J. Elliott (2007). An enhanced depth-averaged tidal model for morphological studies in the presence of rotary currents. *Continental Shelf Research* 27(1), 82–102.
- Park, M. and D. Wang (2000). Tidal vorticity around a coastal promontory. *Journal of Oceanography* 56, 261–273.
- Pingree, R. (1978). The formation of the Shambles and other banks by tidal stirring of the seas. *Journal of the Marine Biological Association of the United Kingdom* 58, 211–226.
- Pingree, R. and L. Maddock (1977). Tidal eddies and coastal discharge. *Journal of the Marine Biological Association of the United Kingdom* 57(3), 869–875.
- Pingree, R. and L. Maddock (1979a). Tidal flow around an island with a regularly sloping bottom topography. *Journal of the Marine Biological Association of the United Kingdom* 59, 699–710.
- Pingree, R. and L. Maddock (1979b). The tidal physics of headland flows and offshore tidal bank formation. *Marine Geology* 32, 269–289.

- Shcherbina, A. and G. Gawarkiewicz (2008). A coastal current in winter: Autonomous underwater vehicle observations of the coastal current east of Cape Cod. *J. Geophys. Res.* 113(C07030), 15.
- Signell, R. and W. Geyer (1991). Transient eddy formation around headlands. *J. Geophys. Res.* 96, 2561–2575.
- Smagorinsky, J. (1963). General circulation experiments with the primitive equations i. The basic experiment. *Monthly Weather Review* 91(3), 99–164.
- Stokesbury, K., B. Harris, M. Marino II, and J. Nogueria (2004). Estimation of sea scallop abundance using video survey in off-shore U.S. waters. *Journal of Shellfish Research* 23(1), 33–40.
- Vennell, R. and C. Old (2007). High resolution observations of the intensity of secondary circulation along a curved tidal channel. *J. Geophys. Res.* 112(11), C11008. doi:10.1029/2006JC003764.
- White, L. and E. Deleersnijder (2007). Diagnoses of vertical transport in a three-dimensional finite element model of the tidal circulation around an island. *Estuarine, Coastal and Shelf Science* 74, 655–669.
- White, L. and E. Wolanski (2008). Flow separation and vertical motions in a tidal flow interacting with shallow-water island. *Estuarine, Coastal and Shelf Science* 77, 457–467.
- Wolanski, E., T. Asaeda, A. Tanaka, and E. Deleersnijder (1996). Three-dimensional island wakes in the field, laboratory experiments and numerical models. *Continental Shelf* 16(11), 1437–1452.
- Wolanski, E. and W. M. Hamner (1988). Topographically controlled fronts in the

- ocean and their biological influence. *Science* 241, 177–181.
- Wolanski, E., I. Imberger, and M. I. Heron (1984). Island wakes in shallow coastal waters. *J. Geophys. Res.* 89, 553–569.
- Zimmerman, J. T. F. (1976). Topographic generation of residual circulation by oscillatory (tidal) currents. *Geophysical and Astrophysical Fluid Dynamics* 11, 35–47.